Mechanical properties of peripheral stress fibers in adherent cells spreading on patterned substrates

THÈSE N^{O} 6634 (2015)

PRÉSENTÉE LE 3 JUILLET 2015
À LA FACULTÉ DES SCIENCES DE BASE
LABORATOIRE DE BIOPHYSIQUE CELLULAIRE
PROGRAMME DOCTORAL EN PHYSIQUE

ÉCOLE POLYTECHNIQUE FÉDÉRALE DE LAUSANNE

POUR L'OBTENTION DU GRADE DE DOCTEUR ÈS SCIENCES

PAR

Céline Jeanne LABOUESSE

acceptée sur proposition du jury:

Prof. V. Savona, président du jury
Prof. J.-J. Meister, directeur de thèse
Prof. J. Snedeker, rapporteur
Dr M. Balland, rapporteur
Prof. G. Dietler, rapporteur

ÉCOLE POLYTECHNIQUE
FÉDÉRALE DE LAUSANNE

Suisse
2015

Ai-je vraiment cherché quelque chose? J'ai bien sûr soulevé quelques pierres, sondé la base de la falaise ouest, à l'aplomb des cavernes que j'ai repérées à mon arrivée (...) Quand je suis entré pour la première fois dans le ravin, j'ai compris que ce n'était pas l'or que je cherchais, mais une ombre, quelques choses comme un souvenir, comme un désir.

J.M.G Le Clézio, *Voyage à Rodrigues*

Remerciements

Cette thèse est le fruit de quatre ans de travail au LCB. Il y a eu évidemment des hauts et des bas, autant dans les résultats que dans la motivation, mais j'ai eu la chance de pouvoir compter pendant ce temps sur l'aide de tous les membres du laboratoire, et sur quelques collaborations extérieures. Je voudrais donc remercier tous ceux qui ont participé de près ou de loin à ce travail, et ceux qui m'ont supporté toutes ces années au LCB, je sais que je ne vous ai pas rendu la vie facile.

Je voudrais avant tout remercier le Prof. Jean-Jacques Meister de m'avoir accueilli au LCB et pour son aide tout au long de ces 4 ans. Je vous suis reconnaissante à la fois pour vos nombreux conseils scientifiques et pratiques pendant la thèse, et pour la liberté que vous m'avez laissé. Sans doute que j'ai un peu tendance à n'en faire qu'à ma tête, mais j'ai essayé malgré cela de suivre vos conseils. De plus, les conditions de travail étaient assez exceptionnelles, et ce n'est pas seulement dû à la proximité du lac et des pistes de ski. J'ai eu notamment la chance de pouvoir voyager tous les ans en conférence.

Je voudrais ensuite remercier les membres du jury pour leurs commentaires et suggestions intéressantes pour la suite du projet, Dr. Martial Balland, Prof. Jess Snedeker, Prof. Giovanni Dietler et Prof. Vincenzo Savona.

Certaines personnes ont contribué plus particulièrement à certains aspects de cette thèse. Tout d'abord Yannick Loosli et Prof. Jess Snedeker de l'Université de Zurich sont ceux qui ont émis l'hypothèse du *length maturation threshold*, et l'idée qu'il y a un lien entre la géométrie imposées aux cellules et la distribution des adhésions et des fibres de stress. Cela m'a permis de prendre un bon départ dans ces 4 ans de thèse avec une collaboration fructueuse. Ca a été une chance mais aussi un plaisir de travailler avec vous.

La deuxième partie de cette thèse sur la réponse des cellules à une diminution de la contractilité a été en partie inspirée par le travail de Prof. Ulrich Schwarz, à l'Université d'Heidelberg. Je voudrais chaleureusement le remercier pour son accueil dans son groupe, ainsi que ses deux doctorants Jérôme Soiné et Christoph Brandt. Je n'ai pas pu utiliser de manière approfondie leur modèle d'analyses des forces de traction, mais malgré cela mon court séjour à Heidelberg à été très bénéfique.

Mais la plus grande partie du travail a été faite au LCB. Pour le coté expérimental, un immense merci à Josiane pour toutes les cultures cellulaires, les manips, les transfections, les immunofluorescences, les échantillons de PDMS, les stamping... et j'en oublie certainement. Et merci également d'avoir eu la patience de m'apprendre ces techniques. Merci à Carine aussi pour nous avoir fourni les plasmides pour les transfections et ensuite pour ton aide sur certaines protocoles clés. Je voudrais mentionner aussi le staff du BIOP pour l'utilisation de leurs microscopes et leurs conseils avisés sur l'imagerie et le traitement d'images.

La microfabrication des substrats en salle blanche a été un travail de groupe. Alors merci au CMi de l'EPFL et à tout le staff pour leur aide sur les processus de photolithographie, mais surtout merci à Benoît, Camilo et Josiane que j'ai exploité un certain temps pour fabriquer mes échantillons. Et merci particulièrement à Benoît qui a pris le temps de m'expliquer, de débugger et d'optimiser tous ces processus de fabrication.

Je veux ensuite remercier Alicia et Niccolò pour leur expertise sur la fabrication des substrats mous (gels, PDMS) et le patterning/stamping de ces substrats, étape critique évidemment au succès des manips. Autres éléments essentiels évidemment, les fameux *ultrasoft* cantilevers. Un grand merci donc à Niccolò pour tout le temps que tu as investi dans la fabrication de ces cantilevers, ainsi qu'à Chiara et Benoît pour votre aide sur la caractérisation AFM des gels et des cantilevers. Je n'oublie évidemment pas Seb, qui a pris le temps d'optimiser les protocoles de stamping, m'a permis de faire des belles manips et ensuite a suivi mes lubies expérimentales malgré le peu de chance que le projet marche. Seb, ça a été super de travailler avec toi !

Coté projets, je dois beaucoup à Benoît, Chiara et Sasha que j'ai embarqué un peu de force dans mon projet sur la réponse dynamique des cellules à une inhibition de myosine. Grâce à eux, cela a finalement donné des résultats et une histoire à raconter. Ils ont également été indispensables pour faire avancer le projet des “trous”, qui était d'ailleurs leur idée au départ. Merci également à Francky, qui a toujours été très disponible pour discuter de plein de choses, des codes C++ à la préparation de l'oral, en passant par les séries de physique, tout cela avec la zénitude qu'il me manque.

Pour finir par le plus important, merci à Benoît et Chiara pour leur aide plus ou moins quotidienne sur tout, les manips, les discussion philosophiques, les analyses, la gestion des projets, la rédaction des papiers (et pour cela, je n'oublie pas non plus Sasha qui m'a appris que chaque mot est important, faut juste prendre le temps de trouver le bon). Je sais que j'ai parfois été trop impatiente pour ne pas dire plus, je vous en suis d'autant plus reconnaissante.

Enfin, car la science n'est pas tout, pour les séances de motivation en randonnant, en skiant, et plus récemment en grimpant, ou tout simplement autour d'un apéro, mais surtout pour leur présence dans les moments faciles et difficiles, je dois énormément au soutien

de ma famille et de mes amis : Papa qui m'a écouté râler tout ce temps, les “Parisiens” : Juliette, Balthazar, Clotilde, Agnes, et les Lausannois : Franck, Isa, Lise, the beautiful Camilo, e mille milioni di grazie alla Chiara. Et la personne la plus importante dans tout cela, pour le soutien moral, les coups de pied aux fesses, la motivation, l'inspiration, les discussions scientifiques biophysique ou neuro, et tous les autres papotages sur tous les sujets, the best sister of all, Marie !

Merci à vous tous.

Résumé

De multiples processus cellulaires sont dépendants d'interactions mécaniques entre la cellule et son milieu environnant. Notamment, l'architecture du cytosquelette d'actine est fonction des propriétés physiques de la matrice extracellulaire. Afin de mieux comprendre les mécanismes par lesquels le cytosquelette s'adapte au milieu extérieur nous avons étudié le cas particulier de fibres de stress périphériques. Ces épais faisceaux contractiles d'actine forment la bordure concave de cellules adhérentes sur des substrats micro-structurés. La visualisation des fibres par fluorescence, la mesure des forces de traction, et des techniques de micro-manipulation ont permis de mieux comprendre l'assemblage et les propriétés mécaniques de ces fibres. Nous avons combiné ces mesures expérimentales avec des simulations numériques, afin de proposer un modèle mécanique général décrivant le comportement de ces fibres de stress.

Nous avons d'abord identifié la formation de ces fibres périphériques comme signature d'une réorganisation du cytosquelette déclenchée par des intervalles non-adhésifs dans la géométrie du substrat. Ces fibres se forment au-delà d'une distance minimale de 3-4µm, nécessaire pour stimuler la maturation des adhésions terminales. La réorganisation du cytosquelette implique aussi une redirection des forces le long du bord cellulaire. De plus, nous avons observé que la tension et le rayon des fibres augmentent légèrement avec leur longueur. L'organisation et les propriétés mécaniques du cytosquelette peuvent donc être contrôlées par des substrats micro-structurés avec des intervalles non-adhésifs adaptés.

Le rayon des fibres périphériques vient de la compétition entre la tension de ligne et tension de surface, mais le rôle que joue la myosine dans cet équilibre est encore mal compris. Nous avons donc étudié comment cet équilibre était modifié lorsque la myosine était inhibée. Nous avons observé une diminution de la courbure des fibres et des forces de traction, due à une moindre baisse de la tension de ligne par rapport à la tension de surface. Cela indique une contribution indépendante de la myosine à la tension de ligne. Nous en proposons un modèle basé sur une association de l'élasticité des fibres et de l'activité de la myosine. Ce modèle reproduit la dynamique de la forme des cellules en réponse à une diminution de la contractilité, et permet d'estimer la dose d'élasticité intrinsèque à chaque fibre.

Afin de déterminer ce qui contrôle l'élasticité de ces fibres, nous avons mis au point un protocole basé sur la micromanipulation de fibres partiellement isolées. Un micro-levier flexible est utilisé pour mesurer la force nécessaire pour déformer transversalement de la fibre. La réponse de la fibre est représentée par un modèle d'un solide à 3 paramètres (1 ressort en série avec un élément Kelvin-Voigt), et peut être séparée en 2 régimes distincts. Le premier est une réponse élastique à une traction rapide. Le second est une réponse viscoélastique à une relaxation lente. Les coefficients élastiques et viscoélastiques sont extraits des courbes force-élongation et de la vitesse d'élongation pendant la relaxation. Inhiber la myosine a conduit à une diminution de la tension active, mais n'a pas eu d'effets évidents sur l'élasticité. Ces résultats montrent que l'activité de la myosine ne détermine qu'en partie la réponse mécanique des fibres de stress périphériques à une contrainte extérieure mécanique (déformation) ou géométrique (zone adhésive limitée).

Mots-clés actine, myosine, élasticité, contractilité, forces de traction, adhésions, fibroblastes

Abstract

Many cellular processes require or depend on mechanical feedback from the cell's microenvironment. For example, the local organization of the actin cytoskeleton is known to adapt to the physical properties of the extracellular matrix. To gain better understanding of the mechanisms controlling this process, we have studied the particular case of peripheral stress fibers, thick concave contractile bundles of actin filaments. We have employed micropatterned adhesive substrates to constrain cell shape and adhesion layout. We have then used fluorescence microscopy, traction force microscopy and cantilever-based force measurements to experimentally characterize the assembly and mechanical tension of these peripheral stress fibers. We combined these experimental data with numerical simulations of cell shape and cell tension to propose a general mechanical model of stress fiber behavior.

We first identified the formation of peripheral stress fibers as significant of a behavioral switch triggered by non-adhesive gaps in the substrate geometry. These bundles indeed form above a threshold distance of 3-4μm, necessary to stimulate adhesion maturation, and lead to a redirection of cellular tension parallel to the cell edge. Additional analysis of cells on rigid and soft substrates showed that the radius and tension of peripheral bundles weakly increase with spanning distance. Thus both the cytoskeleton local organization and its mechanical properties can be controlled to some extent by non-adhesive features in substrate geometry.

The peripheral fibers' concave curvature results from the balance of the line and surface tensions. However, the nature of these forces, and in particular the contribution of myosin-dependent contractility, are not clear. To get insight into this force balance, we inhibited myosin activity and monitored the shape and tension responses. We found that myosin inhibition led to a decrease in the traction forces and an increase in arc radius, indicating that line tension dropped to a lesser extent than surface tension. These results suggest a myosin-independent component in the tension of peripheral arcs. We propose a simple physical model in which the line tension is the sum of a myosin-dependent active component and of a passive elastic component. Numerical simulations of this model reproduce well the measured shape dynamics and allow estimating the relative contributions of elasticity and contractility to the arc line tension.

We then developed an alternative setup to directly probe the elasticity of semi-isolated peripheral fibers, using micromanipulation techniques. A soft cantilever was used to measure the force with which the fiber resisted a transverse deformation. The overall mechanical response of the fiber can be represented by a 3-parameter-solid model, i.e. a spring in series with a Kelvin-Voigt unit. The response was separated into two regimes: first a fast traction during which elastic response dominated, followed by a viscoelastic relaxation. The elastic and viscoelastic coefficients were extracted from the force-elongation curves and from the elongation velocity during relaxation. Inhibiting myosin activity decreased the active pre-tension, but had no clear effect on the elasticity. Our results show that myosin is an important actor, but not the only one, in the response of peripheral fibers to external mechanical constraints (active deformation) or geometrical constraints (limited adhesive area).

Keywords actin, myosin, adhesions, elasticity, contractility, traction forces, fibroblasts

Contents

Remerciements **vii**

Résumé **ix**

Abstract **xi**

Introduction **1**

1 Biophysical Background **5**
- 1.1 The cell, a mechanosensitive unit 5
- 1.2 The cell cytoskeleton and cell adhesions 7
  - 1.2.1 Actin 7
  - 1.2.2 Myosin II 11
  - 1.2.3 Cell-matrix adhesion complexes 14
  - 1.2.4 Stress fibers 15
- 1.3 Traction forces 19
  - 1.3.1 Cellular generation of traction forces 19
  - 1.3.2 Measuring traction forces and cell mechanical tension 20
- 1.4 Influence of ECM properties on cell function 22
  - 1.4.1 Effet of the matrix' rigidity 22
  - 1.4.2 Effect of the matrix' adhesive geometry 23
- 1.5 Mechanical coupling of cell shape and cell tension 25
- 1.6 Viscoelastic models of the cell and the cytoskeleton 27
- 1.7 Research aims in context 30

2 Materials and Methods **31**
- 2.1 Biology 31
  - 2.1.1 Cell Culture 31
  - 2.1.2 Experimental protocols 31
  - 2.1.3 Chemical compounds to alter myosin activity 33
- 2.2 Microfabrication of patterned substrates 33
  - 2.2.1 Photolithography on glass substrates 34
  - 2.2.2 Polyacrylamide gel fabrication 34
  - 2.2.3 3-dimensional PDMS pattern fabrication 35
- 2.3 Optical Microscopy 39

2.3.1 Wide-field microscopy . . . 39
2.3.2 Traction Force Microscopy . . . 40
2.4 Force Spectroscopy . . . 41
2.4.1 Atomic Force Microscopy for gel stiffness measurements . . . 41
2.4.2 SU-8 cantilevers for fiber tension measurements . . . 41
2.5 Image processing and analysis . . . 42
2.5.1 Image treatment . . . 42
2.5.2 Traction Force Microscopy analysis . . . 44
2.6 Numerical methods . . . 46

3 ECM geometry triggers a reorganization of the cytoskeleton 47
3.1 A length maturation threshold . . . 48
3.1.1 Methods . . . 50
3.1.2 Cytoskeleton organization controlled by discrete adhesive patterns . 50
3.1.3 Evidence for an actin length threshold controlling the maturation of focal adhesions . . . 54
3.1.4 Mechanism of bridge formation . . . 57
3.2 A geometry-dependent force balance . . . 60
3.2.1 Force distribution on discrete adhesive patterns . . . 60
3.2.2 A contour model to describe how forces depend on geometry . . . 63
3.3 Discussion . . . 66

4 Contractile elastic arcs define cell shape 69
4.1 Methods . . . 70
4.1.1 Traction force microscopy . . . 70
4.1.2 Cantilever-based measurements of fiber tension . . . 71
4.2 Experimental results . . . 72
4.2.1 Shape response to myosin inhibition . . . 72
4.2.2 Fiber tension measurement . . . 73
4.2.3 Comparison of line tension measurement techniques . . . 77
4.3 Model of elastic contractile arcs . . . 79
4.3.1 Description of the elastic contractile bundle model . . . 79
4.3.2 Fitting the model to experimental data . . . 81
4.4 Discussion . . . 85
4.4.1 Diversity of shape response . . . 85
4.4.2 Cytoskeletal remodeling during myosin inhibition . . . 86
4.4.3 Assumption of constant arc elasticity . . . 86

5 Mechanical properties of *in situ* semi-isolated fibers 91
5.1 Methods . . . 92
5.1.1 Experimental setup for fiber isolation and deformation . . . 92
5.1.2 Experimental protocol . . . 92
5.1.3 Derivation of model equations . . . 94
5.2 Results from transverse fiber deformation . . . 97
5.2.1 Elastic response of a fiber under traction . . . 97

5.2.2 Viscoelastic relaxation over short time scales 100
5.3 Discussion 103
5.3.1 Validity of a 3-parameter-solid model 103
5.3.2 Dependence of mechanical properties on myosin activity 104
5.3.3 Deviations from linear viscoelastic behavior 105

6 Conclusion and Perspectives **109**
6.1 Summary of results 109
6.2 Discussion 110
6.3 Perspectives 113
6.3.1 Combining active and passive force measurements 113
6.3.2 Further Outlooks 116

Bibliography **119**

Curriculum Vitae **132**

Introduction

Context and aims of research

Over the past two decades, the role of mechanical signals in biological processes, both normal and pathological, have been increasingly recognized. Researchers have been dissecting the many force-dependent processes at all scales, from the molecular scale to the cell and tissue scale, as well as their interplay with biochemical signaling loops. For instance, the mechanical interactions between a cell and its micro-environment lead to stiffness-dependent cell behavior such as growth, polarization or differentiation. Cell morphology is also a key regulator of proper cell function, and together with intracellular tension, conditions the cell's ability to migrate in a given direction (e.g. to the location of a wound), to deform (e.g. in inflating lungs) or on the contrary to resist deformation (e.g. under pulsatile flow). Understanding how cell morphology and cell tension might be impacted by the physical properties of the micro-environment (geometry, rigidity, curvature . . .) is therefore crucial to the building of a more complete picture of biomechanical and biological processes, in particular when they become dysfunctional, as in abnormal embryonic development or in cancer. Such knowledge will also allow in turn to engineer adapted substrates for cellular studies and cell, tissue or organ culture.

Changes in cell shape or cell stiffness come about from the rearrangement of the cell cytoskeleton. The cytoskeleton is a complex cellular network of several biopolymers, often associated to molecular motors, responsible for maintaining the cell's morphological integrity and mechanical tension, much like muscles and bones do in our bodies but at the cellular scale. The different components of the cytoskeleton are able to bear tensile or compressive forces, but also to exert forces on their environment. The biology of the different cytoskeletal structures have been studied at length, such that the assembly/disassembly mechanism, crosslinkers and regulatory proteins are known. However, this knowledge has not been systematically connected to the mechanical role of the cytoskeleton. Questions such as if and how cells have a sense of distances and size, or a memory of shape are not settled. Several models have been developed to understand the cell and the cytoskeleton from a physical point of view, focusing for instance on the viscoelastic properties of the biopolymers, or describing the cell as a whole as an active viscoelastic gel. Progress has also been made in understanding the stick-slip mode of force transmission at cell-matrix adhesions. Yet, how the organization of the various cytoskeleton structures and their mechanical properties arise are far from being fully understood, more so because of the complex interplay between cell morphology, cell tension and other external parameters.

One particular cytoskeletal structure observed in adherent cells under high isometric tension are stress fibers. Stress fibers are involved in many processes such as remodeling of the extra cellular matrix or cell migration. They are generally speaking very responsive to mechanical stimuli, and it is therefore essential to better define their mechanical properties. Among the different classes of stress fibers, peripheral actin-myosin bundles bridging distant adhesions have been observed in cells spread on homogeneous substrates, but are more commonly observed in cells spread on micropatterned substrates. The cytoskeletal arrangement on patterned substrates significantly differs from that on an uniform adhesive layout, and it is interesting to clarify what brings about the changes, and how they are controlled at a mechanistic level. These bridges being connected to cell-matrix adhesions as they assemble, their formation is directly dependent on the adhesive layout.

The aim of the work undertaken over the past 4 years is therefore to describe the formation and dynamic behavior of peripheral stress fibers from a physical point of view, characterize their mechanical properties, and determine how these are modified by extracellular constraints (adhesive geometry) and intracellular parameters (global cell contractility). To this end, we make extensive use of micropatterning techniques to systematically constrain cell spreading and cell adhesive area. We then characterize peripheral stress fibers by fluorescent imaging of the cytoskeleton, traction force magnitude maps and response to mechanical deformations. We combine these experimental measurements with an analytical model of stress fiber tension, and perform numerical simulations of the dynamics of cell shape and cell tension. We believe that the findings on how substrate geometry, cell morphology and intracellular tension are interrelated will be relevant to other cytoskeletal systems of various cell types.

Outline

The main body of this thesis is structured in 6 chapters.

Chapter 1 gives some background to the biological and biophysical aspects of the research presented in this work. It defines the main cellular components that participate in determining cell morphology and cell mechanical tension. Force measurement techniques and some modeling approaches relevant to the study of the mechanical properties of stress fibers are also presented.

Chapter 2 describes the experimental procedures used throughout this thesis. Standard protocols used for cell culture, cell imaging and image processing are given. The techniques used for the microfabrication of patterned substrates are detailed in length, as well as traction force microscopy and cantilever-based force measurements. Additional methodological details which are specific to a particular content are given at the beginning of the corresponding chapters.

In **Chapter 3**, we present an hypothesis on how the substrate adhesive geometry can control cytoskeletal remodeling, the formation of peripheral stress fibers and adhesion maturation. We provide experimental evidence supporting the hypothesis, based on the cytoskeleton organization of cells spread on patterned glass substrates. We further examine the mechanism behind this geometrical control of cytoskeleton organization by resorting to traction force microscopy on patterned soft substrates.

From the evidence that cell tension and cell shape are coupled, we question how this balance is dynamically controlled by myosin activity in **Chapter 4**. For this, we inhibit contractility in full-spread cells and observe how their shape and tension change. We use a combination of traction force microscopy and analytical modeling of shape and tension dynamics to extract fiber tension values and determine the elasticity peripheral arcs.

Chapter 5 presents a new approach to measure viscoelastic properties of semi-isolated fibers, using ultra-soft cantilevers to apply transverse deformations to these fibers *in situ*. We use a 3-parameter-solid model to analyze the force-elongation curves and extract the fibers' spring constant and pre-tension. We investigate the dependence of those values on myosin activity by using contractility inhibiting drugs. We then investigate the involvement of motors in fiber relaxation.

Chapter 6 summarizes the results and discusses the general outcome. A possible direction for future work is presented, in which we attempt to combine the different techniques used, namely traction force microscopy with active fiber deformation.

Chapter 1

Biophysical Background

1.1 The cell, a mechanosensitive unit

The cell is the smallest functional unit of organisms. It is where the most fundamental reactions of life take place, such as the replication and transcription of DNA in the nucleus, RNA translation to proteins by the ribosomes in the cytoplasm, ATP synthesis in the mitochondria etc. There is also a lot of traffic in the cytoplasm (the fluid composing most of the cell's volume) of molecules, proteins and vesicles, carried by motor units on polymer structures formed by the cell cytoskeleton. These movements and reactions are tightly coordinated within the cell and, at a larger scale, within a tissue or organ, and this requires the cell to communicate with its local micro-environment. Communication can take the form of biochemical signals, electrical signals or mechanical signals. Mechanical signals at the molecular scale include for example force-induced activation/recruitment of proteins, the stretching of polymers and proteins, or the reinforcement of molecular bonds under high load. At the cellular level, it determines cell behavior such as cell migration along a gradient of rigidity or cell alignment under shear flow. The capacity to sense, transmit and react to mechanical signals is essential to many cellular processes such as proliferation, differentiation and migration. Fibroblasts, which actively interact with their surrounding environment, are an interesting model system to study how cell mechanical properties and cell morphology are co-regulated in such processes. We detail in this chapter some essential elements to this study, including the cytoskeleton and the cell adhesions, which are key components of the cell's mechanosensitive system.

Fibroblasts

Connective tissue is a type of tissue, rich in extracellular matrix fibers, which supports, protects, joins together or isolates other tissues. For instance, loose connective tissue surrounds blood vessels and nerves. Dense connective tissue is a main component of tendons and ligaments. Other special connective tissues are bone and cartilage. Fibroblasts are the most common cells found in connective tissue. Immature fibroblasts (also called mesenchymal stem cells) can differentiate into smooth-muscle cells or fat cells, or reversibly transform to cartilage cells (chondrocytes). Fibroblasts are isolated in the tissue (not adjacent to other cells) being surrounded by extracellular matrix (ECM) (Figure 1.1a). They have the faculty of secreting some ECM fibers, mainly type I or type III collagen. Their ability to secrete, but also remodel and degrade the ECM make fibroblasts essential in would healing processes. They migrate to sites of injuries, and are able to close the wound thanks to their ECM production capacities. The activity of fibroblasts also contributes to regulate interstitial fluid volume and pressure. Dysfunctions in these roles resulting in excess or diminished ECM deposition can lead to an impaired injury response [Alberts, 2002].

Fibroblasts can have very diverse morphologies. When cultured on 2-dimensional substrates in static conditions, they flatten, and extend spike-like arms in many directions (Figure 1.1b), whereas under shear flow, they will elongate and orient parallel to the flow. Their shape is important for communication with the ECM and neighboring cells, as well as for migration. A key factor in fibroblast shape and function is their attachment to the extracellular matrix through cell-matrix adhesion complexes, through which they exert forces of several hundred pN on the ECM. Their contractility and high degree of attachment to the ECM make these cells ideal to study the interplay between substrate geometry, cell shape and cell mechanical properties, which is the focus of this work.

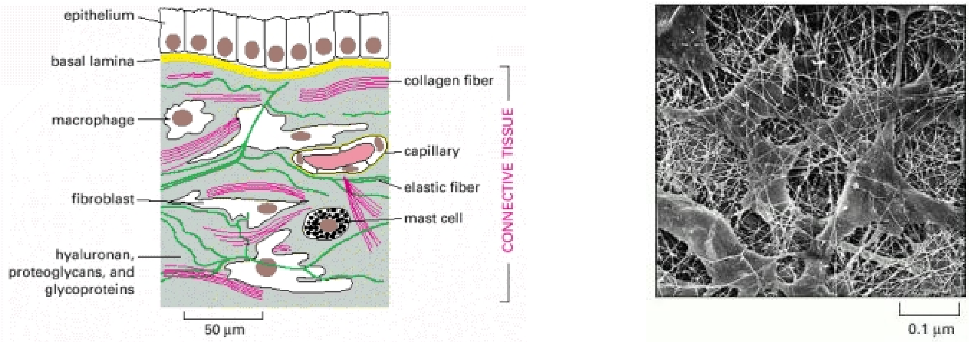

(a) **(b)**

Figure 1.1: a) The connective tissue underlying an epithelium. This tissue contains a variety of cells and extracellular matrix components. The predominant cell type is the fibroblast, which secretes abundant extracellular matrix. b) Fibroblasts in connective tissue. This scanning electron micrograph shows tissue from the cornea of a rat. The extracellular matrix surrounding the fibroblasts is composed largely of collagen fibrils (From T. Nishida et al., Invest. Ophthalmol. Vis. Sci. 29:1887–1890, 1988. ©Association for Research in Vision and Opthalmology.). Reproduced from "The Extracellular Matrix of Animals." in Alberts [2002].

1.2 The cell cytoskeleton and cell adhesions

Two key players in the cell's mechanosensing capacities are the cell cytoskeleton and the cell-matrix adhesion complexes. The term cytoskeleton usually designates all the three different types of biopolymer which compose the cell, namely actin filaments, intermediate filaments and microtubules. Actin filaments play a major role in cell motility and cell division. Cell growth and cell shape are also controlled essentially by actin-based structures. The focus of this thesis is on such structures called stress fibers, parallel bundles composed of actin and myosin filaments. Since microtubules and intermediate filaments are not the purpose of this work, we will abusively use the term *cytoskeleton* to designate specifically acto-myosin networks, for better readability.

1.2.1 Actin

Actin filaments

Actin is one of the most abundant protein in cells. It is a highly conserved protein among eukaryotes, and an actin homologue also exists in bacteria. It is present both in globular (G-actin) and in filamentous (F-actin) forms in the cytoplasm. G-actin monomers associate together to form polar helical actin filaments, of diameter 7nm and with a persistence length of 17μm. The polarity of the filaments comes from different association and dissociation rates of G-actin at each end of the filament. These rates depend on the concentration of ATP-G-actin and ADP-G-actin, and under usual cytoplasmic concentrations, F-actin polymerizes spontaneously at the barbed end (or + end), and depolymerizes at the pointed end (or - end). Polymerization occurs through the addition of ATP-G-actin at the barbed end. The ATP is then rapidly hydrolyzed into ADP. ADP-G-actin detaches from the filament at the pointed end (Figure 1.2). If the polymerization rate and the barbed end balances the depolymerization rate at the pointed end, the filament length is constant, leading to a treadmilling effect.

Regulatory proteins of actin polymerization

The assembly and disassembly of actin filaments and of actin networks, is not only a function of monomer concentrations but on the contrary is locally very tightly controlled by many regulatory proteins. Filament nucleation is promoted by Arp2/3 for branched networks, and formins for aligned networks. Formins also increases polymerization rate. Filaments are then either stabilized by capping proteins (preventing disassembly), or severed by ADF/cofilin. Spontaneous depolymerization can also be enhanced by profilin, a protein that sequesters G-actin, reducing the number of available monomers. The balance between these stabilizing and destabilizing proteins determines the dynamics of the local actin network, and is controlled further upstream by other proteins, such as Rho GTPases, which do not interact directly with actin. Some of the proteins involved in the regulation and assembly of actin are shown in Figure 1.3 and reviewed in Pollard [2007].

Actin networks

Actin polymerization alone is sufficient to generate protrusive forces, for instance at the leading edge of a migrating cell, or in the comet tail that propels some bacteria. When assembled into networks and associated to other proteins, actin filaments serve many other functions. For example, highly dynamic thin criss-crossed networks or thin parallel spikes create cellular protrusions called lamellipodia and filipodia that are used to explore the environment or drive migration. Branched actin network can also form a rigid cortex that supports the cell plasma membrane. At the end of cell division, thick actin bundles form the cytokinetic ring which eventually separates the two daughter cells. The architecture of F-actin assembly is determined by the nature of the cross-linking proteins. For instance α-actinin and fascin bind filaments parallel to each other, while filamin or Arp2/3 will bind filaments with large angles between them, forming non-aligned networks (Figure 1.4, and reviewed in Fletcher and Mullins [2010]).

Lamellipodium and lamellum

As briefly mentioned above, the architecture of the actin networks and the localization of adhesion complexes are spatially regulated in the cell. Several sub-cellular regions can be distinguished. At the leading edge of the cell, there is a thin bi-dimensional sheet of criss-crossed actin filaments ($\sim$300nm in height) called the lamellipodium (LP). Filaments are branched by Arp2/3 at a 70° angle, as in the top-left panel of Figure 1.4. In this area, the balance between polymerization and depolymerization leads to an effective treadmilling of actin filaments, in which each filament keeps a constant length. The lamellipodium is involved in cell motility and environment exploration. This is done partly through the nascent adhesions forming beneath it. Behind the lamellipodium, the actin is more dense and is bundled into fibers, in which myosin becomes incorporated so that contraction is possible. This region, the lamellum (LM), is much thicker (up to 3μm high). The LP/LM interface is marked by the transition from cross-linked to bundled network and therefore easily visible on phase contrast and fluorescence images or electron micrographs (Figure 1.5). Timelapse imaging can be used to observe the continuous advance of this interface with each successive wave of cell protrusion. The dynamic nature of these networks and of the associated adhesions is essential for proper cell spreading and cell motility.

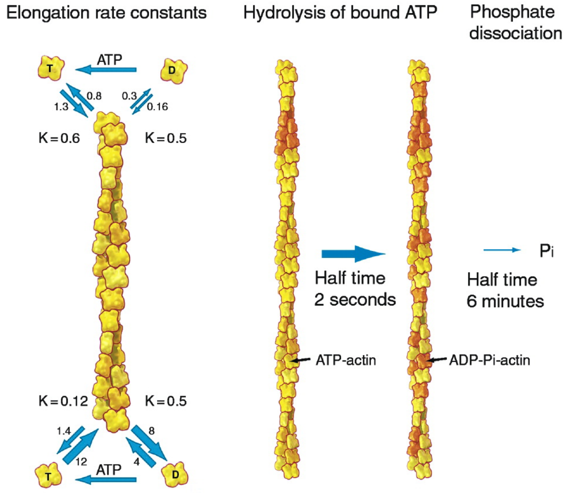
Elongation rate constants
Hydrolysis of bound ATP
Phosphate dissociation
ATP
T
D
1.3
0.8
0.3
0.16
K=0.6
K=0.5
Half time 2 seconds
Pi
Half time 6 minutes
ATP-actin
ADP-Pi-actin
K=0.12
K=0.5
1.4
12
8
4
ATP
T
D

Figure 1.2: Actin Filament Elongation, Hydrolysis of ATP and Phosphate dissociation. ATP-actin (“T”) monomers and ADP-actin (“D”) monomers associate and dissociate from the filament at different rates at the barbed end (bottom) or the pointed end (top). The association rate constants are in $\mu M^{-1}.s^{-1}$, dissociation rate constants in s^{-1}. The ratio of the dissociation to association rate constants gives K, the dissociation equilibrium constant, in µM. ATP-actin hydrolysis is fast but the dissociation of the phosphate is slow. Adapted from Pollard and Borisy [2003], from original artwork by Graham Johnson in “Cell Biology” by T.D. Pollard and W.C. Earnshaw, W.B.Saunders, [2002].

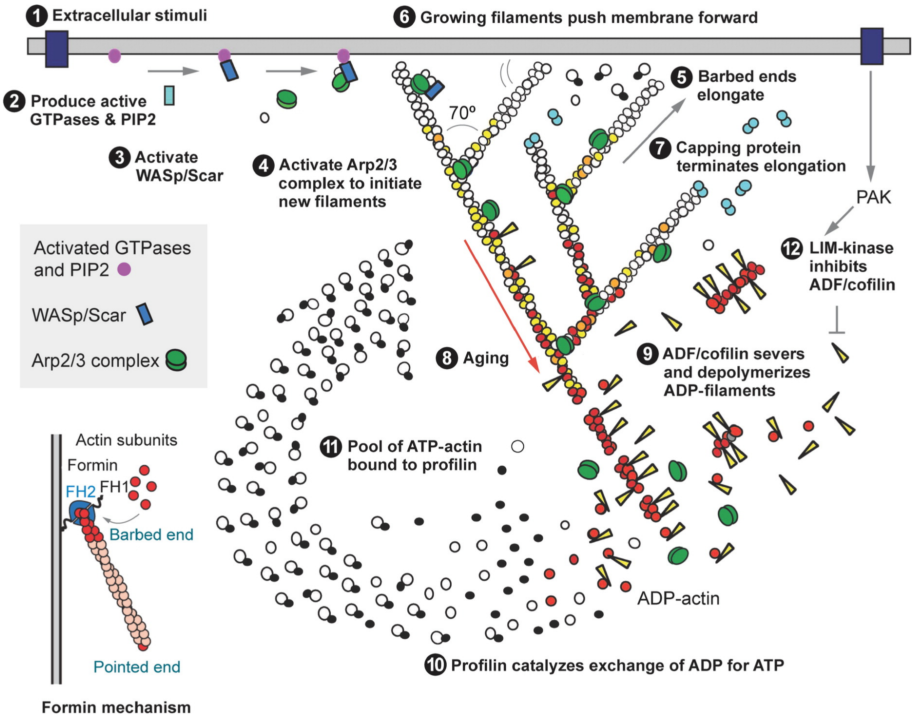
① Extracellular stimuli
⑥ Growing filaments push membrane forward
② Produce active GTPases & PIP2
③ Activate WASp/Scar
④ Activate Arp2/3 complex to initiate new filaments
70°
⑤ Barbed ends elongate
⑦ Capping protein terminates elongation
PAK
⑫ LIM-kinase inhibits ADF/cofilin
Activated GTPases and PIP2
WASp/Scar
Arp2/3 complex
⑧ Aging
⑨ ADF/cofilin severs and depolymerizes ADP-filaments
Actin subunits
Formin
FH2
FH1
Barbed end
Pointed end
Formin mechanism
⑪ Pool of ATP-actin bound to profilin
ADP-actin
⑩ Profilin catalyzes exchange of ADP for ATP

Pollard TD. 2007.
Annu. Rev. Biophys. Biomol. Struct. 36:451–77

Figure 1.3: Overview of actin regulatory proteins. Arp2/3 promotes dendritic nucleation, while formins promote parallel nucleation. A branched actin filament elongates at its barbed end, towards the leading edge of the cell until it is capped. Along the existing filament, ATP-actin (white) is hydrolyzed to ADP-actin (green). GTPases, PIP2, WASp/Scar, PAK and LIM-Kinase are enzymes regulating the activity of actin-binding proteins. Reproduced from Pollard [2007].

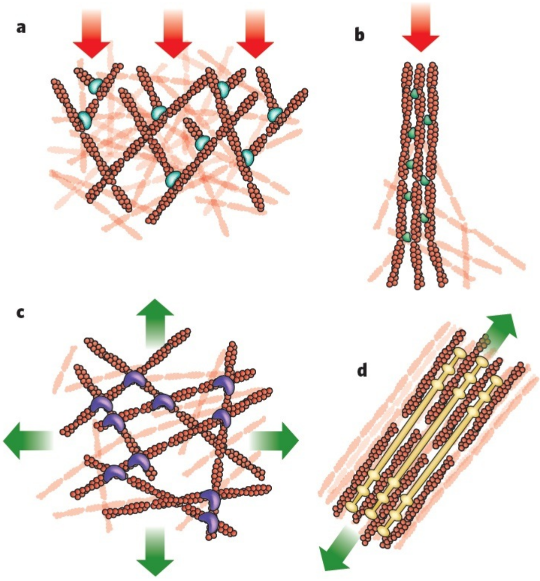

Figure 1.4: Form meets function. **a**, Branched actin-filament networks push against the plasma membrane as they generate protrusions, thereby encountering an inward force of compression (red arrows). **b**, Filaments bundled by fascin into filopodia also generate protrusive forces as they extend from the cell body, encountering similar compressive force (red arrows). **c**, Cortical networks (that is, non-aligned networks) cross-linked by filamin form below the plasma membrane and carry tension loads in multiple directions (green arrows). **d**, Stress fibers form from bundled actin filaments, shown here associated with myosin, and generate tension against cell adhesions to the extracellular matrix (green arrows). Reproduced from Fletcher and Mullins [2010].

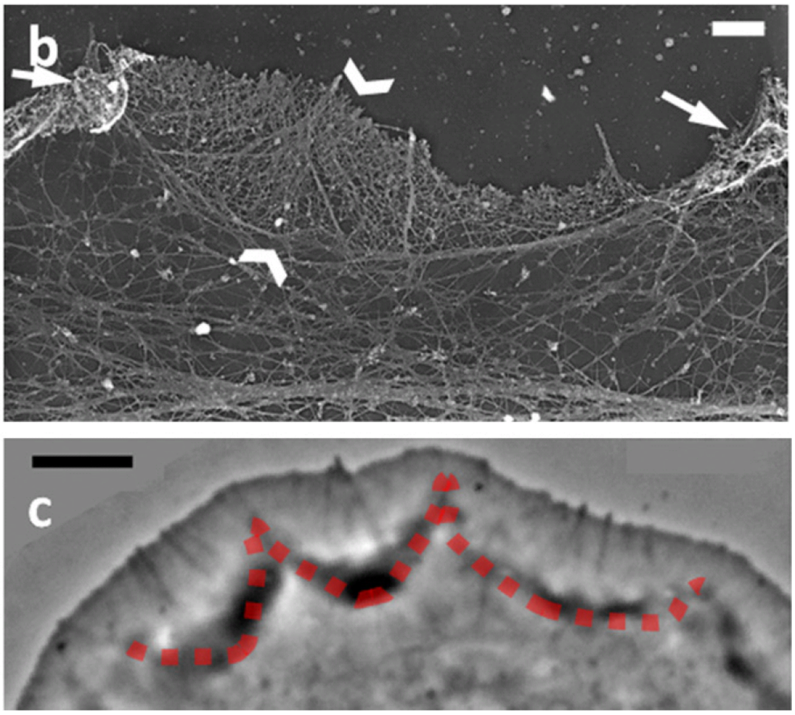

Figure 1.5: (Top) Election micrograph of a *Xenopus* fibroblast in which the transition from the branched actin in the lamellipodium (in between arrowheads) and the bundled actin of the lamellum is clearly visible. (Bottom) Phase contrast image showing the lamellipodium/lamellum interface, delineated in red. Reproduced from Shemesh et al. [2009].

1.2.2 Myosin II

Structure and power-stroke cycle of myosin

Associated to the different polymers of the cytoskeleton are many classes of molecular motors, which bind, cross-link, and move across the filaments. They serve various functions ranging from cargo transportation to force generation. For instance, myosins are the motors responsible for muscle contraction. Myosin is in fact a super-family of molecular motors which bind to actin and convert the energy of ATP-hydrolysis into work to move along filaments (Figure 1.6). They are all made of a head domain (the motor domain), which contains actin binding sites and ATP-binding sites, a tail domain that binds specific cargoes or substrates, and light chains which constitute the lever region. The number of head domains, the length of the tail domains and the number of light chains varies from one isoform to the next, thereby modulating the way myosin advances along actin filaments. The cycle leading to the power-stroke (force generator) is shown in Figure 1.7.

1) At the start of the cycle, myosin is attached to actin in a *rigor conformation.*

2) Myosin binding to ATP triggers the release of the motor head from the filament.

3) The lever arm is cocked, thereby being displaced along the filament. This is followed by hydrolysis of ATP, producing ADP and an inorganic phosphate which remain bound to the myosin head.

4) In this configuration, the weak affinity for myosin to actin leads to attachment to the filament and release of the phosphate. This leads to a conformational changes of the lever arm (the actual power stroke).

5) The myosin head remains in this configuration while the ADP is released, thereby closing the cycle.

In fibroblasts, as in all other non-muscle cells, the **non-muscle myosin II** (NMM II) isoform is the main type of myosin present. NMM II binds to actin filaments, composing the dense acto-myosin cytoskeleton. NMM II possesses two head domains, two light chains called essential light chain and regulatory light chain, and a coiled heavy chain. The reversible phosphorylation of the regulatory light chains is involved in the control of myosin activity. The essential light chains are not known to be phosphorylated, but instead serve to stabilize the heavy chains. Heavy chains can get intertwined together to form bipolar myosin thick filaments (Figure 1.8). Three isoforms of non-muscle myosin II have been identified. The heavy chain of each isoform (myosin IIA, myosin IIB and myosin IIC)

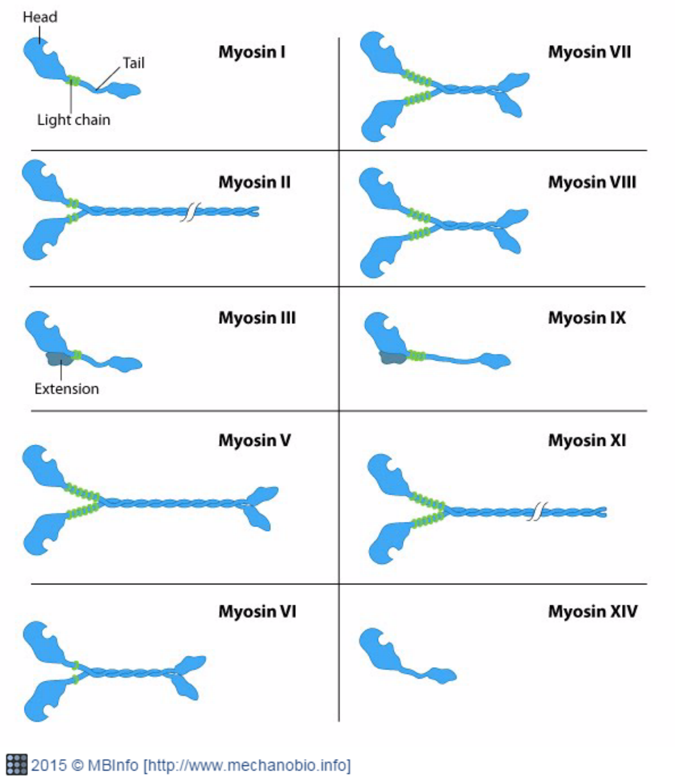
Head
Tail
Light chain
Myosin I
Myosin VII
Myosin II
Myosin VIII
Myosin III
Extension
Myosin IX
Myosin V
Myosin XI
Myosin VI
Myosin XIV
2015 © MBInfo [http://www.mechanobio.info]

Figure 1.6: The myosin super-family of motor proteins. All members contain one or two head domains, several light chains (green) and tail domains that can form coiled dimers. Reproduced with permission from the MBInfo Wiki.

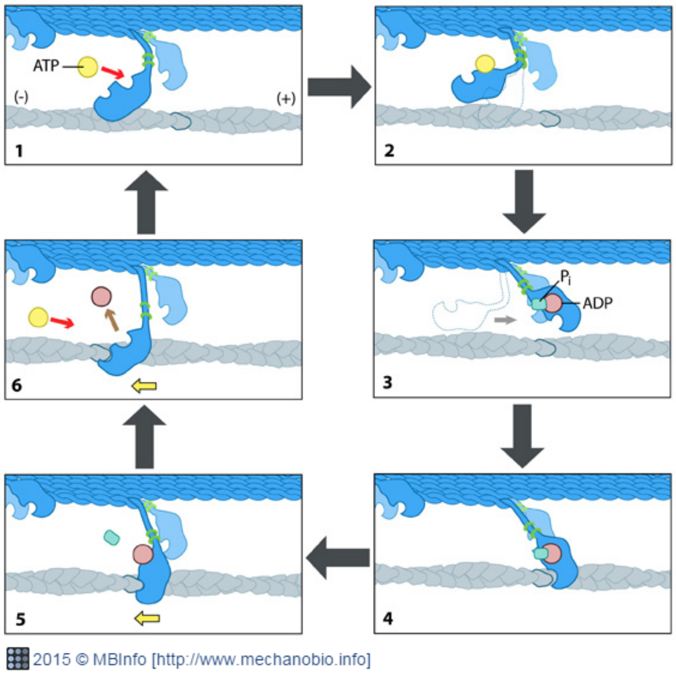
ATP
(-)
(+)
1
2
Pi
ADP
3
4
5
6
2015 © MBInfo [http://www.mechanobio.info]

Figure 1.7: The non-muscle myosin II crossbridge cycle. This sketch shows the steps leading to the power-stroke mechanism and to myosin movement along actin filaments. Reproduced with permission from the MBInfo Wiki.

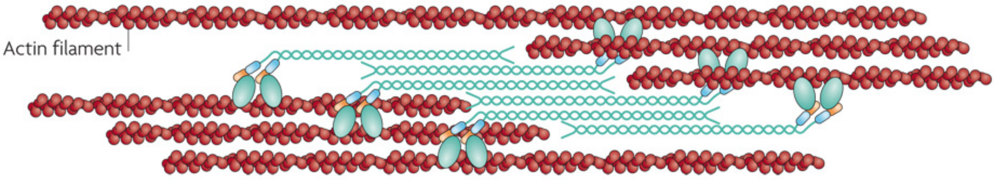

Figure 1.8: Myosin II thick filaments. NMM II molecules assemble into bipolar filaments through interactions between their rod domains. These filaments bind to actin through their head domains and the ATPase activity of the head enables a conformational change that moves actin filaments in an anti-parallel manner. Bipolar myosin filaments link actin filaments together in thick bundles that form cellular structures such as stress fibers. Reproduced from Vicente-Manzanares et al. [2009b].

is encoded by a different gene. This small difference is sufficient to modify their affinity to actin and their duty ratio (i.e the fraction of time myosin remains attached to actin, typically around 0.2 for myosin IIa and 0.8 for myosin IIb [Rosenfeld et al., 2003]), leading to minor differences in their activity and localization within cells [Vicente-Manzanares et al., 2009b].

Contractility and Force-velocity relationship

Contractility originates from the movement of myosin motor heads on actin filaments. Powered by ATP hydrolysis, myosin II advances non-processively towards the barbed ends of actin filaments by steps of 8.5nm. When two heads bind to two anti-parallel actin filaments (i.e. filaments of opposite polarity), the power stroke of each motor head induces the sliding in opposite directions of the filaments rather than motor displacement. This mechanism, in addition to the fact that filaments buckle under compression, leads to overall bundle contraction [Lenz et al., 2012]. The velocity of contraction will depend on the load opposing motor activity. It is indeed well known that muscle contraction velocity is inversely proportional to the load (Hill model for isometric contraction [Hill, 1938]). The same relationship exists for motor filaments in non-muscle cells. For our purpose, a simplified linearized inverse relationship is sufficient to capture the physical behavior of acto-myosin bundles: $F = F_s(1 - v/v_0)$. The stall force F_s is the maximal force that one filament of motors can exert. Motor velocity v is zero at the stall force. Reciprocally, at the maximum velocity v_0, motors exert zero force. For a single motor, the stall force is $F_s \sim 1.7$pN, and the maximal velocity (unloaded velocity) is expected to be between 0.01µm/s and 0.3µm/s [Howard, 2001]. In a recent *in vitro* study of reconstituted actin-myosin networks, Thoresen et al. [2011] showed that in fact non-identical motors with some dispersion in their unloaded velocities is required to contract actin myosin networks, because contraction can only occur if there is a slight imbalance of forces. These authors also propose another requirement for contraction, namely that the density of motors be in an intermediate range, since at low density, the motors would detach too often, while at high densities, dense crosslinking would prevent the sliding of filaments [Lenz et al., 2012].

1.2.3 Cell-matrix adhesion complexes

Fibroblasts do not float around in their environment, but are instead strongly attached to the surrounding extracellular matrix by adhesion complexes that they create at the cell-matrix interface. Cells can also connect to other cells through different types of cell-cell adhesions, but in fibroblasts, cell-matrix adhesions are dominant, so we will focus only on the latter. These are based on the clustering and activation of transmembrane proteins called integrins. Integrins are heterodimeric proteins, composed of two transmembrane glycoproteins chains α and β. There are several subtypes of α and β units, and each unit couple has specific interactions with certain ECM proteins. The extracellular domains of integrins bind to ECM protein filaments (collagen, fibronectin), while the intracellular domains bind to many adhesion proteins and, indirectly, to the actin cytoskeleton. The integrins are the first layer in the construction of adhesion scaffolds, and their engagement induces signaling pathways that regulate adhesion assembly and disassembly, as well as assembly of actin-based structures [Geiger et al., 2001]. Integrins are also crucial to the mechanosensory function of adhesions. The dynamics of integrin clustering and bond engagement is indeed dependent on the mechanical load. Several studies have shown that the binding of some integrins ($\alpha_5\beta_1$) to ECM ligands follow a catch-bond behavior, i.e. that low forces increase bond lifetime until a certain point (Friedland et al. [2009], Kong et al. [2009] and reviewed in Hoffman et al. [2011]). The optimal force (leading to the strongest bond) for activating $\alpha_5\beta_1$ integrins is below 10pN [Kong et al., 2009, Walcott et al., 2011]. Activation of integrins is also a cooperative process, and thus depends on the number of neighboring integrins clustered together. Interestingly, a recent study has shown that the cooperative binding dynamics of integrins lead to a minimal area of clustering for the formation of nascent adhesions [Coyer et al., 2012]. This minimal area, estimated by nanopatterning techniques to be of $0.11\mu\text{m}^2$, depends on the tension level of the cell, and can therefore be tuned by altering cell contractility. This is an example of how mechanical tension has downstream consequences at the molecular level on the organization and size of cell adhesions and the cytoskeleton.

Denomination	**Shape**	**Size**	**Location**	**Lifetime**
Nascent adhesion	dot-like	<0.25µm	cell edge	< 1 min
Focal complex (FX)	dot-like	<1µm	cell edge	< 5 min
Focal adhesion (FA)	elongated (oval shape)	1-5µm	LP/LM interface	20 min
Fibrillar adhesion	fibrillar	1-10µm	central	min to hrs

Table 1.1: Stages of adhesion complex maturation and their properties. Adapted from Geiger et al. [2001] and Gardel et al. [2010].

The nascent adhesions mentioned above are the first stage of adhesion complexes, which form at the cell periphery. Adhesions then evolve in size, shape and composition as they move further inward. This is summed up in Table 1.1 and Figure 1.9. The importance of mechanosensory processes in this maturation process has been extensively demonstrated, notably in one landmark study, in which Geiger and co-workers showed that mechanical force induced the growth of focal complexes, maintaining a constant stress of 5.5nN/µm [Balaban et al., 2001, Riveline et al., 2001]. Elongated focal complexes are then termed focal adhesions (FA). At this point, their size is no longer correlated with the local force. They are enriched in many proteins that participate in the signaling cascades diffusing from the adhesion sites. The complex scaffolding of adhesion proteins has been reconstituted to the nanoscale using super-resolution fluorescence microscopy by Waterman and colleagues (Kanchanawong et al. [2010] and Figure 1.10), who revealed the highly stratified structure of FAs. Among the proteins identified are a few that together form a molecular clutch, that is that they connect actin filaments to adhesions with a tunable strength, allowing for the transduction of cytoskeletal forces into either protrusion or traction at the leading edge [Gardel et al., 2010]. Talin and vinculin are two such mechanoresponsive molecules, necessary for focal adhesion formation and stabilization: talin first binds to actin, then is stretched under force. This opens up hidden vinculin-binding sites, thus enabling the recruitment of vinculin which stabilizes adhesions [Wolfenson et al., 2009].

1.2.4 Stress fibers

One type of acto-myosin network of particular interest to this work are stress fibers (SF), so called because they are able to bear great amount of stresses. Stress fibers are thick bundles of parallel actin filaments, bound together in a bi-polar arrangement by α-actinin (Figure 1.11).

Classification of stress fibers

Stress fibers are categorized into 3 main classes depending on their structure and localization in the cell. **Dorsal SFs**, also called radial SFs, initiate at the LP/LM interface and elongate radially from the cell periphery, rising towards the cell center. At their distal ends they are connected to focal adhesions, while at their proximal ends they connect to transverse arcs. **Transverse arcs** are myosin-enriched stress fibers, oriented orthogonally to dorsal SFs. The myosin bands alternate with α-actinin. The myosin-powered contractility of transverse arcs drives their centripetal flow, and indirectly, the elongation of dorsal SF. While flowing inward, arcs also move away from the basal side towards the apical side of the cell. Finally, dorsal SFs from two opposite regions of the cell may become

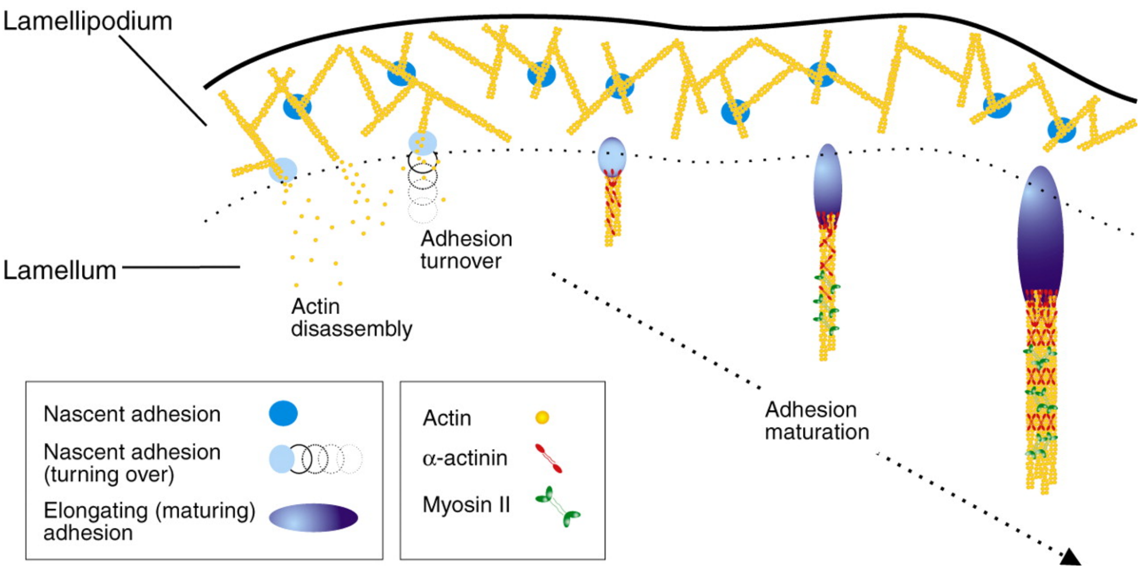
Lamellipodium
Lamellum
Actin disassembly
Adhesion turnover
Adhesion maturation
Nascent adhesion
Nascent adhesion (turning over)
Elongating (maturing) adhesion
Actin
α-actinin
Myosin II

Figure 1.9: "The adhesion lifetime. Adhesions first form in the lamellipodium, where their rate of assembly correlates with the rate of protrusion. As actin disassembles at the rear of the lamellipodium, adhesions turn over. Some adhesions elongate in the region of convergence between the lamellipodium and the lamellum, and mature centripetally along thin actin filaments that are decorated with α-actinin, an actin cross-linker (depicted in red). As the bundles become thicker and more stable owing to enhanced cross-linking, myosin II (depicted in green) enters and the adhesions become larger." Image and legend reproduced from Vicente-Manzanares et al. [2009a].

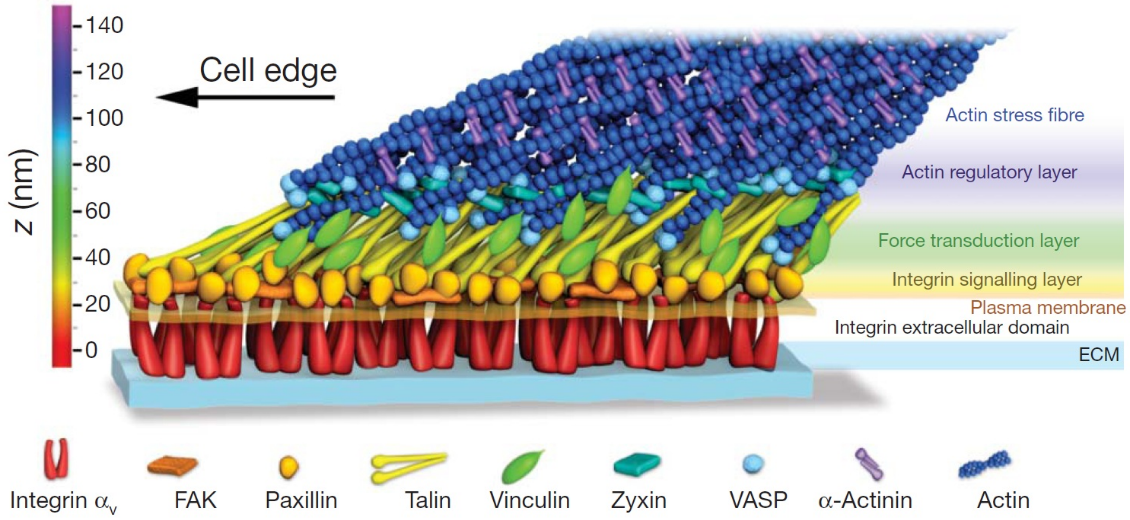
z (nm)
140
120
100
80
60
40
20
0
Cell edge
Actin stress fibre
Actin regulatory layer
Force transduction layer
Integrin signalling layer
Plasma membrane
Integrin extracellular domain
ECM
Integrin α_v
FAK
Paxillin
Talin
Vinculin
Zyxin
VASP
α-Actinin
Actin

Figure 1.10: Schematic of the nanoscale architecture of focal adhesions. The position and height of each molecule was determined by super-resolution microscopy (iPALM), revealing several layers in the organization of FAs. The model does not reflect the actual stoichiometry of the adhesions. Reproduced from Kanchanawong et al. [2010]

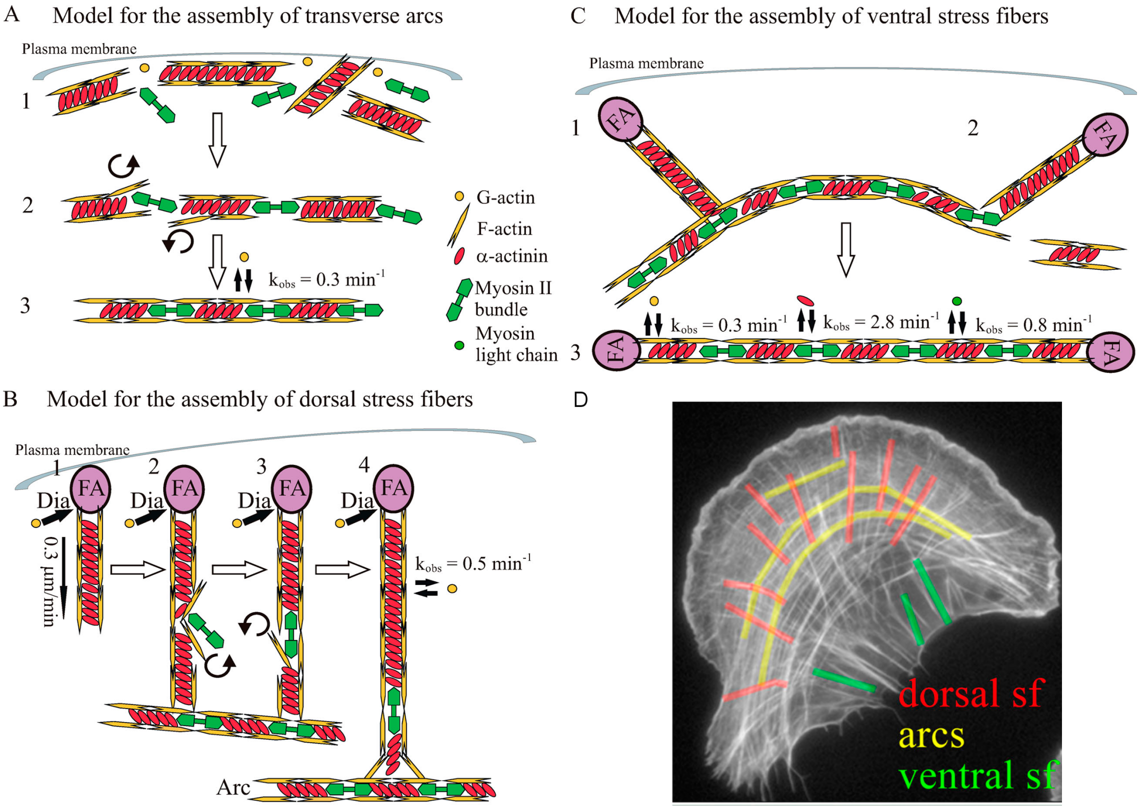
A Model for the assembly of transverse arcs
Plasma membrane
1
2
3
k_{obs} = 0.3 min^{-1}
G-actin
F-actin
α-actinin
Myosin II bundle
Myosin light chain
C Model for the assembly of ventral stress fibers
Plasma membrane
1
2
3
FA
k_{obs} = 0.3 min^{-1}
k_{obs} = 2.8 min^{-1}
k_{obs} = 0.8 min^{-1}
B Model for the assembly of dorsal stress fibers
Plasma membrane
1
2
3
4
Dia
FA
0.3 μm/min
k_{obs} = 0.5 min^{-1}
Arc
D
dorsal sf
arcs
ventral sf

Figure 1.11: Models of SF assembly. (A-C) Sketch of the mechanisms for the assembly of transverse arcs (A) and dorsal SFs (B). Ventral stress fibers result from the end-to-end annealing of dorsals and arcs (C). (D) Stress fibers in a human osteosarcoma (U2OS) cell. Actin filaments were marked with phalloidin. Adapted from Hotulainen and Lappalainen [2006].

connected by an arc that then aligns to form one long **ventral SF**. These SF are stably anchored to focal adhesions and remain on the basal side of the cell. Ventral SFs also contain both α-actinin and myosin, but these proteins do not alternate as in transverse arcs. The formation and function of these stress fibers has been reviewed in Pellegrin and Mellor [2007], Tojkander et al. [2012] and Burridge and Wittchen [2013].

Peripheral arcs are usually not considered a distinct class of stress fibers, not being frequently observed in standard culture conditions. They are similar in composition to transverse arcs. However, they do not flow inward contrary to transverse arcs, and their curvature is opposite to that of arcs, since they are concave with respect to the cell body.

Models of SF assembly

In a landmark study, Hotulainen and Lappalainen [2006] have shown that there are two distinct modes of assembly for stress fibers. While dorsal stress fibers elongate at their distal ends (near focal adhesions) by formin-mediated polymerization, transverse arcs assemble by the association of myosin filaments and existing actin filament fragments nucleated by

Arp2/3 and crosslinked by α-actinin. α-actinin is progressively displaced by myosin filaments intercalating into SFs. They additionally characterized the turnover rates of actin, myosin light-chain and α-actinin in dorsal SF, arcs and ventral SF, and found dissociation rates of the order of 0.3 to 0.5 min^{-1} for actin, close to 1 min^{-1} for myosin light chain, and 2.7min^{-1} for α-actinin.

The formation of transverse arcs has been further investigated by Lippincott-Schwartz and colleagues [Burnette et al., 2011; 2014]. Using super-resolution microscopy, they observed how the myosin-driven condensation of actin filaments from retracting protrusions formed bundles, creating the base for further protrusions. The inward flow of these bundles was markedly slowed down near adhesions, where they connected to dorsal SF. This differential velocity resulting in a concave shaped LP/LM interface. While the interface stays stationary with respect to the cell edge, each individual arc then flows inward and upward, powered by the elongation of dorsal SFs, as already observed by Hotulainen and Lappalainen [2006]. These authors further found that the arcs become enriched in myosin IIa as they progress in the lamellum. Their contractile power participates in maintaining a relatively flat lamellum (compared to the cell bulk), by bending dorsal SFs downward, forcing them to pivot around the focal adhesions.

Regulation of SF assembly and contractility

Stress fibers are not normally observed in intact tissues, but rather cells develop them in specific situations, in response to high mechanical forces, such as during the contraction of wounds and scar tissue, or in endothelial cells lining vessels in hypertensive animals. In cultured environments, stress fibers are prominent on 2d surfaces and in rigid 3d matrices, when cells generate elevated levels of isometric tension [Burridge and Wittchen, 2013]. This indicates that SF assembly is indirectly regulated by mechanical tension. This is partly done through the action of the small signaling proteins RhoA, Rac1 and Cdc42, all members of the Rho GTPases family. RhoA promotes SF assembly through the formin mDia (nucleator and polymerizing factor of dorsal SF), and a Rho-associated protein kinase, ROCK. Among other targets, ROCK promotes the phosphorylation of the myosin regulatory light chain, thereby increasing stress fiber contractility. It also inhibits cofilin-mediated actin disassembly, thus stabilizing long actin filaments. Rac1 and Cdc42 promote respectively Arp2/3- and formin-based nucleation of actin filaments, which then serve as building blocks of SF, as shown in Figure 1.11 [Tojkander et al., 2012]. However, since Rac and Cdc42 also promote the formation of protrusions (lamellipodia and filopodia), they are often viewed as antagonistic to Rho, tipping the balance in favor of migration, while Rho favors contractility. The activation of Rac and Rho at focal adhesions can lead to gradients of GTPases and their effectors, depending on the distribution of adhesions [Bershadsky et al., 2003].

1.3 Traction forces

1.3.1 Cellular generation of traction forces

During spreading and migration, cells pull on the substrate, exerting so-called traction forces. The forces are transduced to the substrate via the adhesion complexes described in section 1.2.3. These forces originate from the friction of cytoskeletal filaments at adhesions, and from the activity of myosin motors in bundles of actin filaments. In motile cells, friction at adhesions is created by the retrograde flow of actin filaments from the lamellipodium to the lamellum region. Waterman and colleagues found a biphasic relation between actin retrograde flow and traction stresses, such that traction stresses first increase as flow velocity decreases, indicating the engagement and strengthening of the molecular clutch proteins; then when the clutch engagement is maximal, flow velocity further decreases together with traction stress magnitude, and the clutch becomes eventually disengaged (Figure 1.12).

For some time, it was thought that the maturation of focal adhesions under force was due to the tension exerted by dorsal fibers only. However, recent experiments conducted by Gardel and colleagues [Oakes et al., 2012] demonstrated that maturation of focal adhesions and transmission of traction forces are independent of the presence of dorsal SF. In fact, the presence of dorsal SF even tends to diminish the magnitude of the traction forces. The transverse arcs are those responsible for the buildup of traction forces and the maturation of focal adhesions. This led to the hypothesis that dorsal SF serve as a template to stabilize the cytoskeleton-adhesion system, allowing for long-term establishment of focal adhesions and subsequent evolution to fibrillar adhesions. Fibrillar adhesions are the sites used for ECM remodeling, an important properties of cells of the connective tissue. As a natural consequence, one will find less dorsal SFs in fast migrating cells, where adhesion turnover is high, and more in slow migrating cells and non-motile cells which specialize in ECM production or remodeling. Transverse arcs are not the only source of traction forces in adherent cells, for on patterns with non-adhesive edges, it has been observed that peripheral stress fibers also exert a significant amount of stress [Albert and Schwarz, 2014, Mandal et al., 2014].

1.3.2 Measuring traction forces and cell mechanical tension

The first attempts to measure cell-generated traction forces were conducted by [Harris et al., 1980] who observed wrinkles on silicone-rubber substrates. Since then, many different techniques have been developed (reviewed in Kraning-Rush et al. 2012), such as **traction force microscopy** on soft gels [Lee et al., 1994, Pelham and Wang, 1999, Dembo and Wang, 1999] or tracking the deformation of **elastic micro-pillars** [Tan et al., 2003, Balaban et al., 2001, Ghibaudo et al., 2008]. Traction force microscopy (TFM) consists of embedding micron-sized beads in a soft gel, typically polyacrylamide (PAA), and to record the displacements of the beads under cell forces (there is a more detailed description in 2.3.2 and 2.5.2). The improvements brought over the years to this technique and to analytical tools now allow to reach micron resolution in the stress field reconstruction [Sabass et al., 2008]. Micro-pillar based experiments use PDMS or PMMA elastic pillars and reconstruct forces based on the displacements of pillars, assuming each pillar deforms elastically. It is a discrete rather than continuous method and gives directly the force vector field, instead of the stress field as in the case of TFM. Cell spreading is weakly constrained on the pillars since the location of adhesions is restricted to the pillar array. TFM can also be performed while constraining cell spreading by using patterned PAA gels. This has been extensively done in the present work to study the influence of substrate geometry and cell shape on traction forces.

The type of substrate used for traction force microscopy measurement should be carefully chosen, since there are known influences of the extracellular environment on levels of mechanical tension within cells. In particular, cells adapt their tension to the stiffness of the substrate, but inversely also have a preferential stiffness, a concept termed “tensional homeostasis” [Brown et al., 1998, Engler et al., 2006, Reinhart-King et al., 2005, Webster et al., 2014]. It is therefore necessary to tune the gel stiffness to the cell type. TFM is well suited for this since our protocol allows us to fabricate gels with stiffness ranging from 1 to 40kPa. For the study of fibroblasts, PAA gels of 8kPa to 20kPa were prepared (detailed in section 2.2.2).

While TFM and similar techniques are used to measure cellular traction forces exerted on the substrate, other techniques allow to measure the mechanical tension in non-adherent cellular structures. For instance, micro-plates coated with adhesive protein or Atomic Microscopy (AFM) have been used to measure cell stiffness [Fouchard et al., 2014]. Tension within single fibers can be measured using micro-needles or cantilevers [Bernal et al., 2007]. In both these methods, a known deformation is applied to cells and the response force is measured by the deflection of a plate or of a cantilever beam. Examples are given in Figure 1.13.

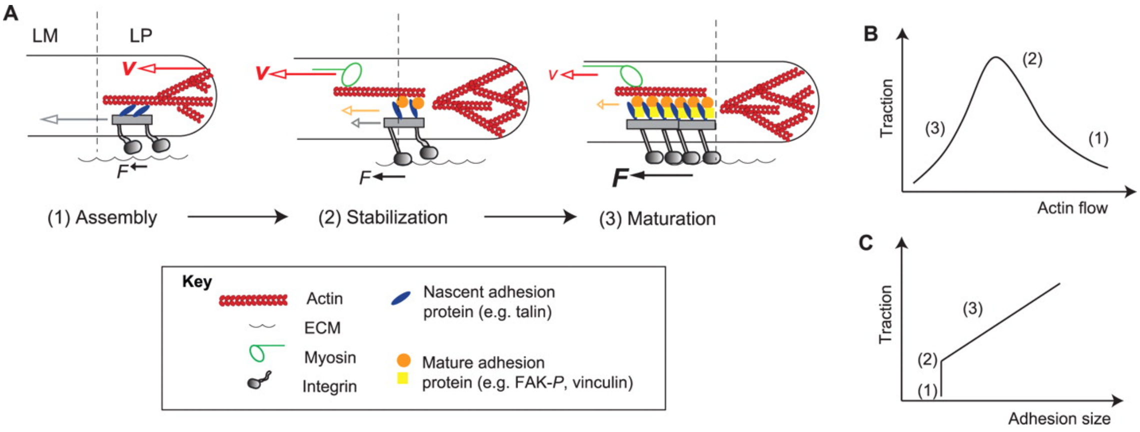
A
LM
LP
V
F
(1) Assembly
(2) Stabilization
(3) Maturation
Key
Actin
ECM
Myosin
Integrin
Nascent adhesion protein (e.g. talin)
Mature adhesion protein (e.g. FAK-P, vinculin)
B
Traction
(3)
(2)
(1)
Actin flow
C
Traction
(3)
(2)
(1)
Adhesion size

Figure 1.12: Correlations between actin retrograde flow, adhesion size and traction forces during adhesion assembly. (A) As nascent adhesions form, the engagement between adhesion clutch molecules and actin filaments is weak, leading to a fast retrograde flow (red arrow) and low traction forces (black arrow)(1). Adhesion stabilization and myosin-powered flow strengthen the clutch, reduce flow velocity and increase traction forces (2). Stress fibers anchor at the protein plaque of mature adhesions, adhesions elongate, forces increase (3). (B) Biphasic correlation of retrograde flow speed and traction force, starting from an inverse correlation to a direct one. (C) Adhesion size and traction force correlate in stable and mature adhesions, not in nascent ones. Reproduced from [Schwarz and Gardel, 2012].

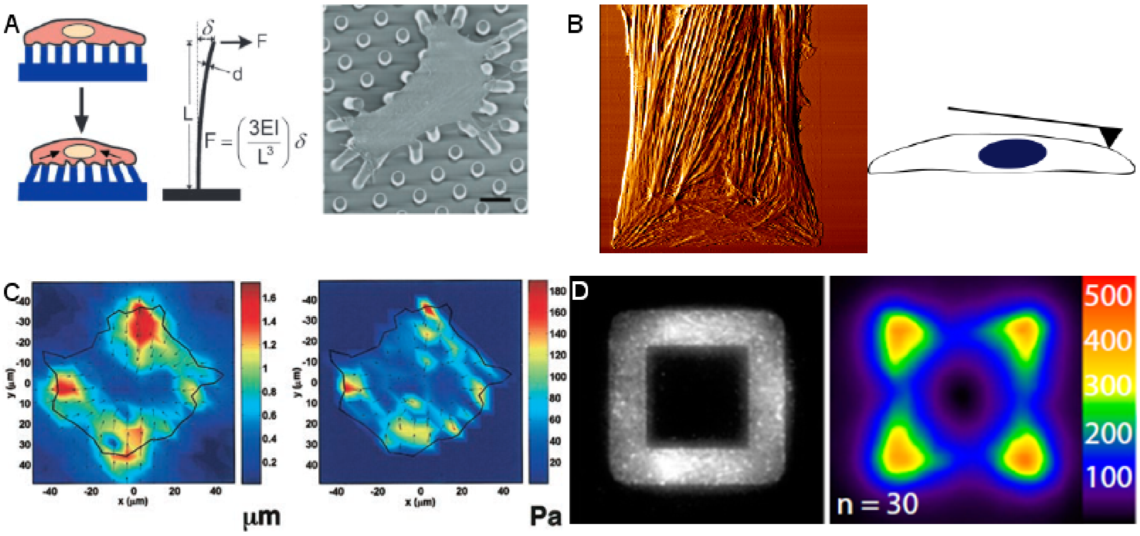
A
δ
F
d
L
F = (3EI / L³) δ
B
C
y (μm)
x (μm)
1.6
1.4
1.2
1
0.8
0.6
0.4
0.2
μm
180
160
140
120
100
80
60
40
20
Pa
D
500
400
300
200
100
n = 30

Figure 1.13: Examples of force measurement techniques. A) Elastic Micro-post deflect proportionally to the applied force [Tan et al., 2003]. B) AFM tip measures fibroblast stiffness by scanning the mechanical force needed to indent the cell. Stress fibers are prominently visible. C) Displacement (left) and traction stress (right) vectors of a cell spread on a soft gel. Forces were measured with TFM [Parker et al., 2002] D) TFM on a patterned substrate (pattern geometry shown on the left). The forces concentrate on the adhesive parts and are higher at the corner of the patterns [Tseng et al., 2012].

1.4 Influence of ECM properties on cell function

We have outlined above the main steps involved in cell spreading and traction force generation, and emphasized that cell-matrix adhesions are central to these processes. The reason for this are that adhesions are able to sense the mechanical properties of the extracellular matrix. It is now well established that cells feel and respond to the geometry (i.e. size and shape of adhesive islands) and the stiffness (or rigidity) of the ECM [Discher et al., 2005, Tee et al., 2011], the most striking examples being brought by the cell-shape dependent switch from growth to apoptosis in endothelial cells [Chen et al., 1997] and the stiffness-specific lineage commitment in undifferentiated mesenchymal stem cells, such that neuron progenitors are found on soft matrices and bone progenitors on stiff matrices [Engler et al., 2006]. In differentiated cells such as fibroblasts, ECM stiffness also influences cell spreading and cell tension generation [Schwarz et al., 2006, Marcq et al., 2011, Zemel et al., 2010b]. However, it remains difficult to unravel the downstream effects on cell area, cell traction forces or cell polarization given how entangled these properties are. We here review some experimental and theoretical aspects of how the properties of the extracellular matrix influence cell behavior.

1.4.1 Effet of the matrix' rigidity

One of the most obvious effects of changing ECM rigidity is that cells increase their spread area with substrate stiffness until they reach a plateau value. This has been observed both on homogeneous substrates [Yeung et al., 2005, Zemel et al., 2010a] and on micro-pillars [Ghibaudo et al., 2008, Han et al., 2012]. Cell polarization increases as well with substrate stiffness, until an optimal point, so that cells are more elongated on substrates whose stiffness best matches their intracellular stiffness. This is also observed at the subcellular level, since focal adhesions become more elongated on stiffer substrates (higher aspect ratios), though their average area is only marginally higher [Prager-Khoutorsky et al., 2011, Yip et al., 2013, Han et al., 2012].

These observed changes in cell morphology are a consequence of the mechanical balance between the cell and the substrate. There is indeed a simultaneous monotonical increase of traction stresses on increasing substrate stiffness, up to a saturating stress level [Ghibaudo et al., 2008, Han et al., 2012, Yip et al., 2013, Oakes et al., 2014]. This has been explained in the framework of active matter theory by representing the ECM as a linear spring, and the cell as the combination of an elastic stress and motor activity. The interplay of motor contractility and elasticity produces a sigmoidal increase of tension with substrate

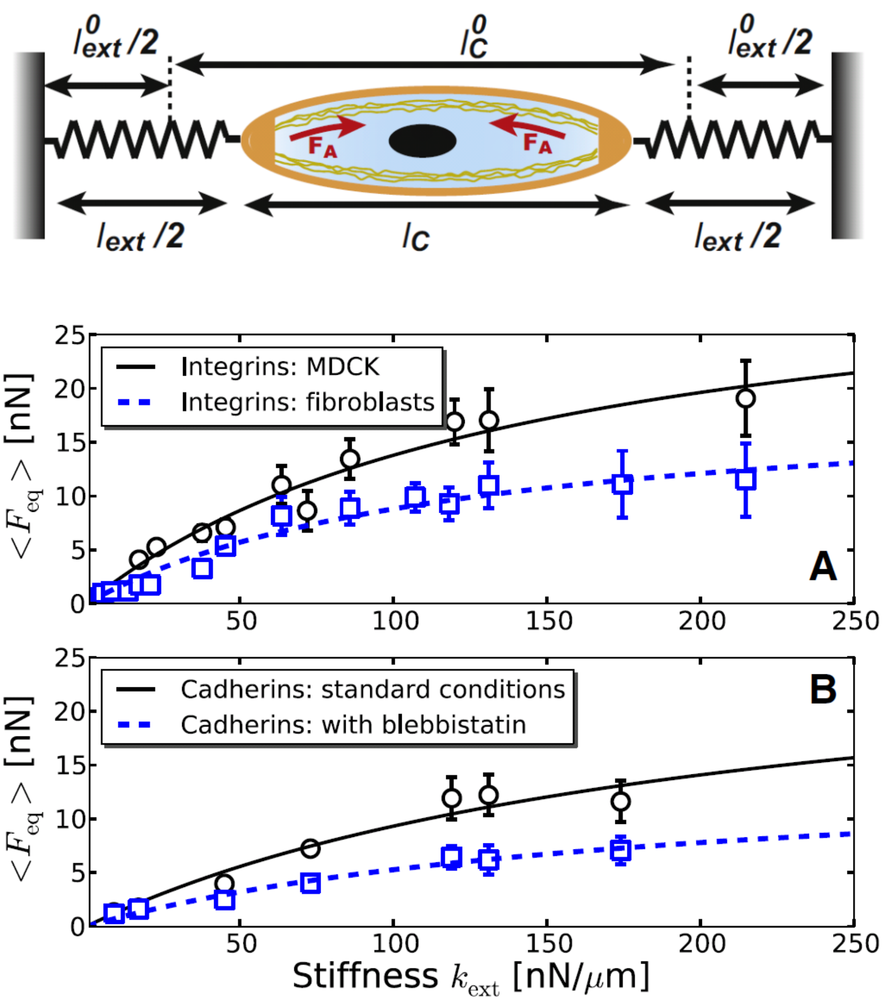

Figure 1.14: Active matter model for rigidity sensing. Model predictions and fit with experiment showing the increase of the equilibrium traction force with ECM stiffness k_{ext}. Data points are from Ghibaudo et al. [2008], solid lines are results from the model in Marcq et al. [2011]. Reproduced from Marcq et al. [2011].

stiffness [Marcq et al., 2011 and Figure 1.14]. Other two-spring or three-spring models have predicted the increase and saturation of cellular stress with substrate stiffness, taking into account the dynamics of adhesive complexes or the cell polarization on top of matrix rigidity [Schwarz et al., 2006, Zemel et al., 2010b].

1.4.2 Effect of the matrix' adhesive geometry

The results mentioned above show that cells adapt their mechanical tension to the stiffness of the extracellular environment. This is known as tensional homeostasis. The tensional setpoint is not only determined by substrate stiffness. For instance, cells restricted to small spreading areas do not respond to changes in stiffness as larger cells normally do [Tee et al., 2011]. Recently, Fletcher and co-workers have shown that single cells resort to tensional buffering, being able to tune their setpoint in a strain-rate dependent manner, in response to external forces [Webster et al., 2014]. Cells therefore dynamically adapt their tensional setpoint to external mechanical perturbations. Cell spread area also increases intracellular tension, independently of substrate stiffness. Whether this is mimicked in focal adhesion size and distribution is unclear. One could expect that larger FAs would lead to higher stresses, given the known fact that FA elongate under tension [Balaban et al., 2001]. The development of high-resolution traction force microscopy techniques have enabled to test that idea thoroughly. Gardel and colleagues found that the relationship of FA size with traction stresses is spatiotemporally regulated, with FA size increasing linearly with traction stress in the early stages of FA growth, and near the cell edge. But once FA size saturate at a maximal size, traction stresses then either continue increasing near the cell, or decrease if the FA is far from the cell edge (see Figure 1.12 and [Stricker et al., 2011]). FA size may thus not be in proportion to traction stress levels [Oakes and Gardel, 2014]. Several studies have also shown that the increase of traction stresses with cell area is not due to a greater number of focal adhesions [Han et al., 2012, Oakes et al., 2014], and is thus not directly controlled by adhesive area. Both Rape et al. [2011] and Oakes et al. [2014] report higher maximal stresses with increasing cell radius, for a constant adhesive area. Therefore the center-to-corner distance is the factor determining traction stress levels in cells. Oakes et al. [2014] further verified that the local curvature of the micropatterned island influences the maximal stress exerted at FAs, but not their local density. They conclude that FA density and maximal stress are modulated by cell area and cell shape, so as to maintain a constant strain energy (defined here by the product of substrate displacement by traction stress).

From the studies cited above, it appears that cells have a given strain energy for a given area. The shape of the adhesive pattern and the stiffness of the substrate will only modify how and where this energy is spent (high substrate strain or maximal stress at places of high curvature). The distribution of tension in the cell can thus be controlled as was done in those studies by imposing specific adhesive geometries through micropatterning techniques. Mandal et al. [2014] even showed that specific adhesive geometries for the same external cell envelope is sufficient to redirect both the orientation of actin fibers and the direction of principal stress. Adhesive geometry therefore elicits a global cell response, and is able to control cell polarization, even in non-motile cells. This can be useful to control downstream behavior such as the local organization of the cytoskeleton, but also directed cell migration, or the orientation of cell division [Théry et al., 2006b, Reymann et al., 2010; 2012, Vignaud et al., 2012].

1.5 Mechanical coupling of cell shape and cell tension

To further explore how cell morphology can impact the cell's tensional state, we briefly discuss a few models explaining how the minimization of energy relate cell shape and cell traction stresses. Most models compare numerical results based on energy minimization to the experimental shapes and/or traction forces of cells on patterned substrates, in which cell size and shape is constrained by the adhesive geometry. Using discrete adhesive patterns (i.e. non-homogeneous) allows for the presence of free edges usually defined by prominent stress fibers.

The cell is assimilated to a thin 2-dimensional sheet of material. The cell interior is either represented as a homogeneous contractile bulk [Bischofs et al., 2009, Banerjee and Giomi, 2013], or as a meshwork of small filaments [Guthardt Torres et al., 2012, Lemmon and Romer, 2010]. There are generally 3 main contributions to the system's energy: contour energy (driving the straightening of the contour), contractile pressure proportional to cell area (driving the area minimization) and the local adhesive energy. Cell sorting and cell spreading on dotted adhesive patterns have been successfully simulated based on such energy minimization and Monte-Carlo routines. This is known as the Cellular Potts Model [Graner and Glazier, 1992, Vianay et al., 2010]. Similar approaches have then be used to predict the magnitude of traction forces for cells of given geometries, with some variations in the energy functional used. For instance, Banerjee and Giomi [2013] introduced explicit center-to-edge dependence in the adhesive energy at FAs, and some bending energy in the contour term, corresponding to the bending of the bundle delineating the contour. This is useful to explain convex contours or cusps, but is neglected in the other models. Oakes et al. [2014] have compared results of a model that does not take line tension into account with one that does, and found that including line tension in the energy functional results in traction stresses concentrated at regions of high curvature, as observed experimentally (Figure 1.15). Albert and Schwarz [2014] add an elastic contour term in the line tension for the free edges. They are able to robustly predict both traction stresses and edge curvature during spreading using this modified Potts model.

The concave shape of the free edges is one geometrical demonstration of the mechanical balance in the cell. Their radius is given by the ratio of the local contour energy and the bulk contractile energy. This is a 2-dimensional analog to the Laplace law describing the shape of droplets as a function of pressure and interfacial tension $\Delta P = \gamma(1/R_1 + 1/R_2)$; in the case of a 2-dimensional description of cell shape, the out-of-plane radius R_2 is taken to be very large such that the second term can be neglected. This description has been detailed in Bischofs et al. [2008; 2009] and used to analyze the steady-state shape of free

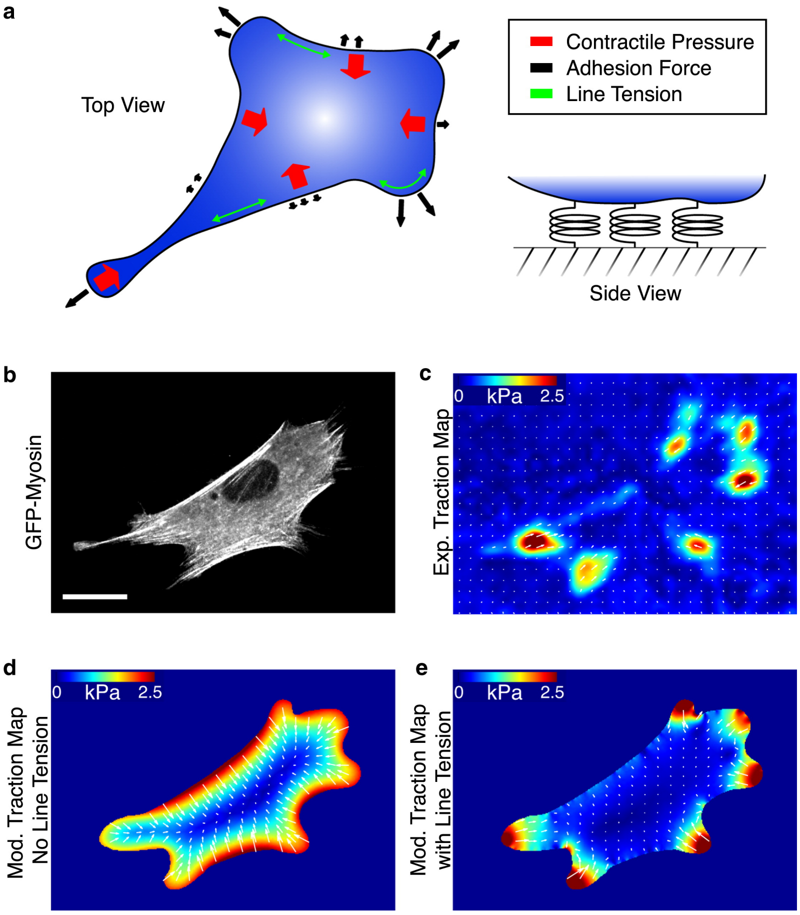
a
Top View
Contractile Pressure
Adhesion Force
Line Tension
Side View
b
GFP-Myosin
c
Exp. Traction Map
0 kPa 2.5
d
Mod. Traction Map
No Line Tension
0 kPa 2.5
e
Mod. Traction Map
with Line Tension
0 kPa 2.5

Figure 1.15: Contractile gel model with uniform boundary tension predicts traction stress localization. (a) Illustration of the terms entering the energy functional. (b) Fluorescent myosin of a cell spread on a gel and (c) corresponding traction stress magnitude map. Output of the model for this cell geometry without including the line tension term (d) or with the line tension term (e). Reproduced from Oakes et al. [2014].

contour lengths. This relation and how it may explain shape dynamics will be extensively discussed in Chapters 3 and 4.

1.6 Viscoelastic models of the cell and the cytoskeleton

As the models just described show, the mechanical properties of cells are usually discussed in terms of energy or forces, rather than in biological terms. Similarly, the response of single molecules or ensemble of molecules can be modeled in terms of elastic or viscous elements. Combinations of viscoelastic units can also be used to model cell behavior as a whole. We give here briefly some examples of how contractile bundles have been modeled in other works.

Linear solids

At low strains, biological fibers behave as linear materials, that is that the stress is proportional to strain and follows Hooke's law $\sigma = E\epsilon$. To model the mechanical response of cytoskeletal bundles, the behavior of both filaments and motors need to be considered. Additionally, the coupling with adhesions to which bundles are connected can be relevant. Filaments are represented by arrangements of springs (force proportional to the deformation, $F = kx$) and dashpots (force proportional to deformation rate $F = \eta\dot{x}$). Motors are modeled by a contractile element, whose force T_0 is constant, or function of deformation rate: $T = T_0 f(\dot{x})$. These elements can be arranged in series (the respective forces are in balance, the deformations of each element add up), or in parallel (the elements have the same displacement, and their forces add up). As an example, the response of a Maxwell fluid model, a Kelvin-Voigt solid model and a Standard-Linear solid model, which are the three most used elementary models (without motors), are shown in Figure 1.16. The deformation of a spring is instantaneous (as can be seen by the vertical lines in the Maxwell and Standard-Linear models), whereas a dashpot is slow to deform, taking a characteristic time $\tau = \eta/k$ (the stiffer the spring, the faster the deformation).

Colombelli et al. [2009] and Besser et al. [2011] have studied the relaxation dynamics and force propagation in stress fibers severed by laser ablation. They found that fiber retraction is restricted close to the cut, and that the release of tension as the fiber is severed recruits zyxin, a focal adhesion protein. They used a viscoelastic-contractile bundle model to explain their findings (Figure 1.17). This model succeeds in explaining that SF contract non-uniformally along their length, and that they are elastically coupled to the substrate. They additionally predict that when such elastic coupling dominates over friction coupling, oscillations in the displacements of bands along the fiber appear, a fact later confirmed by experiments. In another study by the same authors [Besser and Schwarz, 2007], non-uniform contractility of SF was explained with a similar viscoelastic-contractile model, but without explicit mechanical coupling to the environment. Instead, a biochemical

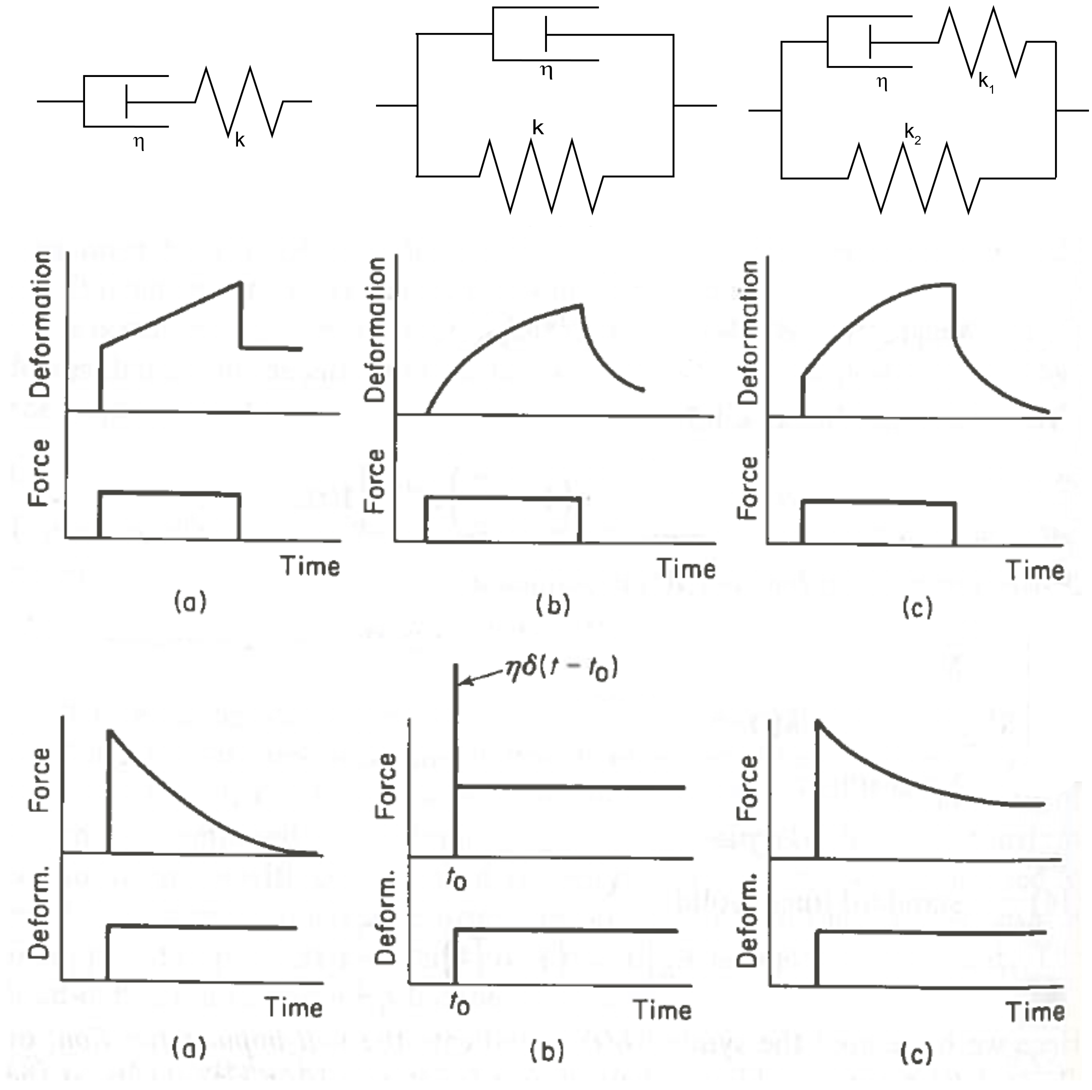

Maxwell Kelvin-Voigt Standar-Linear

Figure 1.16: Response of elementary viscoelastic models to a step force and a step deformation. (a) Maxwell model, (b) Kelvin-Voigt model, (c) Standard-Linear model. Reproduced from [Fung, 1965].

positive feedback loop at adhesion sites (increased ROCK activity under tension) led to the contraction of the peripheral bands and the elongation of the central bands, as had been also observed experimentally in Peterson et al. [2004]. These mechanical models therefore contribute to the proper interpretation of experimental results and to get further insight into the crosstalk between mechanical elements and biochemical signaling. In Chapter 5, we use a similar model to analyze the mechanical response of transverse deformed isolated fibers. However, since the initial observed response was elastic followed by a viscoelastic relaxation, we use a 3-parameter-solid model (spring k_1 in series with {spring k_2// dashpot η}) which better accounts for this behavior. The responses of such a model to a step force and a step deformation are shown in Figure 1.18.

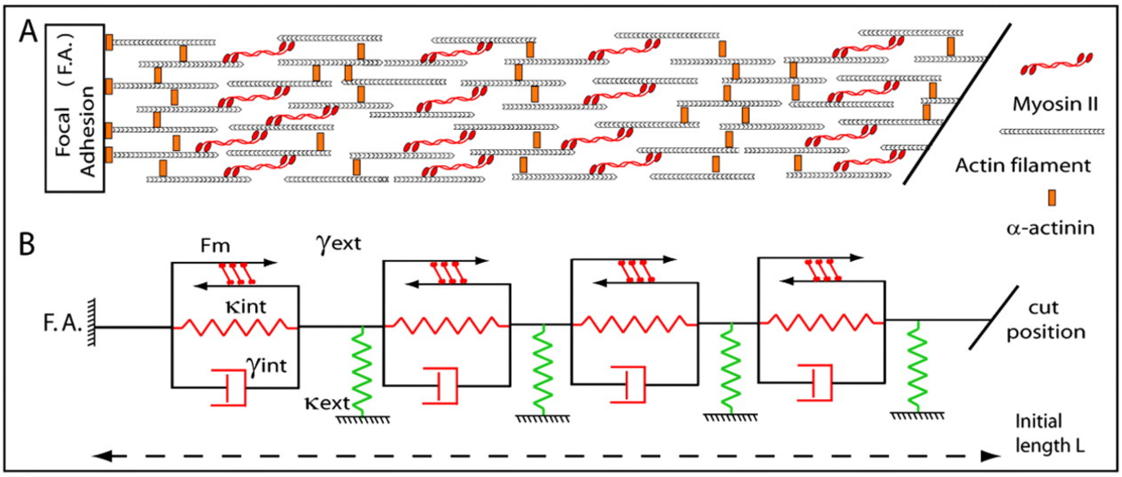
A
Focal Adhesion
(F.A.)
Myosin II
Actin filament
α-actinin
B
Fm
γext
κint
γint
κext
F. A.
cut position
Initial length L

Figure 1.17: Viscoelastic model of a contractile SF coupled to the susbtrate. The SF is represented as a seires of similar units. Each unit being the parallel association of a motor contractile part of force F_m, a spring k_{int} and a dashpot γ_{int}. The fiber is elastically coupled to the substrate by spring k_{ext}. One end of the fiber is fixed at the focal adhesion (FA), while the other end is free (cut position). Reproduced from Colombelli et al. [2009].

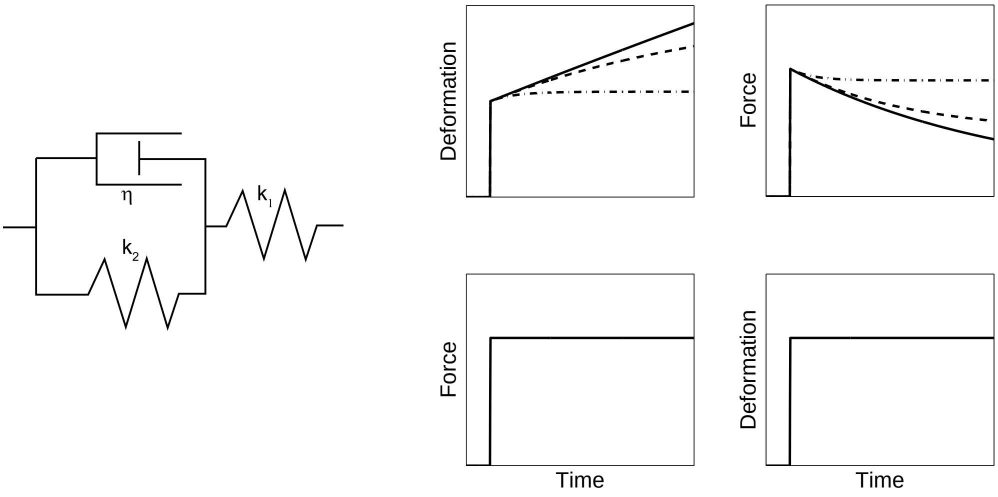

Figure 1.18: Response of a 3-parameter-solid model to a step force and a step deformation for several couple of parameters. Solid line: $k_1 = 10k_2$, dashed line: $k_1 = k_2$ and dash-dot line: $k_1 = 0.1k_2$.

Non-linear elastic behavior

Some structures, and notably reconstituted actin networks, display strain-hardening or strain-softening properties, that is that the cell stiffness increases or decreases with strain [Chaudhuri et al., 2007, Xu et al., 2000]. Strain-hardening mechanisms thus contribute to the reinforcement of the cytoskeleton under high loads. This can result either from the mechanical properties of cross-linkers or from those of the polymer filaments themselves, and is dependent on the architecture of the network under consideration (filament length, nature of the crosslinkers). Nonetheless, the quantification of these phenomena is out of the scope of this work.

1.7 Research aims in context

We have briefly given examples of how adhesive geometry and constrained cell shape could change the local magnitude of traction stresses. However, most of the studies mentioned have been conducted on uniformly adhesive substrates or cell-sized islands. The adhesion layout was therefore continuous. We propose to examine which mechanisms govern cytoskeleton assembly and cytoskeletal tension on non-uniform adhesive patterns, and how the peripheral stress fibers thus formed contribute to traction forces at the cell-substrate interface. Deciphering the interplay between substrate geometry, cell morphology and cell mechanical tension is essential for the further understanding of mechanical signaling pathways and the biochemical feedback loops associated to them.

Chapter 2

Materials and Methods

2.1 Biology

2.1.1 Cell Culture

All experiments were done on fibroblasts. In Chapter 3, we used both NIH 3T3 (a mouse cell line) and subcutaneous fibroblasts (SCF, primary cells from rats). SCF were used up to passage P6. In Chapters 4 and 5, we used rat embryonic fibroblasts (REF52, a rat cell line). All cell types were cultured in Dulbecco's Modified Eagle Medium (DMEM) supplemented with 1% L-glutamine, 1% of antibiotic mix penicillin-streptomycin, and 10% Fetal Calf Serum. For live experiments, imaging medium Leibovitz-15 (L-15) was used (buffered so that the pH$\sim$7.4 was stable for several hours). For all experiments, cells were usually seeded in 12-wells plates two or three days prior to experiments so that they were close to confluence before the experiments. Cells were then detached with 0.02% EDTA in Phosphate Buffer Saline (PBS) and 0.25% trypsin, and seeded on the substrates for the experiments, thus having a reproducible number of cells on each sample.

2.1.2 Experimental protocols

Transfections

For actin dynamics experiments and traction force microscopy, cells were transfected with LifeAct EGFP (plasmid purchased from IBIDI), two days prior to experiments, in antibiotic-free medium. The LifeAct-EGFP peptide binds to F-actin without interfering with cytoskeletal dynamics and enables live fluorescent visualization of the filaments. We used Fugene HD (Promega) as a transfection vector since it is the one which gave the best success rates. After testing different ratios, we found that using 4.5µL:1µg as ratio of Fugene:plasmid gave the highest percentage of transfected cells. We attempted transfections with plasmids encoding myosin heavy chain or focal adhesion proteins paxillin/vinculin, but the transfection success rates on the fibroblasts were too low to have a sufficient number of cells with stable fluorescent signal throughout the experiments.

Fixation protocols

Two different fixation protocols were used, a standard one and one combined with cytoskeleton extraction. The fixating agent was paraformaldehyde (PFA) in both protocols, prepared in PBS. Cytoskeleton extraction was used to remove cytoplasmic content, reducing background, and giving a higher contrast for the cytoskeleton and associated proteins (actin, myosin). However, to visualize focal adhesions, the standard fixation protocol yielded better results.

Standard protocol	Protocol with cytoskeleton extraction
Wash with serum free medium (1x)	Wash with serum free medium (1x)
Fixation with 4% PFA, 10 min	Fixation with 4% PFA in CSK buffer 4°C, 15 min
	Permeabilization with 0.2% Triton X-100 in CSK buffer, at 4°C, 10 min
Rinse with PBS (3x)	Rinse with PBS (3x)

Cytoskeleton buffer composition (reagents diluted in distilled H_2O, pH=6.9)

60mM PIPES
2mM MgCl2
1mM Na-Orthovanadate
25mM HEPES
1mM PMSF (added just before use)

Immunostaining protocols

Standard immunostaining protocols were used following standard fixation or fixation + extraction [Smith et al., 2010]. Cells were permeabilized with 0.2% Triton X-100 before staining. Primary antibodies were incubated for 1 hour, then rinsed 3x with PBS, secondary antibodies were incubated for 1 hour, then rinsed 3x with PBS. The primary antibodies used to mark focal adhesions were anti-paxillin and anti-vinculin. Myosin was labeled with either isoform-specific antibodies (anti-MYH9 for IIa, anti-myosin IIb for IIb), or with anti-MLC which targets the phosphorylated form of the light chain. Other primary antibodies used include anti-α-actinin. F-actin was labeled with Alexa-Phalloidin directly conjugated to a fluorophore. DAPI was used to label the nuclei of fixed cells.

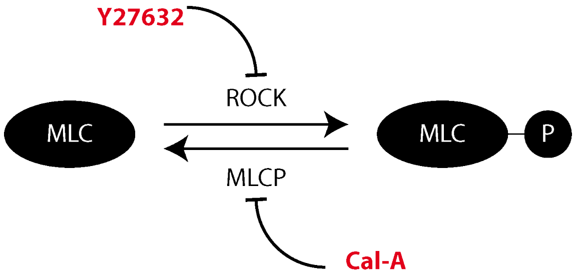

Figure 2.1: Schematic of the myosin phosphorylation reaction, enhanced by ROCK and inhibited by MLCP. This sketch is voluntarily over-simplified to illustrate the action of Y27632 and Calyculin A. Myosin activity is in fact regulated by the coordinated action of many different enzymes. Details can be found in Vicente-Manzanares et al. [2009b].

2.1.3 Chemical compounds to alter myosin activity

Myosin was inhibited using either ROCK inhibitor 10µM Y27632, or 50µM blebbistatin. Myosin light chain phosphatase was inhibited using 5nM calyculin A. Y27632 and calyculin both act on the phosphorylation of the myosin light chain. Y27632 inhibits the ROCK-mediated phosphorylation by binding to ROCK and acting as a competitive inhibitor to ATP, while calyculin A inhibits the action of myosin light chain phosphatase (MLCP) (Figure 2.1). On the other hand, blebbistatin acts directly on the myosin, blocking the myosin heads in a low actin-affinity conformation [Straight et al., 2003, Sakamoto et al., 2005]. All drugs were freshly diluted in the imaging medium, to reach the desired final concentration. Y27632 and blebbistatin are light sensitive and were therefore used in the dark. Additionally, blebbistatin is inactivated by UV light. Therefore no imaging with close to UV wavelengths was possible (in particular GFP imaging of transfected cells) during blebbistatin treatment.

2.2 Microfabrication of patterned substrates

Micropatterning tools have become standard to cell biology experiments over the last decade. A great variety of protocols exist depending on the dimension of the substrates (2d or 3d), the nature of the surface to pattern (glass, hydrogel matrix or 2d soft gels) and the critical size to reach (micron or sub-micron). Micropatterning can also be combined with microfluidics to allow for cell migration under controlled flow conditions. All these tools have been employed to study the effects of constrained geometry on cell function. Though micropatterned substrates may seem artificial, they are in fact a very convenient way to reproduce and study in a systematic way specific features of cellular micro-environments, that are all but homogeneous. Thus the layout of adhesive protein, the size of an adhesive island and its local curvature, the local stiffness, the height of a channel, are all features that can be finely controlled and used to constrain cell morphology and function, and the expression of certain cytoskeletal features. We have thus extensively resorted to some micropatterning tools for 2-dimensional susbtrates in this work. Descriptions of other micropatterning techniques are given in [Théry, 2010, Piel and Théry, 2014].

All experiments were done on patterned substrates, though occasionally control experiments were done on homogeneous adhesive substrates. The adhesive patterning on glass and gels is based on the same UV-lithography techniques detailed below. The adhesive layer was systematically prepared with human plasma fibronectin diluted at 10 or 20µg/mL in PBS. Fibrinogen conjugated to Alexa-Fluor was added to the fibronectin solution at 15µg/mL to mark the pattern fluorescently. The protein was adsorbed on the surface for 90 min in an atmosphere-controlled incubator (T=37°C).

2.2.1 Photolithography on glass substrates

Patterned glass coverslips were fabricated using standard UV-photolithography techniques [Guillou et al., 2008]. The steps are detailed in Table 2.1. For experiments done on glass substrates, the coverslips were functionalized with OctaDecylTrichloroSilane (ODTS) for stronger attachment of the adhesive protein. This prevented the cells from ripping off the protein and ensured the stability of the adhesive pattern during the time of the experiment. For experiments done on gels, the patterned glass coverslips were only used to transfer the pattern to the gels, so weak attachment of the protein to the glass was preferable. Therefore, no surface functionalization with ODTS was necessary.

2.2.2 Polyacrylamide gel fabrication

Traction force microscopy on polyacrylamide gels (PAA) is a well-established experimental method to investigate forces exerted by cells on substrates of varying rigidities. An increasing number of studies now resort to patterned gels, to constrain the localization of adhesions and thus of traction forces. Several protocols exist to create an adhesive pattern on the gel surface, such as micro-contact printing, or direct PAA activation by UV light [Tseng et al., 2011]. We used an alternative technique, taking advantage of existing setup for the easy patterning of glass coverslips by photolithography. We thus followed standard protocols for gel fabrication [Tse and Engler, 2010], and used those patterned glass coverslips to transer the pattern to the gel, as shown in Table 2.2. PAA solution was prepared with acrylamide and bis-acrylamide in different concentrations to obtain different gel rigidities. The gel rigidities used here were typically between 8.7 kPa (5% w/v acrylamide and 0.3% w/v bis-acrylamide) and 16.7 kPa (10% w/v acrylamide for 0.15% w/v bis-acrylamide). A table of concentrations and rigidities can be found in Tse and Engler [2010]. To obtain patterned gels, a support glass coverslip was treated sequentially with 0.1 M NaOH, (3-Aminopropyl)-TriMethoxySilane (APTMS) and 0.5% glutaraldehyde to permit strong gel attachment to the coverslip. Gels were then polymerized in two layers, the top one containing red fluorescent beads (diameter 200 nm). Polymerization was triggered by adding TEMED and 0.05% ammonium persulfate (APS) to the PAA solution. The bottom layer was polymerized between the glutaraldehyde treated support coverslip and a surfasil-treated top coverslip. Surfasil, diluted in choloroform ensured easy lift-off of the top layer. The top layer was polymerized between the bottom layer and a patterned glass coverslip with adhesive protein adsorbed on it. There was no need for anti-adhesive backfilling of the surface of the gel with pluronic, since the gel was in itself anti-adhesive. To transfer the protein from the patterned coverslip to the gel, a crosslinker sulfo-SANPAH was added to the gel solution, and it was allowed to polymerize for 30 minutes.

The gels were prepared using round coverslips, but were then cut to a rectangular strip with a scalpel so that a microchannel (sticky-slide from IBIDI) could be glued onto it. This microchannel facilitated medium changes with small volumes during the experiment.

2.2.3 3-dimensional PDMS pattern fabrication

3-dimensional patterns were fabricated with polydimethylsiloxane (PDMS), a biocompatible silicone elastomer. Molds for PDMS patterns were etched into silicon wafers at $\sim 5\mu m$ depth. Si wafers were fabricated by photolithography followed by dry etching, using standard protocols [Ghibaudo et al., 2008]. PDMS was prepared at a ratio of 10:1 of base:curing agent, spin coated on a support coverslip (primed with 1M NaOH) and molded with a Si mask on which surfasil had been evaporated. Curing time of 40 min at 100° C was sufficient to have proper polymerization and allow easy mold lift off.

PDMS patterning was done by microcontact printing, using a glass coverslip on which adhesive protein was uniformly adsorbed. The PDMS patterns were palced under UV light (16 W, at 3cm) for 30 min to improve stamping quality. They were then were stamped with the adhesive protein for $\sim$ 1 minute. Finally, PDMS samples were immersed in 2% Pluronic so that only the top of the structures were adhesive. See Table 2.3 for illustrations.

1. Chrome mask fabrication Laser writing + wet etching of the exposed chrome layer Reusable, stored in clean room	
2. Surface functionalization ODTS, diluted 1/1000 (v/v) in Hexane, deposited on a glass surface primed with a 0_2 plasma 100 W, 1min. Can be kept several weeks in closed environment	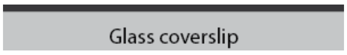 Glass coverslip
3. Coating with photo-resist Photoresist (PR) spin-coated at 5500 rpm for a resulting 0.5µm thickness Coating followed immediately by exposure	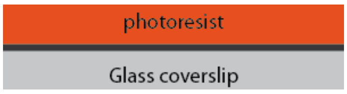 photoresist Glass coverslip
4. UV insolation + development PR exposed with a mask aligner (15 mW/cm^2, 7 sec.) Exposed PR developed in a bath of CD26 for 10 sec Micropatterns stored in dark for several weeks	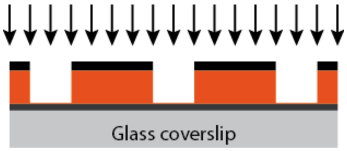 Glass coverslip
5. Protein adsorption 10µg/mL fibronectin + 15µg/mL fibrinogen conjugated to Alexa647 incubated on the pattern at 37°C for 90min Done 1 day before experiment	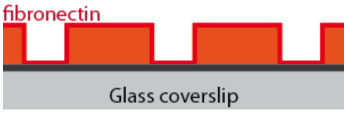 fibronectin Glass coverslip
6. PR stripping Photoresist removed by a 5 sec dip in ethanol placed in ultrasonic bath This steps immediately follows protein adsorption	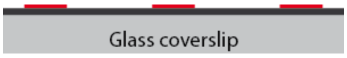 Glass coverslip
7. Surface backfilling Pluronic 2% in H_2O incubated at room temperature for 2hrs This step immediately followed PR stripping	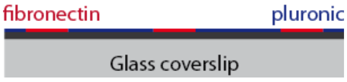 fibronectin pluronic Glass coverslip
in fine constrained cell spreading Cell-substrate adhesion complexes are restricted to the patterned adhesive areas	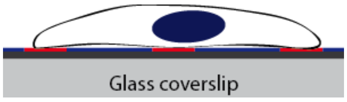 Glass coverslip

Table 2.1: Microfabrication of patterned glass substrates

1. Patterned coverslip preparation Protein adsorbed on a patterned glass coverslip at 37°C for 90min	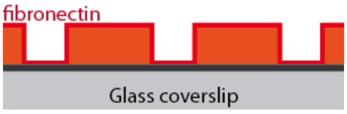 fibronectin Glass coverslip
2. Surface functionalization NaOH 0.1M + APTMS + glutaraldehyde prepared before gel preparation	Glass coverslip
3. Polymerization of first layer PAA solution polymerized between two glass coverslips at room temperature for 10 min layer thickness $\sim 40\mu m$	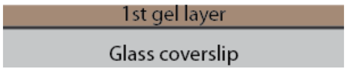 1st gel layer Glass coverslip
4. Polymerization of second layer PAA solution containing microbeads polymerized between 1^{st} layer and patterned glass coverslip at room temperature for 30 min layer thickness $< 10\mu m$ Top coverslip removed in PBS	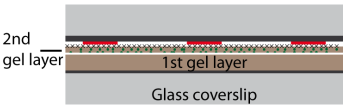 2nd gel layer 1st gel layer Glass coverslip
5. Lift-off of top coverslip Top coverslip removed in PBS	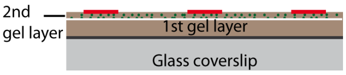 2nd gel layer 1st gel layer Glass coverslip
6. Final configuration Localized adhesive complexes of a cell spread on a soft substrate	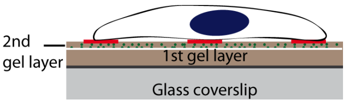 2nd gel layer 1st gel layer Glass coverslip

Table 2.2: Polymerization of patterned PAA gel

1. Si wafer preparation Wafer spin-coated with positive photoresist	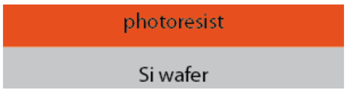 photoresist Si wafer
2. Photolithography and Etching Exposure + development + dry etching Depth of features controlled by etching time $\sim$ a few min PR finally stripped by a high-power plasma	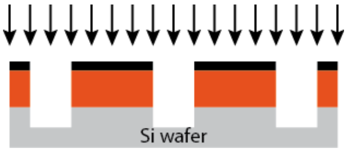
3. Si molds Si molds can be re-used multiple times, but need to be treated with surfasil before each use by evaporating surfasil on them for 30 min	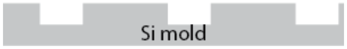
4. Molding + Curing of PDMS PDMS spin-coated on a coverslip and Si-mold pressed on top Curing time 45 min, 100°C	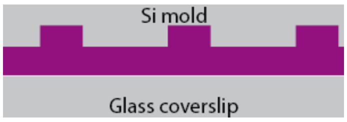 Si mold Glass coverslip
5. Activation of PDMS Si-mold lifted-off, PDMS activated by UV illumination, 30 min 16W	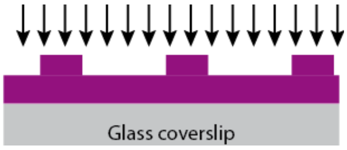 Glass coverslip
6. Stamping of PDMS substrate A glass coverslip uniformly coated with adhesive protein served as stamp Stamping for 1 min, applying mild pressure	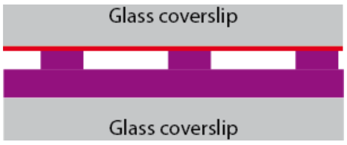 Glass coverslip Glass coverslip
7. Backfilling Pluronic 2% room temperature, 1 hour	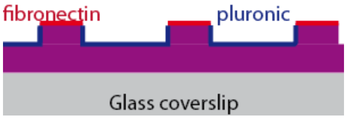 fibronectin pluronic Glass coverslip
8. Final 3-d patterned substrate Cell locally creates adhesion complexes	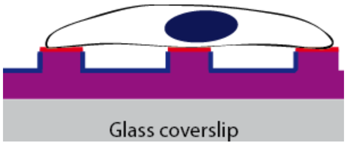 Glass coverslip

Table 2.3: PDMS substrate fabrication

2.3 Optical Microscopy

2.3.1 Wide-field microscopy

All imaging experiments presented in this work were done on an inverted Zeiss wide-field microscope (condenser NA = 0.55), which allowed simultaneous imaging of several fluorescent channels, as well as brightfield imaging. Fixed cells mounted in PVA in between two glass coverslips were imaged with a 63x oil immersion objective, with a numerical aperture of NA = 1.4. For TFM experiments, both a 63x oil objective and a 63x water immersion objective were used, the latter giving better results (see paragraph 2.3.2). For micromanipulation experiments, a 40x air objective (either NA = 1.3 or NA = 0.75) gave sufficient resolution and magnification. The maximal in-plane resolution at 63x was ∼230nm (given by $Res = 0.61\lambda/NA$). The out-of plane resolution was ∼713nm.

Fluorescence microscopy

Our system allowed to image up to 4 fluorescent channels simultaneously. We used a HBO or XBO arc lamp source, and neutral density filters to reduce intensity of incoming light, in order to reduce bleaching and phototoxicity. We indicate here the characteristic bandwidth of the filters, with some of the dyes and proteins imaged in those channels in the various experiments.

"COLOR"	$\lambda_{ex}/\Delta\lambda(nm)$	$\lambda_{em}/\Delta\lambda(nm)$	EXAMPLES
deep red	640/30	700/75	Alexa-Fluor 647
red	560/40	620/60	Alexa Fluor 568, TRITC
green	470/40	525/50	Alexa Fluor 488, FITC, GFP
blue	350/50	460/50	Alexa-Fluor 350, DAPI

Live imaging

Live imaging was done on the same system, the cells being immersed in special imaging medium that ensured a stable pH. Cells were stable in those conditions for many hours, though fluorescent light occasionally led to cell death when the cumulative exposure time was too high. To avoid this, neutral density filters were systematically used to reduce fluorescent light intensity during live experiments.

2.3.2 Traction Force Microscopy

Traction force microscopy is based on high-resolution imaging of bead displacements combined with potent image analysis and force reconstruction tools (section 2.5.2). Three channels were imaged at each time-point: the pattern (deep red), the beads (red) and the cells (GFP or transmitted light). The positions of fluorescent beads embedded in the gel were also recorded after the cells were detached from the gel using PBS/EDTA and trypsin. Since the beads were dispersed in the top layer of the gel of 10μm thickness, z-stacking was used to locate the ones nearest to the gel surface. From the z-stacks of a single bead, the point-spread-function of the system could be estimated, and used to deconvolve the images. The point-spread-function confirmed that an oil immersion objective is not well suited for traction force microscopy experiments. There is indeed a mismatch of refractive index at the immersion medium/glass coverslip/gel interfaces leading to abnormal reflections (n = 1.5 in oil immersion medium and through the glass, n∼ 1.3 in the gel), and in the end, aberration in the point-spread function (two distinct planes of maximal intensity, see Figure 2.2). For this reason, we switched to a 63x water immersion objective (compatible with inverted microscopes), NA = 1.2.

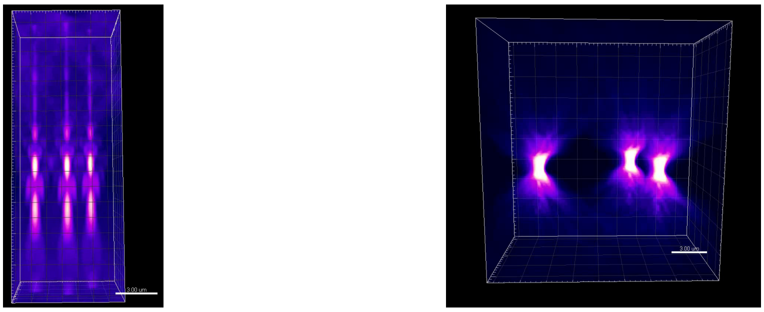

(a) Oil immersion objective **(b)** Water immersion objective

Figure 2.2: 3-d visualization of the point-spread-function of a fluorescent bead embedded in a gel (refractive index n = 1.37) immersed in water (refractive index n=1.33). a) With an oil-immersion objective (n = 1.5) b) With a water-immersion objective (n=1.3). Note that the refractive index mismatch leads to two high intensity peaks in a), whereas the point-spread function is symmetric in b).

2.4 Force Spectroscopy

2.4.1 Atomic Force Microscopy for gel stiffness measurements

To verify the stiffness of the PAA gels, we used an atomic force microscope (AFM) in force-spectroscopy mode on single layer, bead-free gels. A silicon nitride cantilever with a triangular tip was used (spring constant $40\text{nN}/\mu\text{m} \leq k \leq 180\ \text{nN}/\mu\text{m}$). The cantilevers were calibrated on a dry surface before use. Gel stiffness measurements were then conducted in water, to prevent it from drying from evaporation. The gel was indented at several locations (100 points/location) and the force feedback on the cantilever was measured by a 4-quadrant photodiode. Depth of indentation was kept below 10% of the gel thickness, around 2-5µm, so that the Hertz model could then be applied to the force-indentation curves (integrated in the JPK data processing software). In the range of validity of this model, the force is proportional to the Young Modulus E of the gel and to the square of the indentation. We then averaged E over all data points to obtain the gel stiffness. Gel stiffness measurement was repeated for each new preparation of PAA solution.

2.4.2 SU-8 cantilevers for fiber tension measurements

To deform cell peripheral fibers and measure their tension, Piacentini et al. [2014] have developed custom microfabricated cantilevers, with low spring constants suited to probe cellular tensions. Compared to other force-measurement techniques (AFM, micro-pillar arrays), these polymer cantilevers have the advantage that they can be used to directly probe the tension within a fiber, without necessitating an intermediate adhesive layer that could modify the mechanical interaction between cellular structure and probe. Furthermore, they are easily adaptable on an optical microscope stage, allowing easier sample visualization than with AFM. Cantilevers were designed as rectangular beams attached to a 50µm thick support layer (Figure 2.3a), both made in SU-8 epoxy photoresist, and fabricated by a double photolithography on a sacrificial aluminium layer. The size of the cantilevers were adapted to probe sub-cellular structures, with a thickness $t = 5\mu\text{m}$, width $w = 5$ or $10\mu\text{m}$, and height ranging from 500 to 1000µm. Different sizes allowed to tune the spring constant according to $k_c = E \cdot w \cdot t^3/(4h^3)$, E being the Young modulus of the material (5 GPa for SU-8). Spring constants were between 6.25 and 0.78nN/µm. Before experiments, a cantilever was glued on a supporting rod and could then be functionalized with fibronectin by treating the cantilever with an O_2 plasma (1 min, 100 W), then immersing them in a fibronectin solution for 30 min (20µg/mL), or alternatively passivated by immersing them in a 2% Pluronic solution for 30 min. This was to avoid cells from

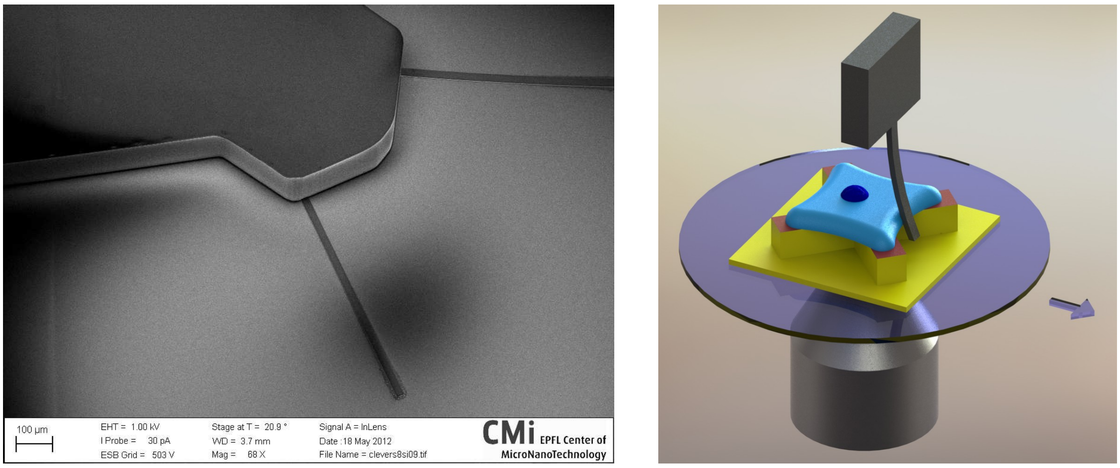

(a) Electron micrograph of a cantilever **(b)** Sketch of the setup

Figure 2.3: a) SEM view of two cantilever beams on their support. Scale bar 100µm. b) Sketch of a cantilever mounted vertically on a micromanipulator above the microscope stage. Micron-precision placement of the cantilever near the cell edge allowed controlled indentation/deformations of the fibers by moving the motorized stage. Reproduced from Piacentini et al. [2014].

sticking to the cantilever, and therefore being able to use the cantilevers multiple times. The cantilever was then mounted on a micromanipulator so as to hang vertically in the sample, and allow it to deflect in the plane of the cell. The micromanipulator was built of two 3-axis units (NMN-25 mounted on top of MX-1, both from Narishige Scientific Instruments Lab). The cantilever was first visually aligned in the center of the microscope's field of view using transmitted light and a 40x magnification, then positioned near the cell of interest. Deflections were applied to the cell in the x-y plane by moving the microscope stage, while the cantilever holder stayed fixed. Stage motion was controlled by custom software written in MATLAB. This setup is sketched in Figure 2.3b. Note that the SU-8 photoresist is autofluorescent over a wide spectrum, such that is was not possible to use these cantilevers on with transfected cells.

2.5 Image processing and analysis

2.5.1 Image treatment

Microscopy images were routinely treated with ImageJ tools to adjust brightness and contrast, subtract background, threshold images and measure cell areas. In fluorescent actin images, cell contour could be obtained by thresholding the image with the *Otsu* method. On bright-field images, manual detouring of the cell contour was performed. To improve image resolution, some stacks of images were deconvolved using the Huygens Deconvolution software.

Deconvolution

Fluorescence imaging with a wide-field microscope is a diffraction-limited technique, so the in-plane resolution and most of all the axial resolution are limited. The final image is the result of the convolution of the object image with the point-spread function of the system (microscope+objective). The point-spread function is the system's image of a point-like source (as in Figure 2.2). Deconvolution algorithms restore the object image from the knowledge of the point-spread function. This is useful to deblur images and improve the signal-to-noise ratio as well as the resolution. It can also be used for 3-d reconstruction. In this work images were deconvolved with the online Huygens software interface [www.svi.nl], using a theoretical point-spread function based on the specifics of the imaging system, and the software's integrated *Classic Maximum Likelihood Estimation* algorithm applied to a stack of images. The z-step of each stack was 200nm.

Image alignment

Both for the traction-force microscopy and the cantilever-based experiments, stack of images had to be aligned to determine movements from one time-point to the next of beads, pattern or cells. For this, we used an ImageJ plugin "Template matching" with the *normalized correlation coefficient* or *normalized cross correlation* algorithms, implemented by Q. Tseng, available on `https://sites.google.com/site/qingzongtseng/tfm`.

Measuring arc radii

The radius of curvature of actin arcs were measured using a custom MATLAB script on images thresholded manually using ImageJ (Figure 2.4). Briefly, the contour of the arc was detected, and then a circle was fitted to 3 points along the smoothed profile. The final radius is an average of at least 3 radii measured while moving the three points along the profile. The distance between the 3 points was adjusted to have a standard deviation below 10%.

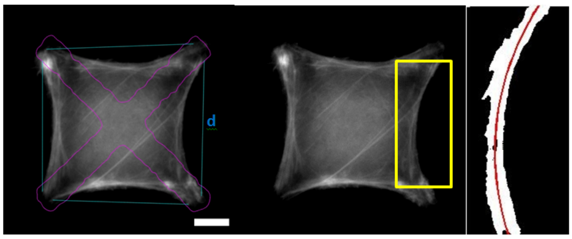

Figure 2.4: Example of arc curvature measurement. The arc's spanning distance were measured in ImageJ, and shown in the first panel in cyan. Each arc was then cropped (central panel) and the MATLAB script used to detect the arc contour profile (right panel) and measure its radius. Scale bar, 10µm.

2.5.2 Traction Force Microscopy analysis

Overview of force reconstruction techniques

Several numerical methods have been developed to reconstruct 2-dimensional traction stress distributions on soft matrices. Historically, Harris et al. [1980] have measured wrinkles on silicone-rubber substrates. Dembo and Wang [1999] have improved the idea by using acrylamide gels instead of silicone-rubber substrates, and then embedding fluorescent microbeads beneath the surface to measure gel strain. The first step of force reconstruction is thus to track bead displacements using Particle Image Velocimetry (PIV) or Particle Tracking Velocimetry (PTV) [Raffel et al., 2007]. The displacement field $\mathbf{u}(\mathbf{x})$ and the traction stress field $\mathbf{f}(\mathbf{x})$ are related by elasticity theory. In the case of an infinitely deep half space (which is the case if the gel height is much larger than the cell size), the direct relation can be expressed in function of the Green tensor $\mathbf{G}$ of the elasticity equation [Landau and Lifschitz, 1986]:

$$u_i(\mathbf{x}) = \int \sum_j G_{ij}(\mathbf{x}\text{-}\mathbf{x'}) f_j(\mathbf{x'}) \mathbf{dx'} \tag{2.1}$$

To calculate the traction stresses, the inverse problem giving the stresses in function of displacements has to be solved. There are several possibilities depending on 1) if a domain outside of which there is zero-force is defined (typically the cell contour) and 2) if the points of application of forces are known and are relatively small. Boundary-element methods define such a closed domain in which forces are applied, assume a theoretical stress distribution and compute the corresponding displacements. Then Tikhonov regularization is used to minimize the difference between the theoretical displacements and the measured ones [Sabass et al., 2008]. In the case where the points of applications are exactly known (typically if focal adhesions are marked), boundary-element methods can be simplified, in so-called point-force reconstruction methods [Schwarz et al., 2002, Sabass et al., 2008]. A third option called the “adjoint method” is also based on a Tikhonov regularization scheme, in which the displacements and traction stresses are calculated by finite element method on a triangular mesh [Ambrosi et al., 2009, Michel et al., 2012]. Alternatively, if no cell boundary or points of applications are given, the stress distribution can be computed exactly in the Fourier space (unconstrained method) on a regular rectangular mesh, assuming zero displacements far from the cell. FTTC has the advantage of being very fast in computation time and does not require boundary definition. These techniques are compared in Sabass et al. [2008], Michel et al. [2012]. For convenience, we chose Fourier Transform Traction Cytometry to reconstruct cell forces.

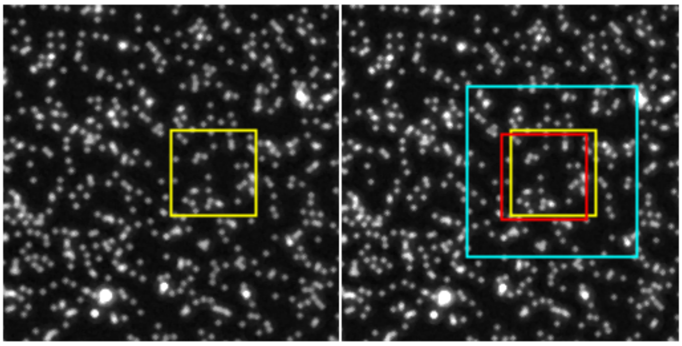

Figure 2.5: Template matching illustration on images of microbeads. The interrogative window is in yellow, the search window is in cyan.

For all traction force microscopy data presented in this work, bead displacements were computed using incremental Particle Image Velocimetry (PIV) and traction stresses were obtained by Fourier Transform Traction Cytometry (FTTC). Algorithms working with ImageJ were taken from Tseng et al. [2011] (detailed in the PhD thesis of Q. Tseng [2011]). The principles are detailed below.

Measuring bead displacements with PIV

PIV procedures are based on template matching algorithms which cut an image into smaller windows and look for how much each window is displaced from one time-point to the next. This is done by looking for the highest cross-correlation between the interrogative window (IW) and the displaced window. The search is limited to a search window SW = IW + 2MD (Figure 2.5). MD is the maximal displacement which can be estimated from the pattern deformation. This procedure is repeated at least 3 times reducing the size of the IW at each step. The previous displacement vector is used as guidance. The final displacement vectors for all sub-images gives the global displacement field at each time-point. For the traction force microscopy images, the smallest windows are 32px x 32px, with ideally 5-6 beads/window. Images are corrected (median filter and background subtraction) to allow better bead detection. Incremental PIV is done independently for each timepoint, comparing the image of the strained gel to a reference image of the unstrained gel taken after cells have been detached.

Force reconstruction using FTTC

To reconstruct the stress field, the susbtrate is assimilated to an infinite elastic half-space. The knowledge of the displacement field over the substrate (assuming zero displacement at infinity) enables us to compute the traction stress vectors at each grid point [Butler et al., 2002, Sabass et al., 2008]. The displacement field and traction stress field are related by the convolution of a Green function in the real space (eq. 2.1), which becomes a product in Fourier space. Inversing the relationship between $u_{i\mathbf{k}}(\mathbf{x})$ and $\tilde{f}_{i\mathbf{k}}$ yields the traction stress vector which is then back-transformed to real space.

$$\tilde{u}_{i\mathbf{k}} = \left\{ \sum_j \tilde{G}_{ij} \tilde{f}_j \right\}_{\mathbf{k}} \qquad \tilde{f}_{i\mathbf{k}} = \left\{ \sum_{l,j} \left[\sum_m \tilde{G}_{ml} \tilde{G}_{mi} + \lambda^2 \tilde{H}_{il} \right]^{-1} \tilde{G}_{ij} \tilde{u}_j \right\}_{\mathbf{k}}$$

The Boussinesq Green function for an elastic half-space is given by Landau and Lifschitz [1986]:

$$\tilde{G}_{ij\mathbf{k}} = \frac{2(1+\nu)}{E} \left[\frac{\delta_{ij}}{k} - \frac{\nu k_i k_j}{k^3} \right]$$

λ is a regularization factor and $\tilde{H}$ the regularization kernel. E and ν are the Young modulus and the poisson ratio of the gel. Typically, $\lambda = 9e^{-10}$, and $\nu = 0.5$. E is measured by AFM force spectroscopy (section 2.4.1).

Double thresholding

The FTTC algorithm used is unconstrained and with no boundary condition, contrary to other methods of force reconstruction. Therefore there are no imposed condition on the localization of forces. One reason this algorithm was chosen is that the localization of the traction forces are not explicitly known, for fluorescent marking of focal adhesions was not available. To calculate the magnitude of the local traction forces, it was therefore necessary to determine a region over which to integrate the traction stress vectors, corresponding more or less to adhesion sites. The actual width of the regions was larger than adhesions because of the discretization steps in the computing of forces. The stress maps were first interpolated on a smaller grid (MATLAB cubic interpolation function). Forces were then calculated by applying a double threshold to the stress map that enabled to isolate the regions of traction stresses and calculate the resulting force vector for each region. The threshold levels were determined on a cell-per-cell basis, using MATLAB image processing tools.

2.6 Numerical methods

All numerical procedures were done using custom MATLAB scripts and existing MATLAB functions. In Chapter 4 the implicit equation linking the radius to the elastic line tension (eq. (4.6)) was solved using the integrated solver *fsolve*. Fitting simple functions was done using the programmable fitting tool *fit* with the *Non Linear Least square* method. In Chapter 5 the elastic tension model was fitted using the *NonLinearModel* tool.

Chapter 3

Extracellular matrix geometry triggers a reorganization of the cytoskeleton

Whether in an organism, in a tissue explant, or in a culture dish, a cell's physical microenvironment is important for cell function. The extracellular matrix' geometrical properties (dimensionality, roughness, curvature), biochemistry (available ligands) or mechanical properties (stiffness) are known to influence cellular processes, as detailed in Chapter 1. In particular, the organization of the actin cytoskeleton, and its progressive layout during cell spreading are determinant for subsequent cell behavior. Cell size and shape, the positioning of cellular organelles, the creation of cell-cell or cell-substrate adhesive contacts, all these will depend on proper cytoskeleton function, and on the distribution of cytoskeleton tension. Understanding what controls cytoskeleton organization, and being able to impact it in bio-engineering applications, is therefore essential for future studies of cell biomechanical behavior. Micropatterning tools have been previously used on 2-dimensional or 3-dimensional surfaces to control the cell's total area, its adhesive area and the localization of adhesions. It is now demonstrated that such constraints on cell spreading affect not only cell shape but also the structure of the cytoskeleton and have downstream consequences on genetic expression and cell fate [Chen et al., 1997, Engler et al., 2006, Théry et al., 2006b]. However, the mechanisms involved in geometry sensing at the sub-cellular level are not fully understod. In this chapter, we focus on how discrete adhesive patterns can influence the organization of the actin-myosin cytoskeleton. Both the organization of the cytoskeleton, its connectivity to cell-ECM adhesions, and its tensional state are studied in relation to the adhesive geometry. In the first section, we specifically look into how non-adhesive gaps modify the formation of acto-myosin bundles. In the second section, we look at the force distribution resulting from the discretization of adhesive geometry.

3.1 A length maturation threshold[1]

Adherent cells on glass substrates display a very symmetric cytoskeleton layout and regular arrangement of focal adhesions around the cell periphery. This regularity is most likely a specific feature of *in vitro* studies, since in their natural environment, no such continuum of adhesion is possible. Fibroblasts *in vivo* attach to available fibers of the ECM, which having a 3D geometry, are intrinsically not plane or smooth. Furthermore, the mechanical properties of the ECM may vary locally. The distribution of adhesion sites is thus most probably inhomogeneous. The question is to what extent does a non-uniform distribution or a default of adhesion impact cell shape and cell function. How could it lead to cytoskeleton remodeling? To address these questions, we resort to discrete adhesive micropatterning, in which we impose non-continuous adhesive geometries. The patterns are circular, typically the size of a single-cell (30 to 50μm radius), with micron-sized features. Seeding fibroblasts on these micropatterns enabled us to isolate single cells, locally constrain the cytoskeleton and control adhesion localization in a reproducible way.

Cells spreading in between adhesive lines tend to form thick acto-myosin bundles at the cell periphery with a concave curvature [Théry et al., 2006a, Rossier et al., 2010]. Although these peripheral bundles may form as well on homogeneous substrates, they are more prominent on micropatterned substrates. Experiments on deformable micro-pillars [Lehnert et al., 2004] or theoretical analyses of stress distributions [Deguchi et al., 2011] indicate that there are high forces at the end of these bundles. For these forces to be transduced to the substrate, the minimal requirement is that the bundles be connected to focal adhesions. It thus appears that high force magnitude and the presence of adhesions are both important in the formation of these peripheral bundles.

In a theoretical paper presenting numerical simulations of cell spreading, Loosli and co-authors have predicted that these peripheral bundles should form and remain stable above a certain length, and that through these bundles, centripetal forces are converted to tangential forces at the leading edge [Loosli et al., 2012]. In this hypothesis, the nascent adhesions present at the lamellum/lamellipodium interface (LM/LP) are stabilized by the anchoring of acto-myosin bundles. If these bundles are long enough, they will collect large

---

[1] Results of section 3.1 are published in Loosli, Labouesse et al. [2013]

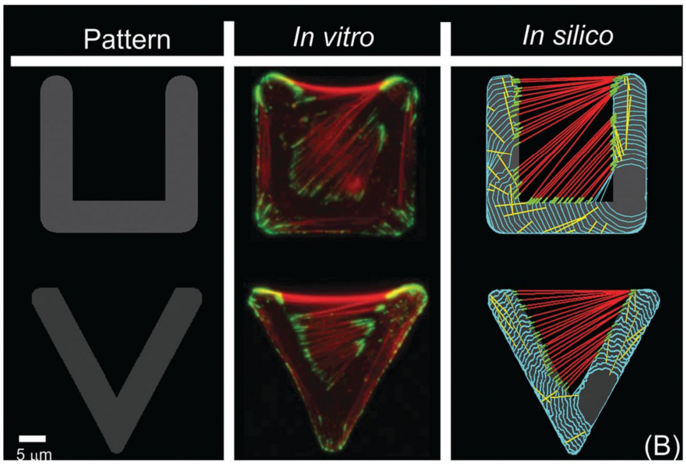

Figure 3.1: Comparison of numerical simulations and experimental results. Left: adhesive patterns “V” and “U” on glass substrates. Center: fixed cells spread on those patterns, with actin stained in red, vinculin in green (reproduced from Théry et al. [2006a]). Right: cytoskeletal morphologies after 30 min spreading predicted by numerical simulations. Red lines represent stable actin bundles anchored at mature focal adhesions (green). Yellow lines indicate other stable actin bundles. Unstable bundles are represented by blue lines. Similarity between experiment and simulation is striking: stable actin bundles on the non-adhesive regions are non-crossing and span from adhesive edge to adhesive edge. Figure adapted from Loosli et al. [2012].

centripetal forces (i.e. forces normal to the interface, directed inward), and balance it by tangential forces at their ends, eventually triggering adhesion maturation. Otherwise, the nascent adhesions will turnover and the acto-myosin bundles will drift inwards. This hypothesis, called the length maturation threshold (LTM), was tested by comparing the outcome of numerical simulations of cell spreading with existing experimental data (Figure 3.1). From these simulations, Loosli and co-authors predicted the threshold length to be 5µm for REF52 cells. A similar force threshold mechanism was also unveiled during polarization of fibroblasts [Prager-Khoutorsky et al., 2011]. Although it was specific to the polarization process, while the LTM may be active already during spreading, similar underlying biomechanical pathways may be involved in both processes, such as the force-dependent maturation and orientation of focal adhesions [Balaban et al., 2001, Bershadsky et al., 2003]. The LTM has been empirically validated, but not directly tested experimentally. We here present experimental evidence in support of the LTM hypothesis, showing that cytoskeletal remodeling is dependent on the adhesive geometry. For this we use circular micropatterns with 8 non-adhesive gaps of different widths, ranging from 2µm to 10µm (the fabrication process is described in 2.2.1). For readability, the patterns are designated by the gap width in the rest of this chapter.

3.1.1 Methods

Image and data analysis

The aim of image analysis was to identify actin bridges and distinguish them from other actin structures. A four step process utilizing information from all three fluorescence image channels (the adhesive pattern, actin filaments and focal adhesions) was structured as follows: (i) manual identification of tangential actin bundles, (ii) selection of bundles spanning non-adhesive regions of the substrate, (iii) bundles terminated by a single adhesion (vinculin only colocalized at one extremity of the actin bundle) were discarded and finally (iv) in the case of parallel actin bundles, only the most distal bridging bundle was considered (yielding a maximal number of 1 bridge per substrate gap, thus eight bridges per cell at the most). Once the number of actin bridges per cell was assessed, the number of non-adhesive gaps effectively bridged by the cell was used to compute the "bridging ratio". The bridging ratio, calculated for each cell, was defined as the ratio between the number of actin bridges per cell and the total number of gaps covered by the cell body. For instance, a bridging ratio of one indicates an actin bridge across each non-adhesive gap. By definition the bridging ratio was always less than or equal to one. Bridging ratio distributions for each group were compared using a Kruskal-Wallis test assuming independent samples with different variances. Kruskal-Wallis is a statistical test used to determine if several groups of data come from the same distribution. It is as such a version of the ANOVA test, but does not assume normal distribution of the population. Each cell was regarded as an independent measurement assuming that the inter-pattern distance (55 µm) was sufficient to provide a single cell experiment. Significant differences were identified for a p-value less than 0.01, after applying Bonferroni correction to compensate for multiple comparisons. Statistical analysis was performed using MATLAB. Distances between the terminating focal adhesions of actin bridges were measured using ImageJ. Error in localization of the actin bundle ends was generally less than 2 pixels (approximately 0.25 µm). This inexactitude corresponds to a maximal inaccuracy of 0.5µm in the assessment of adhesion site spacing (and the corresponding bundle length).

3.1.2 Cytoskeleton organization controlled by discrete adhesive patterns

From a mesh-like to a parallel arrangement of the cytoskeleton

Cells were seeded on the micropatterned substrates and left to spread for several hours, then fixed and stained for actin and adhesion proteins. We observed that non-adhesive zones favored the formation of thick acto-myosin arcs. As is shown in Figure 3.2, panels (A)

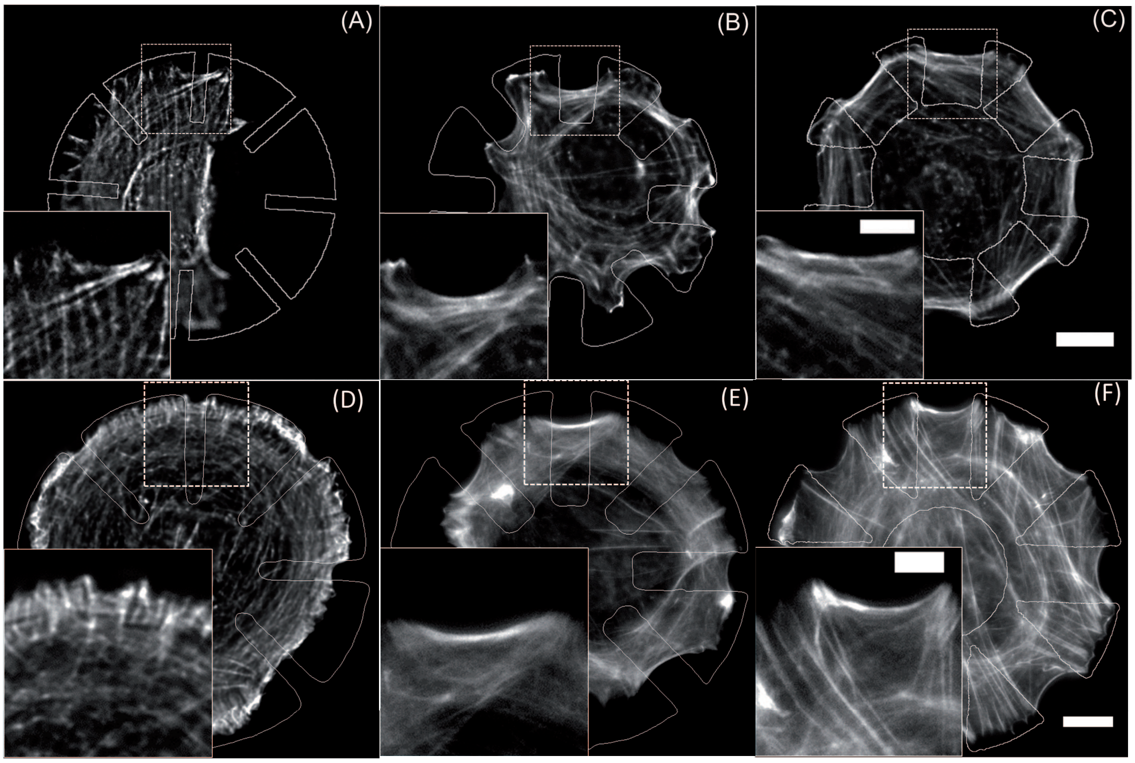

Figure 3.2: Non-adhesive gap width influences the local actin organization. Actin organization in 3T3 (A-C) and SCF (D-F) spread on 2, 6 and 10µm micropatterns, respectively, in panels (A, D), (B, E) and (C, F). Overlays delimit the adhesive patterns. While cells on the 2µm pattern showed a mesh-like actin organization not influenced by non-adhesive regions (A, D), in cells on 10µm patterns there were mainly strong bundles distally delimiting the cell (C, F). Pattern sizes are 2000µm^2 for 3T3 and 4000µm^2 for SCF. Bars are 10µm and 5µm in insets.

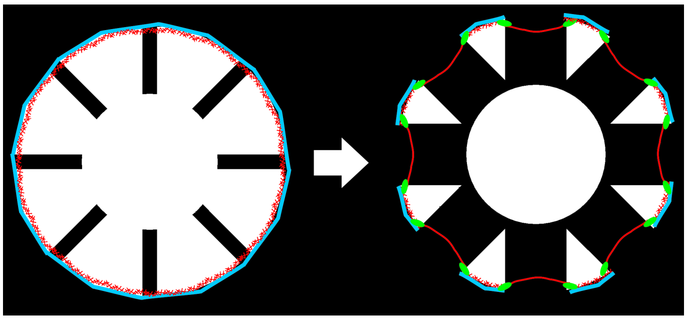

Figure 3.3: Schematic of the actin cytoskeleton reorganization depending on non-adhesive gap width. On small gaps (left) a meshwork organization is found at the leading edge, while over large gaps thick bundles bridging the gaps are observed instead.

and (D), on small gaps, the actin network at the leading edge is similar to what is observed on homogeneous adhesive areas, with a mesh-like organization. The non-adhesive gap did not appear to impede or modify cytoskeleton assembly. In contrast, on gaps wider that 6µm (Figures 3.2, panels (C) and (F) and Figure 3.3), no mesh-like network was observed. Instead, thick acto-myosin bundles bridged the gaps at the cell periphery, occasionally supported by other bundles, parallel to the first one. The arcs were attached to focal adhesions at their ends, similar to what had been previously observed in Théry et al. [2006a] and Rossier et al. [2010]. Cells seeded on the 6µm pattern exhibited a mixed mode: on adhesive regions the actin network was similar to the mesh-like organization observed on the 2µm pattern, whereas non-adhesive regions were bridged by acto-myosin bundles.

Molecular composition of peripheral arcs

To characterize the structure of the peripheral acto-myosin bundles in more detail, we fixed cells spread on cross-shaped patterns with large non-adhesive gaps and immunostained target proteins: F-actin, isoforms IIa and IIb of non-muscle myosin II and α-actinin. We found that the bundles are densely cross-linked by α-actinin and by both isoforms of myosin, though myosin IIb was more concentrated, while myosin IIa was more diffuse (Figure 3.4). In this respect, these peripheral stress fibers were thus similar to transverse arcs, which also contain myosin II and α-actinin [Hotulainen and Lappalainen, 2006]; in contrast, they differ in structure from dorsal SFs which do not contain myosin II. Notably, the arrangement of the cross-linkers in the bundles was not periodic as in sarcomeric muscle fibers, as shown in the profiles in Figure 3.4B. The profiles nonetheless displayed multiple zones rich in myosin and α-actinin consistent with series of (non-identical) contractile units.

Redirection of tension by micropatterning

Focal complexes elongate in the direction of applied forces [Balaban et al., 2001]. Their orientations are therefore a good indicator of the directions of forces during spreading. Both the peripheral arcs and the end-point adhesions were oriented parallel to the leading edge, in contrast to dorsal stress fibers which are arranged radially. The evidence shown in Figure 3.5 indicate that the peripheral arcs pull on the FAs tangentially to the leading edge (adhesions delineated in yellow), in contrast to dorsal SFs (adhesion delineated in red). The presence of non-adhesive gaps therefore led to a redirection of cellular tension from radial forces to tangential forces. Recently, the influence of adhesive branches as well as non-adhesive gaps on redirecting tension has been further demonstrated by Mandal et al. [2014], who found that the orientation of traction forces and global cell polarization could be selectively controlled by adhesive geometries.

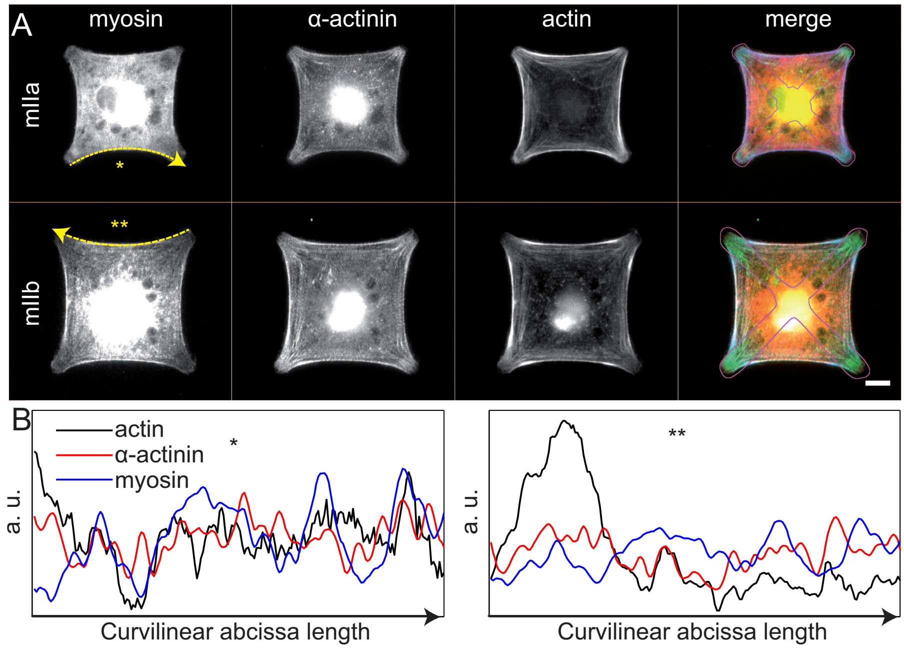

Figure 3.4: Architecture of peripheral acto-myosin bundles. A) Fluorescence images of REF52 cells on cross-shaped patterns, showing isoforms IIa (top row) or IIb (bottom row) of non-muscle myosin II, α-actinin and F-actin. The last column is a merge of all 3 proteins (myosin in red, α-actinin in green, actin in blue, the contour of the adhesive pattern is shown in magenta). Scale bar, 10μm. B) Intensity profiles along one bundle of actin, α-actinin and myosin, respectively in black, red, and blue, showing multiple zones rich in myosin II and α-actinin. Profiles were normalized by the mean intensity over the bundle length. Note that no periodic bands were observed. The corresponding bundles and the scanning direction are indicated by (* or **) and yellow arrows in (A). Bundle lengths are 40μm (*) and 50μm (**).

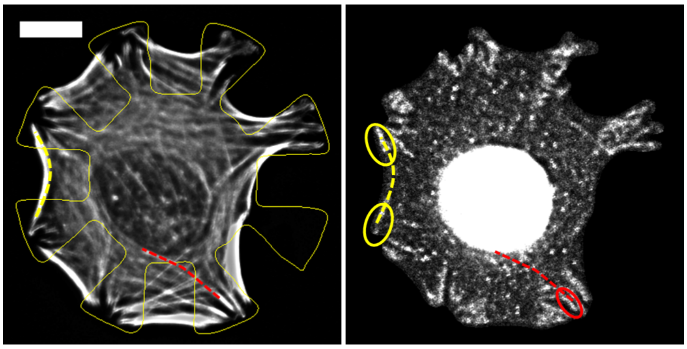

Figure 3.5: 3T3 spread on a 8μm micropattern exhibiting distinct actin bundle and adhesion orientation due to the length threshold maturation. Actin (left) and vinculin (right) visualization allow identifying peripheral actin bridges (yellow dashed lines) from the other actin bundles (red dashed line). Focus on the actin channel enables to distinguish the most peripheral bundle from the others. The vinculin channel permits the localization of the end-point adhesions (yellow and red ovals) and therefore distinguishing dorsal stress fiber with a single ending adhesion from the actin bridges. Bar 10μm.

Adhesive anisotropy during spreading triggers the formation of bridges

The analysis of fixed cells on the discrete adhesive patterns suggests that the switch from a mesh-work architecture to a bundle architecture is triggered by anisotropy in the adhesion geometry. This anisotropy is created here by the non-adhesive gaps, but can be enhanced by the asymmetry of cell spreading and the presence/absence of lamellipodia along the leading edge. Indeed, if cell spreading is anisotropic, the effective non-adhesive gap to be bridged will be greater. To illustrate how spreading anisotropy modifies cytoskeleton organization, we imaged cells spreading on patterns with gaps 8µm wide (Figure 3.6). The cell first extended lamellipodia on the adhesive zones on either sides of the gap. The left and right bridges after 13 minutes of spreading are an example of how different directions of spreading on each adhesive branch may create an effective larger gap (right gap) compared to radial (symmetric) spreading (left gap). When the cell reached the end of the adhesive zone, the cycles of protrusion/retraction resulted in no net advance of the cell edge, but instead in a steady-state protrusion. In between neighboring lamellipodial protrusions, actin bundles were formed delineating the LM/LP interface, as has been also observed elsewhere [Alexandrova et al., 2008, Choi et al., 2008, Shemesh et al., 2009; 2012, Burnette et al., 2011]. In our case, this bundle was stabilized, by strong anchorage at focal adhesions, and persisted for over 40 minutes, advancing progressively as the cell continued to spread and the LM/LP interface moved outwards. This bundle bridging the non-adhesive gap was also reinforced by other parallel bundles being accumulated behind it. The temporal analysis confirms that the bridges are strongly attached to adhesion complexes, since they are present throughout many cycles of protrusion/retraction. Peripheral acto-myosin bundles are thus more stable than transverse arcs, which quickly disappear into the lamellum.

3.1.3 Evidence for an actin length threshold controlling the maturation of focal adhesions

Behavioral switch: bridging ratio

To find out how the change in the actin network architecture at the leading edge might depend on the distance between adhesions, we estimated the number of gaps on which cells used parallel bundles arrangements versus those with meshwork arrangements. For each cell, we computed the bridging ratio (number of bridged gaps/number of occupied gaps). Only distinct tangential circular peripheral bundles were counted as bridges; in those cases where several thick bundles were entangled, or if a bundle was tilted and pulled inwards creating a kink, it was not possible to define a single bridge with a given curvature, and

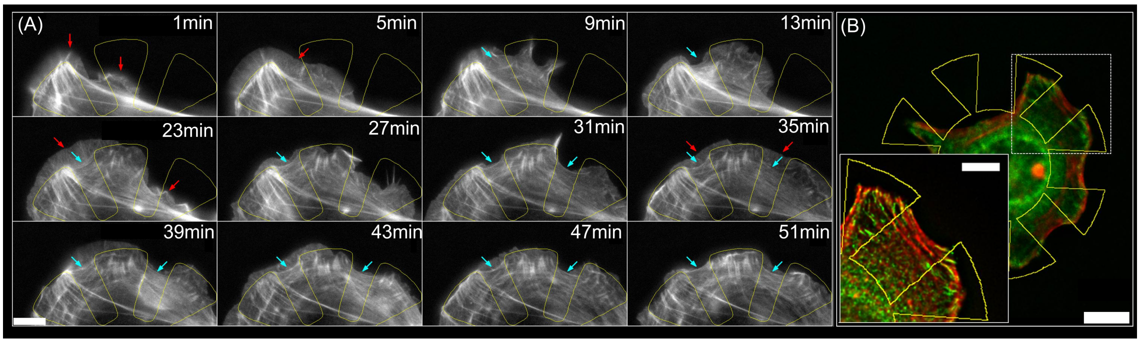

Figure 3.6: (A) Image sequence of a SCF transfected with LifeAct-EGFP spreading on a 8µm gap pattern. The importance of asymmetrical lamellipodial protrusions in actin bridge formation can be clearly seen. Asynchronous protrusion of two lamellipodia (indicated by red arrows) on two distinct adhesive regions is shown in the 1st frame. These two lamellipodia eventually merge (5 min) and give rise to a new LM/LP interface over the non-adhesive gap. The actin bundle bridging the gap is indicated by the cyan arrow (frames from 9 min to 43 min). After 27 min, the same process is observed on the right non-adhesive gap, giving rise to an actin bridge (right cyan arrow, frames 31 min to 43 min). The position of the arrows is the same throughout the frames, showing the great stability of the bridges over more than 30 minutes, corresponding to many protrusion/retraction cycles of the leading edge (novel LP protrusions marked by red arrows). At 23 min (middle adhesive area) and 35 min (right adhesive area), the initiation of dorsal SF oriented towards the cell center is seen. The yellow overlay delineates the pattern. Scale bar is 10µm. (B) Successive actin bridge formation actin (red) and vinculin (green) channels representing a cell with actin bridges arranged in parallel that span non-adhesive gaps of 6µm width. The adhesive pattern is shown in yellow overlay. The white frame shows the zoomed-in region in the inset. Bars are 10µm (full frame) and 5µm (inset) respectively.

these were therefore discarded. We first confirmed that cell area did not have an impact on bridging ratios, such that the gap width was the only significant variable (using Kruskal-Wallis test, p>0.01). Comparing bridging ratios for cells on patterns of same gap width but of different size (1000µm^2 and 2000 µm^2 for 3T3 and 3000µm^2 and 4000µm^2 for SCF), showed no significant differences. We therefore grouped the data from cells on patterns of different areas but with gaps of same widths. The results are shown in Figure 3.7a. On 2µm gaps, there were very few actin bridges (median bridging ratio: 0.29 for 3T3, 0.25 for SCF, 0.10 for REF cells); on 4µm gaps, both types of network (mesh-like or bundles) were seen (median bridging ratios 0.38, 0.63 and 0.32, respectively); on gaps wider than 6µm parallel bridges were systematically observed in the case of 3T3 and SCF (100% bridging for 3T3 cells; for SCFs, median bridging ratio of 1, 5th percentile of 0.88, 0.7 and 0.83 on gaps 6, 8 and 10µm wide, respectively). The bridging ratios on small gaps ($\leq$ 4µm) were significantly different than on larger gaps ($p < 0.01$), evidence of a geometry-triggered behavioral switch.

Behavioral switch: bridge lengths

The hypothesis of a length threshold presented in Loosli et al. [2012] was that bridges would be stable above 5µm in REF52 cells. The bridging ratios measured are partially consistent with this hypothesis, since there is clearly a different morphology of actin network on gaps

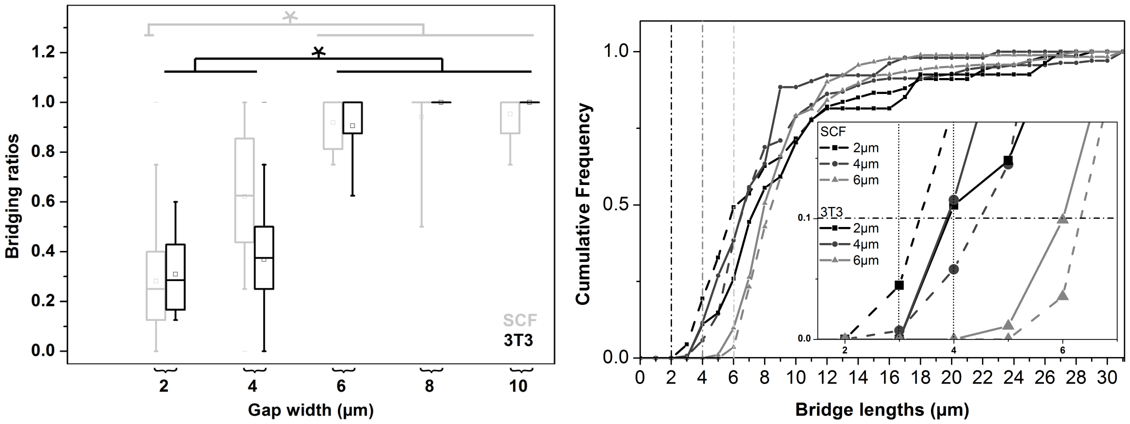

(a) (b)

Figure 3.7: (a) Bridging ratios for 3T3 (black) and SCF (gray). The box represents the interquartile range (region between the 25th and the 75th percentiles), the bars represent the 5th and the 95th percentile. The median value is indicated by the line in the box, whereas the square indicates mean values. Maxima and minima are denoted by dashes. The groups that are significantly different according to a Kruskal-Wallis test are marked by * ($p < 0.01$). (b) Cumulative distribution of actin bridge lengths found on different patterns. Data measured on 3T3 cells (solid lines) and SCF (dotted lines) on patterns with 2µm, 4µm and 6µm gaps. Vertical lines are cursors showing the gap width for each population. In the inset is a zoom-in of the graph. The legend indicates the gap width of the patterns. A horizontal cursor at 10% of all bridges is used for easier comparison of each curve: for 3T3 the bridge lengths on 2µm gaps and 4µm gaps are initially similar, starting at the hypothetical LTM threshold value of 4µm. The shift of the curve for larger gaps is inherent to the pattern geometry since it corresponds exactly to the gap width. This shows that the LTM is below 6µm. For SCF, the curve for the smallest gap is the most informative, showing an increase of the number of bridges longer than 3µm. Vertical dotted lines show the thresholds at 3µm (respectively 4µm) for SCF (resp. 3T3).

below 4µm and above 6µm. It was, however, unexpected to find bridges as well on the smaller gaps. We therefore measured the length of the bridges, for all the gap sizes. We neglected here the curvature length of the arcs, but considered instead the spanning distance between the end-point adhesions. We found that on the larger gaps, the bridges usually spanned just the width of the non-adhesive gap. However, for the smallest gaps of 2µm wide, the minimal bridge length was of 3.9µm for 3T3 cells, and 3.1µm for SCF (see cumulative distributions of bridge lengths, Figure 3.7b). It thus appears that bridges can also be formed on small gaps, most probably driven by spreading anisotropy. Notably, there still is a minimal length of 4µm in 3T3 (resp. 3µm for SCF), which is fully consistent with the hypothesis of a length maturation threshold. From our data, we can thus estimate that this threshold is lower for SCF than for 3T3; this can be explained by the higher contractility of SCF.

Effect of myosin inhibition on bridge formation

The two essential conditions for the formation of bridges, according to our hypothesis, are anisotropy in the adhesive layout, and a mechanism to convert myosin radial forces to tangential forces in a length-dependent manner. The length threshold mechanism is thus expected to be dependent on cell contractility, an expectation supported by the comparison of bridges' lengths in 3T3 and SCF. Centripetal forces indeed originate from myosin activity in the lamellum, and are then converted to tangential forces at adhesions by the peripheral bundles. At lower contractility, a longer bundle length would be needed to reach similar level of forces at adhesions. This could be tested by estimating the length-threshold in myosin-inhibited cells. However, one caveat is that the formation of peripheral bundles is likely also dependent on myosin activity. Svitkina et al. [1997] and Burnette et al. [2011] indeed describe the formation of transverse arcs by the myosin-driven condensation of actin filaments during lamellipodial retraction. The mechanism of peripheral bundle formation is expected to be similar, with the difference that they remain at the cell edge rather that flowing inwards as is the case for transverse arcs, being solidly anchored at focal adhesions. Inhibiting myosin might prevent bridge assembly altogether. To avoid this, low concentrations of inhibitor were used.

To assess how bridge formation and the length threshold are dependent on myosin activity, we treated fibroblasts with blebbistatin. Adding 50µM blebbistatin after 4 hours of spreading resulted in arcs being much less defined (irregular contours). The bridging ratios were lower for all gap widths, and more significantly, in a greater variance overall of the ratios. Consequently, no abrupt behavioral switch was evident in this case. The bridge lengths' were not significantly different from the control case, though here the variance was much lower, indicating there was a smaller range of distance over which actin bundles did remain stable. Since blebbistatin was added only after formation of the bridges, this only shows that myosin contributes to the stability of bridges. When blebbistatin was added during spreading (at a lower concentration of 10µM to 20µM, fewer thick bundles were observed, and the bridge lengths were significantly higher (Figure 3.8). Note that blebbistatin also increases protrusive activity, leading to larger lamellipodia. This could diminish the spreading anisotropy and counterbalance the asymmetry of adhesive patterns. Overall, inhibiting myosin with low concentrations of blebbistatin limited the cytoskeletal reorganization expected on patterns with large non-adhesive gaps but did not totally prevent the formation of bridges. We conclude that peripheral actin bundles can form in the absence of myosin, but are less stable.

3.1.4 Mechanism of bridge formation

Brought together, our observations of bridging ratios and bridges' lengths (Figure 3.7) show that there is a behavioral switch above a certain length threshold, which lies around 4µm for 3T3 cells and around 3µm for SCF, and that myosin contractility is essential to

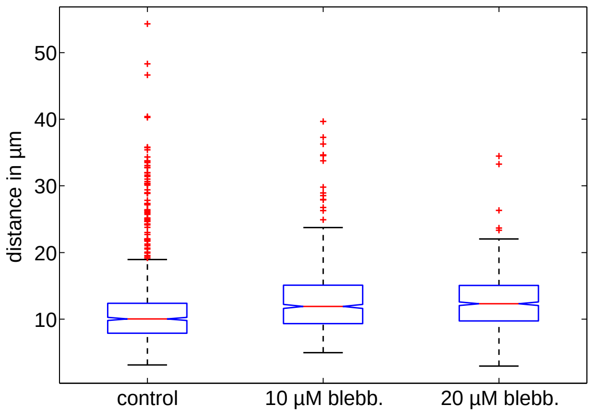

Figure 3.8: Spanning distances of SCF bridges in control conditions, and when blebbistatin was added during spreading at 10µM and 20µM. Boxes indicate the median of the distribution (red line) and the 25th and 75th percentile. Whiskers give extrema, red points outliers. Notched parts show the confidence interval of the median ($p < 0.05$). N = 907, 187 and 178 from left to right.

the stabilization of these bundles. This behavioral switch could reflect two different events: stabilization of acto-myosin bundles occurs only above a certain length and/or mesh-like networks require some amount of adhesive surface for assembly and maintenance. The latter hypothesis could be justified by the association of nucleating factors (Arp2/3) to focal adhesions. However, it is not sufficient to explain bundle lengths greater than 4µm, including on homogeneous substrates or on patterns with smaller non-adhesive gaps. We explain this minimal bundle length by the fact that a certain amount of force is needed to stabilize and maintain focal adhesions.

We thus propose, following the hypothesis of Loosli et al. [2012], that bridge formation is a result of anisotropy in the layout of focal adhesion and of a length-dependent maturation of focal adhesions. Spreading anisotropy may be created or enhanced by patterning, or may come from intrinsic spreading asymmetry (see sketch in Figure 3.9). The latter depends on the local direction of spreading with respect to the non-adhesive gap orientation, and on the protrusive activity. Indeed, the waves of lamellipodial protrusions contribute to the LTM process by locally accumulating bundled actin filaments, as seen in Figure 3.6. In contrast to other models based on the polarization of stress fibers [Prager-Khoutorsky et al., 2011], the LTM mechanism of bundle stabilization is sufficient to explain the tangential orientation of focal adhesions and peripheral stress fibers independently (and prior) to any polarization process. The mechanism is sketched in Figure 3.10. Myosin first leads to the parallel bundling of actin filaments by initiating retraction of the lamellipodium. The bundles then co-localize with focal complexes, stabilizing the bundle parallel to the leading edge. Myosin centripetal forces are accumulated along the bundle length, such that the balancing forces at adhesions scale with the bundles' spanning distance. The force-dependent maturation of adhesions lead to stable anchoring of bundles exceeding a length threshold and to a tangential orientation of the terminating focal adhesions (Figure 3.9). The experimental evidence put forward here shows the close relation between the organization of the cytoskeleton and myosin contractility. In the next section, we investigate further a central underpinning of this hypothesis, namely the relation between force and bundle length.

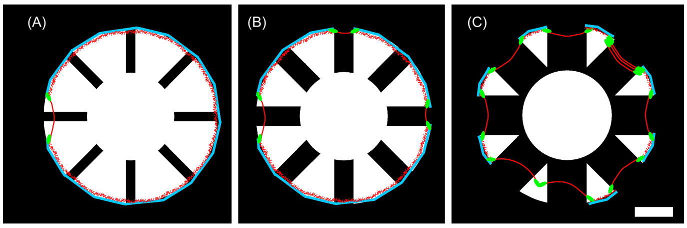

Figure 3.9: Schematic representation summarizing actin bundle organization and adhesion layout. Bridging occurred on all tested patterns, becoming frequent on 4μm patterns and systematic above 8μm. White regions correspond to adhesive zones, black to non-adhesive zones. Actin filaments are presented in red, adhesions in green, and lamellipodia in blue. Pattern size 1000μm^2, scale bar 8μm.

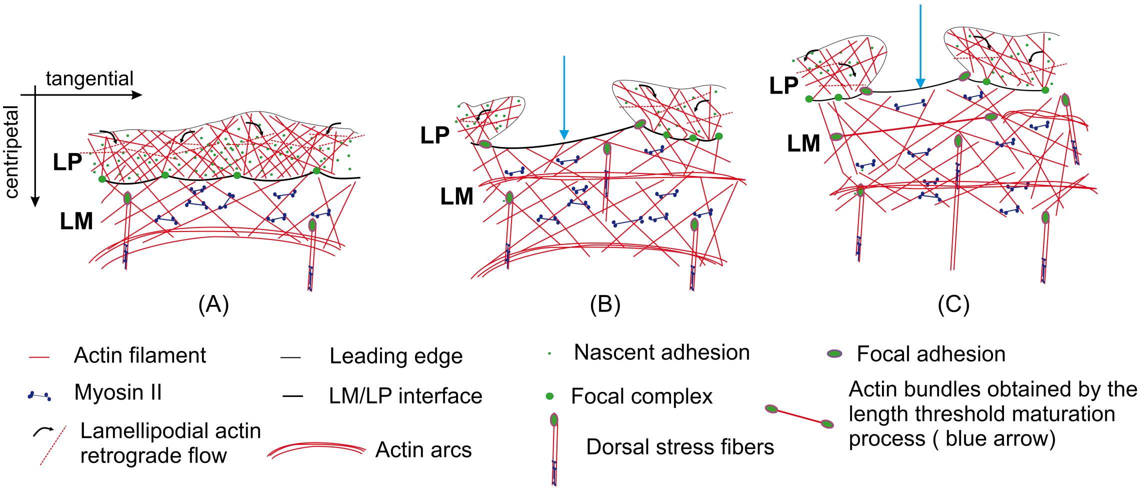
tangential
centripetal
LP
LM
LP
LM
LP
LM
(A)
(B)
(C)
Actin filament
Leading edge
Nascent adhesion
Focal adhesion
Myosin II
LM/LP interface
Focal complex
Actin bundles obtained by the length threshold maturation process (blue arrow)
Lamellipodial actin retrograde flow
Actin arcs
Dorsal stress fibers

Figure 3.10: Schematic representation depicting actin cytoskeleton remodeling and adhesion site reorganization triggered by the length threshold maturation (LTM). (A) Initial configuration, where the lamellum (sparse actin filament network with myosin II activity), the lamellipodium (dense actin filament network beneath which nascent adhesions are generated), the actin arcs and dorsal stress fibers are visible. Here drifting actin filaments in the lamellipodium (retrograde flow represented by black arrows and dashed red lines) interact with nascent adhesions to elicit a shift of the LM/LP interface toward the leading edge. Along with the LM/LP interface shift, actin filaments and adhesion sites reorganize as shown in (B). A novel LP protrudes distally from this new limit, whereas proximally myosin II crosslinks with actin filaments in the lamellum. The focal complexes that earlier formed the LM/LP interfaces are now dissolved and the actin bundles linking the focal complexes migrate toward the cell center as forming actin arcs. The blue arrows indicate segments of the LM/LP interface that link two focal complexes. Due to local inhomogeneity in the lamellipodial protrusions, the nascent adhesions anchoring this bundle are separated by a distance larger than a "maturation length". As a consequence the terminating focal complexes mature into focal adhesions that stabilize the interconnecting bundles and locally arrest lamellipodial activity. Such a mature bundle is visible in the lamellum on (C). Note the coordinate system defining the tangential direction (locally aligned with the leading edge) and the centripetal direction (orthogonal to the tangential direction). Image from Y. Loosli, adapted from [Loosli, Labouesse et al., 2013].

3.2 A geometry-dependent force balance

In the first part, we used the orientation of focal adhesions to illustrate the redirection of cellular tension from radial to tangential forces (Figure 3.5). To bring further experimental evidence of force redirection, and gain insight on the relation between bundle force and length, we turned to traction force microscopy analysis. For this purpose, cells were seeded on polyacrylamide gels of controlled stiffness. Fluorescent beads were embedded in the gel below the surface, so that tracking their displacements allowed to reconstruct cellular forces (see sections 2.2.2 and 2.3.2 for details on the patterning protocol and on the force reconstruction).

The experiments presented in the previous section were done on glass substrates, i.e. infinitely rigid for the cell. Since cells usually develop higher forces on more rigid substrates, one could expect that these acto-myosin bridges are solely found on rigid substrates. However, we found that on polyacrylamide gels, bridges also formed over non-adhesive gaps. One explanation is that the amount of traction stress developed on substrates of different rigidities is not monotonous but rather saturates above ≈ 20kPa [Yip et al., 2013]. Furthermore, the stability of clusters of adhesion proteins also varies with substrate stiffness [Chan and Odde, 2008, Bangasser et al., 2013, Walcott et al., 2011]. We therefore continued investigating the relationship between bundle tension and bundle length on soft substrates, of rigidity between 8kPa to 16kPa, which has been shown to be optimal for fibroblasts [Stricker et al., 2011, Oakes et al., 2012].

3.2.1 Force distribution on discrete adhesive patterns

Tangential orientation of forces at the cell periphery

We measured cell traction forces on patterned substrates displaying non-adhesive gaps of various widths and compared force orientations near gaps with those on homogeneous substrates. We found that traction stresses are exerted at the periphery of the cell, and with greater amplitudes near acute corners imposed by the patterning geometry. This is consistent with other traction force experiments on patterned substrates [Han et al., 2012, Parker et al., 2002, Rape et al., 2011]. In addition, we found that tangential actin-myosin bundles do redirect traction forces. Despite some contribution of the radial forces from dorsal stress fibers and transverse arcs, the orientation of traction stress vectors originating from the peripheral bundles was clearly tangential to the leading edge. The same conclusion is reached by looking at the deformation of the pattern before and after the cell was detached or as the cell spreads (Figures 3.11 and 3.12).

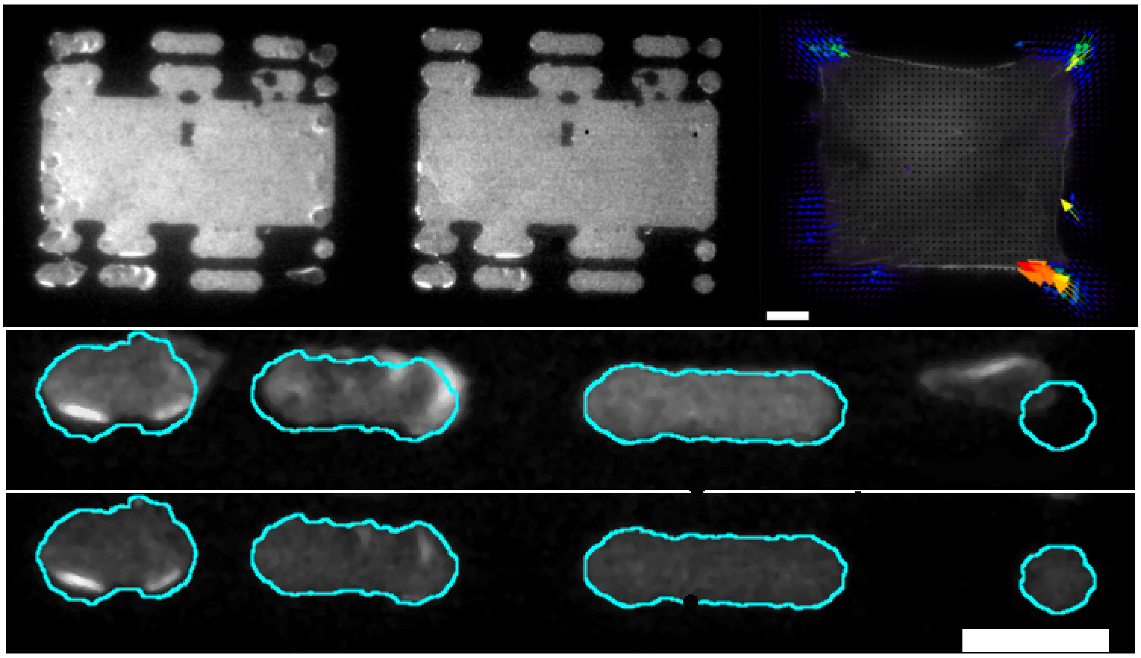

Figure 3.11: Substrate deformation under traction forces. The pattern before (left) and after (center) detaching the cell. Actin (LifeAct transfection) with the overlay of traction forces. Colormap goes from low stress (blue) to high stress (red). Max stress is 2500Pa. Scale bar, 10µm. In the second and third row a zoom on the bottom part of the pattern is shown, the unstrained configuration shown in cyan. In most cases the tangential forces are small, leading to a limited deformation of the adhesive islands in the tangential direction. In one case here (bottom right island), a high stress leads to an important tangential displacement. Scale bar, 10µm.

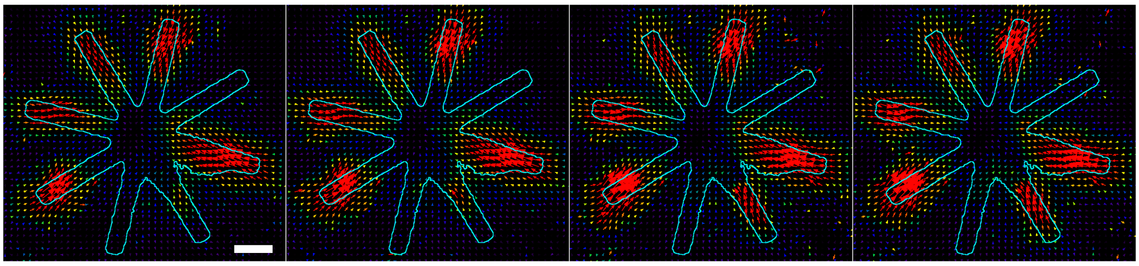

Figure 3.12: Traction stresses of SCF on a star-shaped patterns (shown in cyan). The time interval between each panel is 10 minutes. Notice the increasing traction force on the bottom right branch, where a new peripheral arc is formed. This deviates the forces on the neighboring branch. Scale bar, 10µm.

Scaling of bundle tension with spanning distance between adhesions

When two peripheral arcs on either side of an adhesive branch were anchored at a unique focal adhesion, and no dorsal stress fiber was attached so the LM/LP interface was clearly delimited, it was possible to estimate the bundle tension from the total force exerted on the adhesion and the angle the bundle made with the direction of the force (explained on Figure 3.13). For this, we considered that the traction force transmitted to the adhesions was the vectorial sum of the force from each bundle:

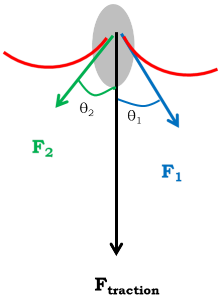

$$\mathbf{F_i} = \frac{|\sin(\theta_j)|}{\sin(\theta_1 - \theta_2)} \mathbf{F_{traction}}$$

Figure 3.13: Projection of bundle tensions into traction force on the adhesion (gray ellipse)

For each bundle, two estimates of the tension were obtained, one from each flanking adhesion, and bundle tension was taken as an average of those two values. Results are plotted in Figure 3.14. A weak increase of force with spanning distance is observed on the grouped data (red squares). Several reasons may explain why no more significant increase is observed. First of all, on the soft patterned substrates used, no bundles small enough were detected to estimate the force from bundles around the maturation threshold. Thus our data could reflect a saturation of force with greater bundle length, which is not contradictory with the existence of a force threshold at shorter distances. Second of all, the method for estimating bundle tension based on decomposing the traction force vector into two components ignores any other contribution to the traction force. Undetected radial stress fibers could lead to overestimation of bundle tension. A second measure of bundle tension is here necessary to confirm or infirm the increase of force with bundle length.

Scaling of bundle radius with spanning distance between adhesions

One indication of bundle tension is given by their curvature radius. Peripheral bundle shape indeed reflects the balance of bundle line tension and of the bulk surface tension (i.e. the myosin centripetal forces). This can be expressed in the form of a 2-dimensional equivalent of the Laplace law which gives the radius of bubbles in function of pressure difference. The relation between radius and tension comes from a minimization of energy,

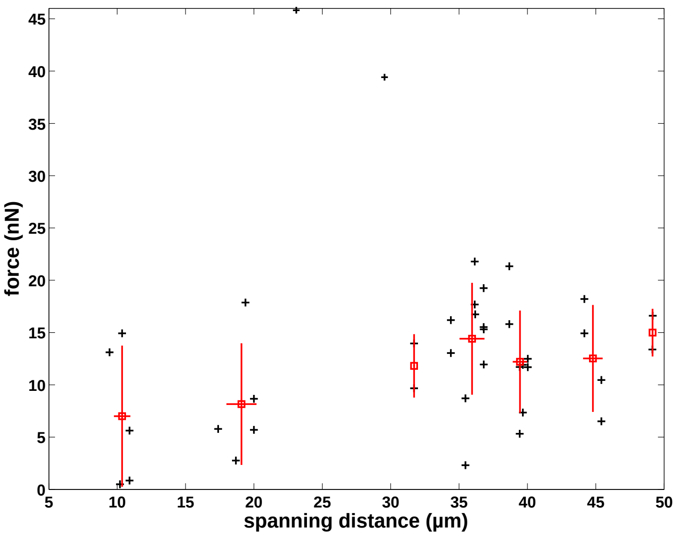

Figure 3.14: Bundle tension versus spanning distance. Data points are in black and grouped averaged in red. Grouped averages were done on interval of 4.1μm intervals, excluding the outliers with very high force.

such that the radius is given by the ratio of the line tension λ and the surface tension σ: $R = \lambda/\sigma$ (see details in section 1.5 and sketch in Figure 3.15). Thus, for a given bulk contractility level σ, bundle radius gives information on bundle tension. In Figure 3.16, we show how bundle radius scales with spanning distance. Cells on both rigid and soft substrates are plotted together. From this graph, we notice that bundle radius increases more than what would be imposed by geometry (i.e. $R \geq d/2$), bringing further support to the hypothesis of a greater tension in longer bundles.

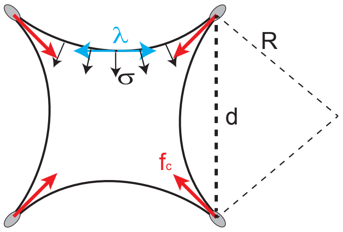

Figure 3.15: Sketch of the equilibrium between line and surface tension determining arc radius and illustrating the Laplace Law $R = \lambda/\sigma$. f_c is here the total force at adhesions.

3.2.2 A contour model to describe how forces depend on geometry

Constant tension model

The Laplace law relating bundle radius to cell tension has been further used in several models for predicting cell shape on patterned susbtrates. For instance, Bischofs et al. [2008;

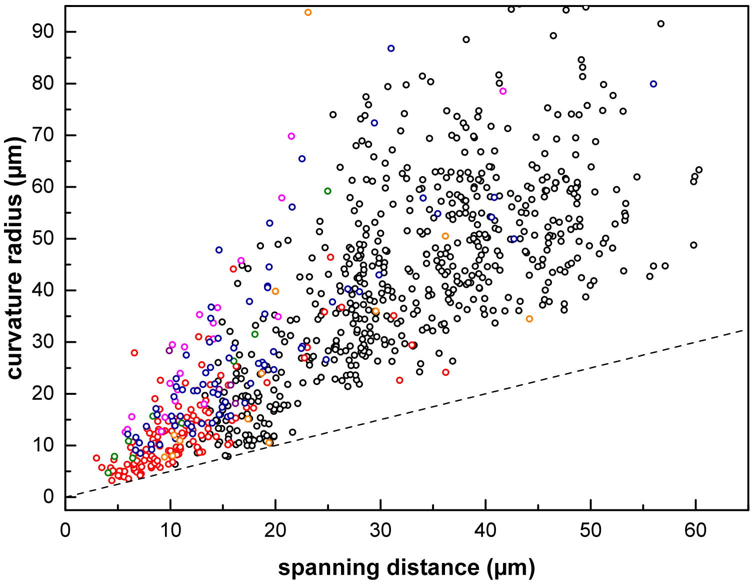

Figure 3.16: Scaling of bundle radius with spanning distance. REF and SCF were seeded on patterned substrates, both rigid (glass) or soft (PAA gels). Each color corresponds to a different batch of experiments. Bundle radius were measured using custom scripts (details given in section 2.5.1). The dashed line corresponds to the geometrical limit or $2R = d$, which is the case where the bundle forms a half circle, d is thus the diameter.

2009] proposed to consider a cell as a 2-dimensional thin sheet with an elastic contour pinned down at its corners so that the free edges take a circular shape. The line tension at the bundle extremity creates a force at the pinning sites (adhesions). The contour bending energy is not taken into account here, since its contribution is minimal (Banerjee and Giomi [2013] treat the case of non-uniform curvatures taking bending elasticity into account and find a wide variety of shapes including convex edges and cusps at adhesions). No specific molecular components are considered here. This conceptualization of the cell is another possible approach to explain the tension in bundles forming between distance adhesions, since the geometry here also leads to a length dependence in the expression of the traction forces at the cell corners.

To express this dependence of forces at adhesions, we consider a polygonal cell, with adhesion sites (pinning) reduced to single points. The force at adhesions is the sum of the contributions from bundles on each side (Figures 3.13 and 3.15). Therefore, the local angle ϕ between each bundle (determined by the spanning distance and the bundle radii) also modulates the effective adhesive force. A constant tension in the arc gives a weak dependence of force on distance, due to the modified angle of bundles at the pinning points (assuming the arc radius does not change). This is given in Bischofs et al. [2009] by

$$F = \sigma d \sin(\phi/2) + 2\lambda\sqrt{1 - \left(\frac{d}{2R}\right)^2}\cos(\phi/2) \tag{3.1}$$

The pinning points at the substrate have in principle some stiffness, accounting for the stiffness of the substrate and of the many molecular bonds participating in the cell-ECM adhesion scaffold. This has been considered by adding a spring at the pinning points in the contour model [Bischofs et al., 2009]. Taking substrate stiffness into account does not change the overall trend, but reduces the magnitude of the force on the substrate. The force at adhesions now writes:

$$F = \frac{\sigma d \gamma_\phi + 2\lambda\cos(\phi/2)\sqrt{\gamma_{phi}^2 + \cos(\phi/2)^2 - \left(\frac{d}{2R}\right)^2}}{\gamma_{phi}^2 + \cos(\phi/2)^2} \tag{3.2}$$

Here $\gamma_\phi = \sin(\phi/2) + \frac{2\sigma}{K}\cos(\phi/2)$ is a normalized constant. Some examples of how the force would vary with the bridge spanning distance are given in Figure 3.17 for two different opening angles, $\phi = \pi/2$ and $\phi = 3\pi/4$. For the stiffness of the substrate, a value of K=10 pN/µm is taken based on the an estimation given in Walcott et al. [2011] that $K = \frac{2\pi RE}{2\pi RE + 3\kappa}\kappa$, where κ is the stiffness of the molecular bonds, E=10kPa the Young modulus of the substrate and R the radius of cell-ECM bond interaction.

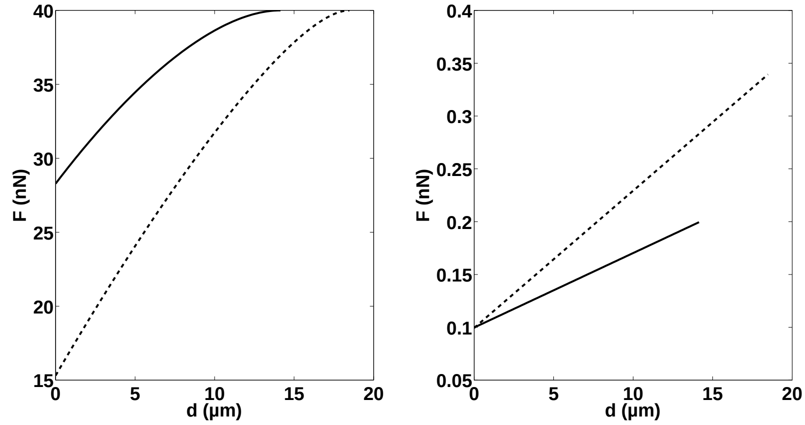

Figure 3.17: Force magnitude versus spanning distance. Plots of eq.(3.1) (left) and eq. (3.2) (right) for a 4-branched (solid line, $\phi = \pi/2$) and 8-branched (dashed line, $\phi = 3\pi/4$) polygonal cell. λ=20nN, σ=2nN/µm and K_{ext}=10pN/µm.

Elastic tension model

This model can be improved, by introducing an explicit dependence of force on spanning distances. To do so, the assumption of a constant line tension is dropped, to consider an elastic line tension instead, where λ depends on bundle strain. The increase of force with spanning distance would here be amplified, at least for a given bundle rest-length. Note that in this case again, substrate stiffness has little influence on the overall trend. The elastic tension model is explored in greater details in Chapter 4.

3.3 Discussion

We have presented evidence of a length-dependent cytoskeleton reorganization from meshwork arrangement to bundled arrangement. Above a length threshold, thick peripheral bundles form and become stably anchored to focal adhesions through the conversion of radial myosin forces to tangential forces at the terminating adhesions. We have then presented experimental measurements of such forces and a possible physical mechanism explaining that the tangential forces weakly increase with bridge spanning distance. The mechanism presented here relies on the fact that the maturation of focal adhesions is force-dependent. The mechanosensory properties of adhesions would thus participate in controlling the length maturation threshold.

Rationale for a force threshold

The hypothesis of a local force threshold at adhesions is based on evidence that the dynamics of focal adhesions rely on force-sensitive processes, such as the load-dependent binding and unbinding rates of adhesion proteins or the stretching of molecules [Wolfenson et al., 2011]. Force may have two effects, either destabilizing integrin-ECM bonds, or increasing the number of bonds by opening access to new binding sites. These two competitive effects as well as collective effects in clusters of integrins lead to the existence of an optimal range of forces for adhesion stabilization [Schwarz et al., 2006, Nicolas et al., 2004; 2008]. Schwarz et al. [2006] mention a threshold of 9pN per $\alpha_5\beta_1$ integrin (catch-bond type). Whether these are valid at the scale of large focal adhesions terminating actin bridges is uncertain, but the principle of force-dependent growth and stabilization of focal adhesions is now well-established (reviewed for instance in Parsons et al. [2010]).

Shemesh et al. [2009] provide an alternative explanation for why concave interfaces form at the rear of the lamellipodium. They found that the formation of a LP/LM interface depends on force and distance between adhesions, though they use a different argument, namely that the actin gel disintegrates above a given stress threshold. Here the limiting factor is the stress in the gel between the adhesions, rather than the force at the adhesion sites. Their numerical simulations yield similar morphologies of the cell's leading edge as what we have found and a prediction that higher force is needed to create a stable interface between focal adhesions that are more spaced. However, they consider only the particular case that of a forward moving interface in migrating cells, and not that of a static leading edge as we have observed on the patterned substrates (Figure 3.6), nor the formation of concave peripheral bridges above non-adhesive gaps. We thus argue that the LTM and force-dependent stabilization of focal adhesions are necessary to explain the prolonged stability of peripheral bundles on patterned substrates.

Conclusion

In this chapter, we have analyzed the dependence of cell shape and cytoskeleton organization on adhesive geometry. The hypothesis of a *length maturation threshold* had been posited in Loosli et al. [2012], and we here provide experimental evidence that there is behavioral switch above which a transition from mesh-like cytoskeletal organization to bundled cytoskeletal organization is observed. The peripheral bundles bridging the gaps are stably anchored at the terminating focal adhesions. We estimate the threshold length to be around 3μm to 4μm for SCF and 3T3 fibroblasts respectively. Our observations are consistent with a myosin-dependent mechanism converting normal centripetal load to tangential forces. We measured a weak dependence of force magnitude on actin bundle length in fibroblasts using traction force microscopy experiments, and a similar trend of bundle radius with bundle spanning distance. We then discussed the theoretical basis for a geometrical dependence of force at adhesions and use a contour model to explain a possible dependence of force with bridge spanning distance. We purposefully kept a simple model of SF, and did not consider a possible reinforcement of bundle along its length by recruitment of crosslinkers, though this could possibly also play a role in the tension building of long peripheral fibers. To gain further insight into how tension and shape are tightly regulated inside cells, it is necessary to better understand how bundle tension depends on myosin activity or on other components. This is the purpose of the next chapter.

Chapter 4

Cell shape dynamics reveal balance of elasticity and contractility in peripheral arcs[1]

The organization of the actin-myosin II system is known to be strongly influenced by the configuration of the adhesive substrate, as is exemplified by the results of Chapter 3, showing how the formation of concave stress fibers can be finely controlled by discrete adhesive geometries (also observed in Théry et al. [2006a], Rossier et al. [2010] and Vianay et al. [2010]). The orientation and tension within these peripheral fibers are important for many cellular processes, even more so because of their anchorage to focal adhesions, which are central to cell-substrate interactions and are hubs of biochemical signaling [Geiger et al., 2009, Schwarz and Gardel, 2012]. In particular, peripheral fiber tension is expected to be transduced through these adhesions into traction forces onto the substrate, which can direct subsequent cell spreading, migration or polarization.

Given the tight coupling between cell shape and mechanical tension [Rape et al., 2011, Zemel et al., 2010a, Lecuit and Lenne, 2007, Chicurel et al., 1998], several studies have dealt specifically with how the curvature of peripheral arcs arises from their mechanical properties, using either analysis of cell shape [Théry et al., 2006a, Bischofs et al., 2008, Deguchi et al., 2011], or analysis of both shape and traction forces [Bischofs et al., 2009, Lemmon and Romer, 2010]. The simplest way to explain the inward curvature of an arc is to use the contour model introduced in section 3.2.1 and Figure 3.15, in which the line tension λ in the arc is balanced by the surface tension σ coming from the cell bulk and by adhesive forces at the corners where the arcs are anchored to focal adhesions [Bischofs et al., 2009]. At equilibrium, the radius R of an arc along its free length is thus $R = \lambda/\sigma$. However, the nature of both the surface tension and the line tension in the arc is not fully understood. It has been argued that the surface tension comes both from the actin-myosin contractility in the cytoskeletal cortex and from the cell membrane; but the magnitude of membrane tension is estimated to be one order of magnitude lower than cortical tension, so the surface tension is expected to be defined by cortical tension [Gauthier et al., 2012, Clark and Paluch, 2011]. The nature of the line tension has been subject to debate: it is generally assumed that it is dependent on myosin-driven contractility, but it is unclear if elasticity contributes to tension [Bischofs et al., 2008; 2009, Guthardt Torres et al., 2012, Banerjee and Giomi, 2013]. It remains to be established how myosin activity affects the mechanical behavior and shape of peripheral arcs.

---

[1] Results of Chapter 4 are published in Labouesse et al. [2015]

In order to elucidate the contribution of myosin-dependent contractility, we study how the coupling between cell shape and cell tension is modified by altered myosin activity. Previous works reported that myosin inhibition often leads to a loss of a coherent cell shape, with the appearance of large invaginations in the cytoplasm and uncontrolled protrusive behavior [Lacayo et al., 2007, Cai et al., 2010]. To avoid this and to obtain a reproducible cell shape while modifying myosin activity, we use adhesive patterning and low concentrations of drugs. We simultaneously measure cell shape, traction forces, and tension in the arcs at various contractility levels in these defined geometries and compare the experimental results with simulations based on different hypotheses about the nature of line tension. Our results help to establish the roles of myosin-dependent contractility and passive elasticity in arc tension and shape.

4.1 Methods

4.1.1 Traction force microscopy

The results presented in this chapter are based on traction force microscopy experiments described in Chapter 2, section 2.3.2. In the analysis presented in this chapter, the total traction force exerted by a cell was computed by integrating all traction stresses under the cell's effective adhesive area. Since marking focal adhesions was not possible, the effective adhesive area was determined by setting a threshold on the traction stresses. Note that the stress footprint under which traction forces are integrated may be larger than the real focal adhesion area, because of the force reconstruction method chosen (FTTC) [Stricker et al., 2010]. TFM was performed under myosin inhibition, using 50μM blebbistatin and 10μM Y27632 diluted in the imaging medium.

4.1.2 Cantilever-based measurements of fiber tension

Fiber tension was measured during myosin inhibition with custom-made SU-8 ultra-soft cantilevers. Details on the fabrication and properties of the cantilevers are given in Chapter 2, section 2.4.2. We here briefly describe the protocol used for tension measurement, which is also detailed in Piacentini et al. [2014]. Cells were seeded on cross-shaped 3D PDMS patterns with fibronectin coated on the top. Two types of cantilevers were used: 5µm x 5µm x 700µm and 5µm x 10µm x 700µm. Their corresponding spring constants were 2.28nN/µm and 4.56nN/µm. Cycles of 4 radial compressions of increasing depth were applied to the peripheral arcs with a cantilever, at a speed of 5µm/s. Such cycles were performed several times before adding the drug and every 4 to 5 min during drug incubation. It was assumed that bundle tension remained constant during one compression cycle, which is justified by the short duration of the compression cycle (2.5 min) with respect to the time of drug treatment (30 min) and the fact that bundle length did not change significantly (less than 2%), due to the compression. Additionally, we verified that compression did not induce significant changes in cell morphology, in particular, that the attachment sites of the peripheral bundles to the adhesive pattern did not shift. R, d and initial bundle-cantilever distance were thus measured once before each cycle. At each compression, the deflection of the cantilever and the indentation of the bundle e were measured, and from this, the force on the cantilever F_c and the bundle deflection angle γ were computed. The deflection angle is given from geometrical arguments by (4.1) which are sketched in Figure 4.1. For small indentations, the force increases linearly with the deflection angle $F_c = 2T \sin\gamma$. For each cycle of compressions, bundle tension T was then measured from the slope of the force-deflection angle curves.

$$\sin\gamma = (x_0 + e)\sqrt{\frac{1}{d^2/4 + (x_0+e)^2} - \left(\frac{1}{2R}\right)^2} - \frac{d}{4R} \tag{4.1}$$

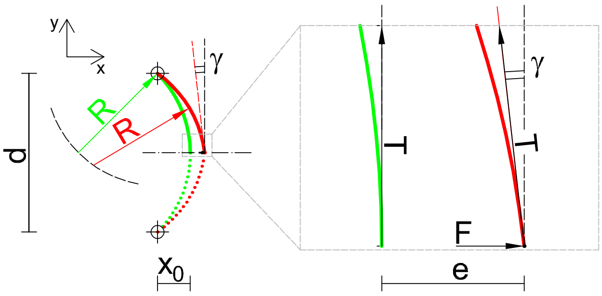

Figure 4.1: Illustration of the geometrical variables leading to the tension-indentation relation. R is the arc radius, x_0 the arc height, d the spanning distance, γ the deflection angle, e the bundle indentation. Adapted from Piacentini et al. [2014].

4.2 Experimental results

4.2.1 Shape response to myosin inhibition

Molecular composition of peripheral arcs

We have discussed in Chapter 3 how fibroblasts create thick arc-shaped actin bundles at the cell edge to bridge non-adhesive gaps, with a radius of curvature determined by the ratio of line tension to surface tension. Line tension could result from myosin activity, passive elasticity, or a combination of the two [Bischofs et al., 2008; 2009, Guthardt Torres et al., 2012], and this should be reflected in the molecular composition of the arcs. We have shown that the arcs are densely cross-linked by both α-actinin and myosin II, which overlap in multiple zones (Figure 3.4). The presence of both active and passive cross-linkers thus suggests that the peripheral arcs can develop active and/or elastic tension, as is argued in Yoshinaga and Marcq [2012].

Cell swelling as a result of myosin inhibition

We first looked at how cell shape changed in response to contractility inhibiting drugs, for cells spread on patterned soft polyacrylamide gels as well as on rigid glass substrates. We used either one of the two drugs: Y27632, a ROCK inhibitor reducing myosin light chain (MLC) phosphorylation levels, or blebbistatin, inhibiting the motor activity of myosin II. Upon treatment with either 10µM Y27632 or 50µM blebbistatin we observed two distinct behaviors. In a minority of cells, there was a loss of cell coherence resulting in a shrinkage of the cell body and a massive extension of protrusions creating many concavities and irregularities in the cell shape [Lacayo et al., 2007, Cai et al., 2010, Senju and Miyata, 2009]. However, in the vast majority of cells, cytoplasmic coherence was maintained, with increased radii of curvature of the arcs, resulting in an overall increase of the cell area (Table 4.1 and Figure 4.2). This response was predominant on both soft and rigid substrates. Cells having reached the end of the pattern branches, the only possible gain in area came from the non-adhesive zones. However, cell area increase was not always isotropic. The 4 peripheral arcs present on each cross-shaped pattern did not systematically have the same response. In some cases, the radius of one arc decreased, while the others increased. Therefore, cell area is a better indicator of the overall cell response than the behavior of individual arcs. The numbers of cells that increased their area for the different substrates and drugs are summarized in Table 4.1. Overall, area increase was observed in over 86% of cells.

	Number of cells with area increase	Quantitative response			
		t_0+10min		t_0+30 min	
		$(A - A_0)/A_0$	$(F - F_0)/F_0$	$(A - A_0)/A_0$	$(F - F_0)/F_0$
10µM Y27632	57 out of 63	+17%	-35%	+32%	-50%
50µM blebbistatin	16 out of 22	+3%	-52%	+5%	-83%

Table 4.1: Quantification of cell response to myosin inhibition. The first column gives the total number of cells for which an area increase was observed in response to myosin inhibition, irrespective of the substrate (glass or PAA gel). The second column gives the percentages of change in area and force magnitude after 10 min and 30 min of drug incubation for cells on PAA gels, as plotted in Figure 4.3.

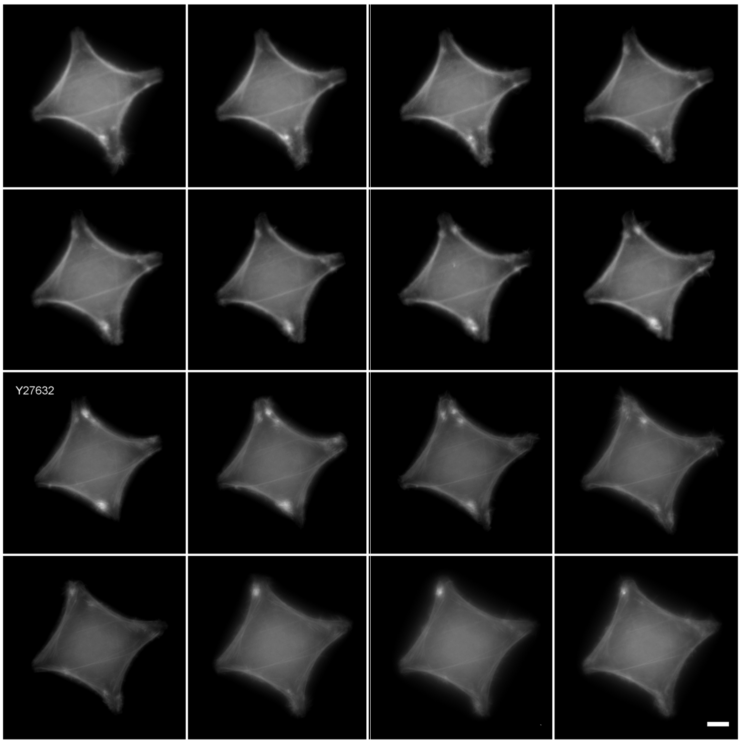

Figure 4.2: Dynamic cellular response to Y27632 treatment. REF 52 cell transfected with LifeAct EGFP on a cross-shaped pattern, imaged for 15 minutes before and 15 minutes after Y27632 addition. Time interval between each panel is 2 minutes; the drug addition time indicated on panel 9. Scale bar, 10µm.

4.2.2 Fiber tension measurement

Dynamics of line and surface tension from traction force microscopy data

Simultaneously to monitoring cell shape, we performed traction force microscopy (TFM) on the patterned polyacrylamide gels to follow the evolution of cell force during contractility inhibition. Full-spread cells were imaged for 20 minutes in control conditions, before adding a contractility inhibiting drug. Inhibiting myosin activity resulted in a drop of traction force magnitude, as was expected and previously reported [Tseng et al., 2011, Aratyn-Schaus et al., 2011, Oakes et al., 2012]. Figure 4.3A illustrates this response, showing the shape and traction stresses for one representative cell before myosin inhibition (on the left) and after 30 min of Y27632 treatment (on the right).

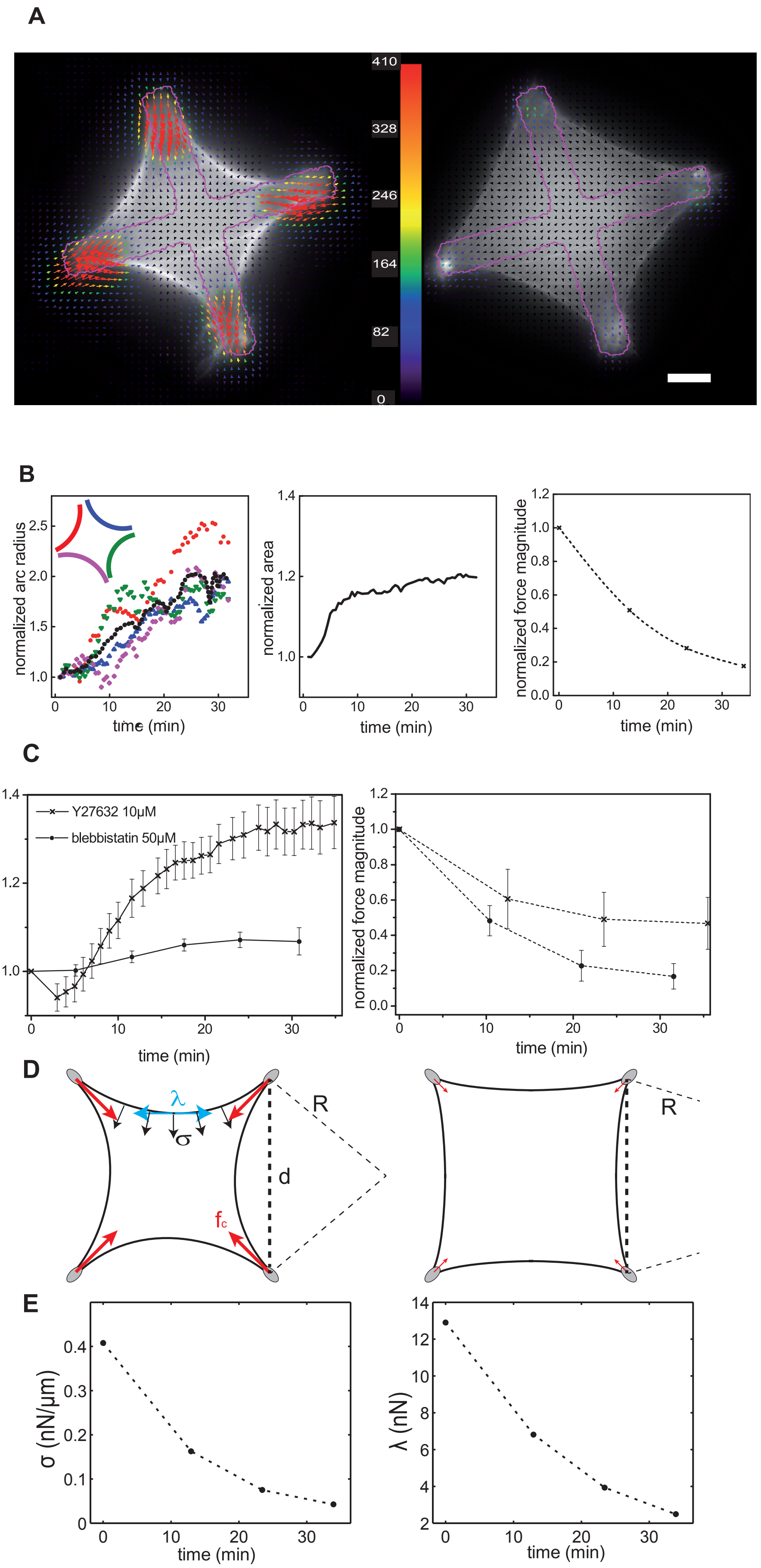

Figure 4.3: Shape and tension response to myosin inhibition (legend on next page)

Figure 4.3: Shape and tension response to myosin inhibition of a REF52 cell on a cross-shaped pattern. A) F-actin and traction stress vectors before myosin inhibition (left) and after 30 minutes incubation with Y27632 at 10µM (right) showing the cell area increase. F-actin was labeled using LifeAct EGFP. Traction stress vectors are indicated by colored arrows (color scale in Pa). Maximum stress is 1020Pa (before inhibition) and 180Pa (after inhibition). Color bar is linear up to 410Pa, all higher stresses are shown in red arrows. Adhesive pattern contour is indicated with a magenta overlay. Scale bar, 10µm. B) Plots of radius (left), area (center) and total force magnitude (right) over time of Y27632 incubation for the cell shown in (A); all are normalized to their initial values. In the left panel, the evolutions of each bundle radius (scatter, with the color coding indicated in inset) and of the mean radius (black dots) are given. C) Mean normalized area (left) and mean normalized force (right) for cells on PAA gels. 'x' indicate Y27632-treated cells (n = 18), and 'o', blebbistatin-treated cells (n = 8). Bars are the standard error of the mean. After 30 minutes of incubation, the drug was washed out with normal imaging medium. D) Sketch of a cell on a cross-shape pattern under control conditions (left) and contractility inhibited conditions (right). The line tension λ (cyan), surface tension σ (black) and force at adhesions f_c (red) are depicted, as well as the spanning distance d and arc radius R. E) Surface tension (left) and line tension (right) calculated for the cell shown in A,B,C from eqs. (4.2)-(4.3).

For this cell, the mean radius increased linearly to twice its initial value, corresponding to a 20% increase in area, while the total force magnitude dropped below 20% of its initial value during the 30 min of myosin inhibition, as shown in Figure 4.3B. The evolution of area and traction force magnitude averaged over all cells showed similar trends (Figure 4.3C and Table 1), setting aside the small initial dip in cell area, coming from a fast initial contraction of some cells likely due to a transient liquid flow when the drug was added. After washing out the drug with normal medium, traction forces were observed to grow again, confirming that the observed lower contractility state is due to myosin inhibition. Comparing the two myosin inhibitors, we observed that blebbistatin and Y27632 had similar effects on cells, both leading to decreased traction forces and increased radii, though the changes were different in magnitude (see discussion in section 4.4 for possible reasons).

We next investigated how the Laplace equilibrium (4.2) was shifted by myosin inhibition (Figure 4.3D).

$$R = \lambda/\sigma \tag{4.2}$$

We assume the line tension λ to be homogeneous within one arc, and the surface tension σ, normal to the cell edge, to be also homogeneous within the cell. In contractility inhibiting conditions both surface tension and line tension are likely to decrease. However, the increase in the radius of curvature could happen only if the surface and line tension do not change in the same manner, e.g. if the surface tension drops while the line tension stays constant, or the surface tension drops faster than the line tension. We set out to find in which proportions surface tension and line tension respond to myosin inhibition.

The experimental measurements of the traction forces and of the curvature radii are in principle sufficient to infer the evolution of line and surface tensions: by considering a cell attached to the substrate at its four corners, the forces at adhesions can be expressed as a function of geometrical parameters and of the line tension [Bischofs et al., 2009]. We assume that the cell has a 4-fold symmetry (i.e. 4 arcs having the same curvature and same line tension, and a uniform spanning distance between the adhesions, see Figure S1) and that the traction forces are exerted at the tips of the adhesive branches, with equal magnitude f_c at the four cell “corners”. Together with eq. (4.2), this simplification allows to calculate unique values of λ and σ for each cell from the knowledge of the spanning distance d, the mean radius of the arcs R, and the traction force magnitude $F = 4f_c$ exerted by the cell (illustrated in Figure 4.3D):

$$\sigma = \frac{F}{2\sqrt{2}(d + 2R\sqrt{1 - d^2/4R^2})} \tag{4.3}$$

Our measurements showed that both line and surface tension decreased during contractility inhibition, but the drop of surface tension was more pronounced than that of line tension (Figure 4.3E): with 5-fold decrease in the traction force and a 1.5-fold increase in the arc radius, eq. (4.2) - (4.3) give approximately 7-fold decrease of surface tension and 4.5-fold decrease of the line tension. The decay of both λ and σ is consistent with the hypothesis that both depend on myosin activity, albeit in a different manner.

Cell response to an increase of contractility

Although the analysis presented here, and the numerical model developed in the next section focuses on inhibition of myosin, we were curious how cells would respond to an increase of contractility. We thus performed the opposite perturbation where contractility was enhanced using calyculin A (5nM). Calyculin A inhibits the Myosin Light Chain Phosphatase (MLCP) pathway, thus increasing the fraction of phosphorylated (i.e. active) myosin motors. In many cases, this led to such an abrupt increase in contractility that the whole cell body shrunk. In rare cases though, peripheral arcs remained intact, and were observed to be pulled inward (Figure 4.4). Similar to the case of myosin inhibition, this decrease of arc radius can be explained using the Laplace equilibrium model (eq. (4.2)) by an increase of surface tension in higher proportion than line tension.

Cantilever-based measurements of line tension

To confirm the estimations of λ and σ from TFM experiments, we measured line tension using an alternative protocol presented in Piacentini et al. [2014]. We applied small radial deformations to the peripheral arcs with ultra-soft cantilevers, of spring constants of 2.3 and 4.6nN/µm, but the results are independent of the cantilever spring constant. The increase of fiber indentation with the cantilever displacement depends on the tension within the fiber, yielding λ (see section 2.4.2 and [Piacentini et al., 2014] for details). This was

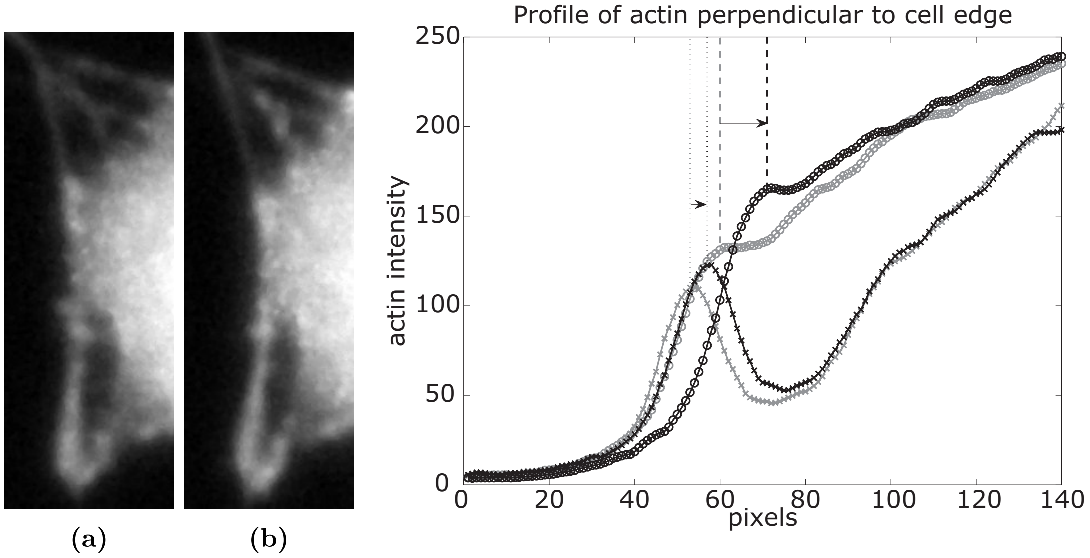

(a) (b)

(c)

Figure 4.4: Calyculin A treatment pulls fiber inward. Close up on a peripheral fiber before (a) and after (b) treatment with cayculin A. The cell was transfected with LifeAct EGFP. (c) Inward pull of fiber with increase of surface tension. In this cell, the cytoplasm became detached from the fiber extremities before calyculin A was added. Upon addition of the drug, the fiber was pulled inward in its center, where it had remained attached to the cytoplasm. This is shown here: profiles perpendicular to the cell edge at the center (o) and at the extremity (x) of the fiber are given before (gray) and after (black) treatment with 5nM of calyculin A. The dotted and dashed lines indicate the inward pull of the fiber of ≈1µm at the center and 0.4µm at the extremity respectively.

done on a different substrate than TFM experiments (rigid PDMS 3D-patterns, Young modulus $E \sim$ 2MPa) incompatible with traction force measurements. ROCK inhibitor Y27632 was applied in the same conditions as previously, resulting in a drop of fiber tension. Note that in this case a minor retraction of the arcs was observed, possibly due to repetitive mechanical perturbation. We observed a close-to-linear decrease of λ in time (Figure 4.5), confirming that line tension depends on myosin activity. Typically λ decayed by 2.5% per minute ($R^2 = 0.77$). We can use the values of λ and of the radii of curvature R to infer σ from eq. (4.2), yielding values of initial surface tension between 0.1nN/µm and 2.3nN/µm, in the same range as what was extrapolated from TFM experiments (see Figure 4.7 and Table 4.2). These independent measurements validate our initial estimations of the decay of λ.

4.2.3 Comparison of line tension measurement techniques

We presented above two independent measurements of the line tension under myosin inhibition. The cantilever-based experiments gave a direct estimate, while on PAA gels λ was interpolated from R and F. The magnitudes of the drop in tension during the 30 minutes of drug incubation are similar, down to 20%–40% of the initial tension on

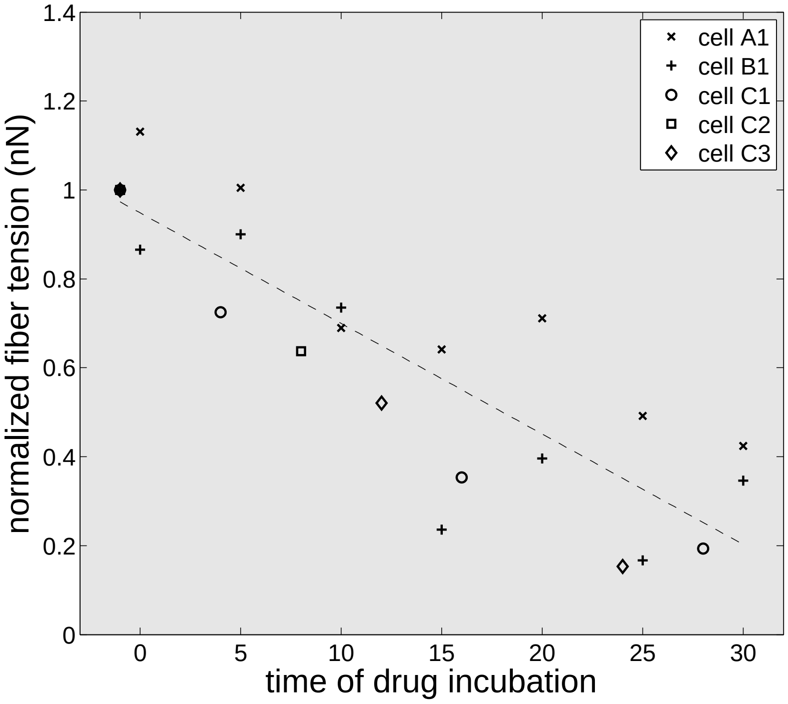

Figure 4.5: Fiber tension measurement with ultra-soft cantilevers during Y27632 treatment. Each marker denotes a different cell. The values were normalized by the value of tension before addition of the drug (average of several points). Dotted line is a linear fit to all the data grouped together: $y = -0.025x + 0.95$ ($R^2 = 0.77$). Cells A1 and B1 were indented with a 5µm x 5µm x 700µm cantilever (k = 2.28nN/µm), cells C1-C3 were indented with a 5µm x 10µm x 700µm cantilever (k = 4.56nN/µm).

the PDMS substrates, and to 10%–20% on the PAA gels. These correspond to initial fiber tensions distributed between 60nN and 150nN on the PDMS substrates, and 12nN and 85nN on PAA gels; they then fall to 20nN – 60nN, and 1nN – 10nN, respectively. The same trend is observed for the surface tension, which is two times higher on PDMS than on PAA gels (1.1nN/µm compared to 0.67nN/µm). Both values corroborate existing estimates [Bischofs et al., 2008, Piacentini et al., 2014]. The higher amplitude of λ and σ on the PDMS substrates may be explained by the substrate rigidity which is 200 times greater than the PAA rigidity ($\sim$ 2MPa compared to 10kPa), as cells develop more force on more rigid substrates [Schwarz et al., 2006, Marcq et al., 2011]. The values of line tension determined here are higher than what is for instance reported in Albert and Schwarz [2014] where the total line tension was found at about 5.5nN. However, this value was obtained from MCF10A cells, which are less contractile than REF cells. We also found substrate-dependent differences in the rate of λ decrease. On PDMS tension loss was nearly linear, whereas it appeared exponential on PAA gels. This apparent difference may be due to a difference in time scale ($\tau \sim 10$ min or $\tau > 30$ min, where τ is the characteristic decay time of σ). Note that since the line tension was measured every 4 to 5 minutes on the PDMS substrates, and every 10 minutes on the PAA gels, the time-scale estimations are only order of magnitudes. One factor that could explain these small differences is the repeated indentations. In the cantilever-based experiments, the fiber was mechanically perturbed several times, which could cause higher values of λ over time.

4.3 Model of elastic contractile arcs

4.3.1 Description of the elastic contractile bundle model

The experimental results presented above show that both the surface tension and the line tension decay as myosin activity decrease, but to different extents. It was reported that ROCK controls myosin light chain phosphorylation locally in the centre of the cell [Kolega, 2003], but given that blebbistatin and ROCK inhibitor Y27632 produce qualitatively similar effects, different responses of λ and σ are not likely to stem from a localized action of ROCK. We checked how the distribution of phosphorylated myosin in cells was affected by the inhibitors. Figure 4.6 shows staining for actin and phosphorylated myosin light chain (pMLC). In all cells, myosin remained colocalized with actin bundles. In blebbistatin-treated cells, there are still high levels of pMLC. That was expected, since blebbistatin does not affect light chain phosphorylation, but rather freezes myosin in a weakly bound state. In Y27632-treated cells, the level of pMLC had greatly decreased both in the arcs and the bulk of the cell. Therefore, the action of Y27632 was not spatially limited to the center of the cell.

We assume that both Y27632 and blebbistatin act by limiting the number of active motors, in function of the drug concentration, thus reducing the myosin-dependent contractility both in the peripheral arcs and the bulk of the cell; then a lesser effect of myosin inhibition on the line tension could be explained by the existence of a myosin-independent component in the line tension. In previous theoretical works line tension in stress fibers has been considered to be solely active, i.e. myosin-dependent but strain-independent [Lenz et al., 2012, Kaunas et al., 2010], solely elastic, i.e. dependent linearly on strain [Bischofs et al., 2008], or a combination of both [Albert and Schwarz, 2014, Yoshinaga and Marcq, 2012]. As argued above, an entirely active behavior does not account for increasing arc radius: if both line tension and surface tension were directly proportional to the number of motors, the equilibrium radii would not change (following eq. (4.2)), contrary to what has been experimentally observed. On the other hand, an entirely elastic force proportional to bundle strain $\lambda_{el} = \frac{EA}{L_0}(L - L_0)$ could explain the decay of line tension, since an increase in curvature radius would diminish bundle length L (bundle would straighten) and hence

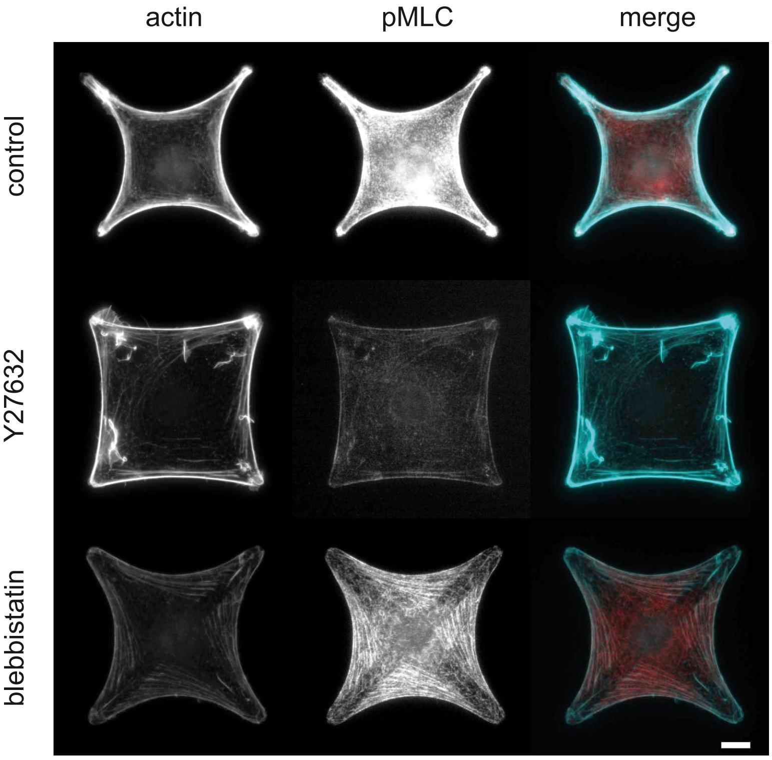

Figure 4.6: Myosin involvement in line and surface tension. A) Immunostaining of cells in control conditions and under Y27632 and blebbistatin treatment. Cells were stained for actin (left), and pMLC (center). Right column shows the merge of actin (cyan) and pMLC (red). Scale bar, 10µm.

the strain. The decrease of line tension would be strongly dependent on how much the bundle length changes.

We propose here to use a general model, associating an active contractility with elasticity in the line tension. We neglect a possible elastic contribution to the surface tension, as has been done in existing cable network models [Bischofs et al., 2008, Guthardt Torres et al., 2012, Paul et al., 2008]. Since the drug response developed over a relatively long time scale (tens of minutes) we assume that the observed states represent mechanical equilibrium with motors working at their stall force, thus the surface tension is directly proportional to the number of active motors, as is also the active part of line tension λ_a. The total line tension is then the sum of the two contributions:

$$\lambda = \lambda_a + \lambda_{el}. \tag{4.4}$$

Two additive components here correspond to a system in which the active and elastic elements are connected in parallel. The myosin-independent elastic term, will dominate once the motors are inhibited, leading to increased radii; as the arcs straighten, the elastic tension will diminish as well. On the other hand, a motor connected in series to an elastic bundle is equivalent to the purely active case, since the total force in this arrangement is equal to the active force developed by motors. Thus a series arrangement cannot explain our observed change of radius. Note that this consideration is not contradictory with the possibility that several contractile units connected in series exist in a fiber; in this case, each unit could have elastic and active elements in parallel. We thus assume such a parallel arrangement, with the line tension being the sum of active and elastic contributions. To determine the elastic contribution, it is necessary to know the rest-length of the bundle. Note that to explain bundle straightening due to elastic tension, the rest length should be smaller than the shortest length measured in the experiments. We notice indeed that even after myosin inhibition there is some remaining tension in the bundle, which can be partly attributed to the elastic tension. Moreover, since actin filaments buckle under compression, negative elastic tension cannot develop. Therefore $L_0 \leq L_{min}$, which in the limiting case of a straight bundle translates to $L_0 \leq d$. In principle, L_0 could be taken strictly smaller than d, which would mean that a straight fiber is tensed independently of myosin activity. However, since numerous studies have attributed the pre-tension of fibers to myosin [Deguchi et al., 2005; 2006, Lu et al., 2008, Deguchi and Sato, 2009], corresponding to our active term λ_a, it is safe to assume that the elastic rest-length is by construction the straight bundle length, here equal to the spanning distance. The rest-length in the model is therefore taken as equal to the spanning distance $L_0 = d$, similarly to Bischofs et al. [2008], Albert and Schwarz [2014]. The bundle stiffness EA (product of Young Modulus E of the bundle by the cross-section A) is assumed to remain constant during myosin inhibition (see discussion in section 4.4):

$$\lambda_{el} = \frac{EA}{d}(L - d) \tag{4.5}$$

Expressing L and λ in terms of d and R, and combining equations (4.2), (4.3) and (4.4) yield an implicit equation for R:

$$R = \frac{\lambda_a}{\sigma} + \frac{EA}{\sigma d}\left(2R \arcsin\left(\frac{d}{2R}\right) - d\right) \tag{4.6}$$

4.3.2 Fitting the model to experimental data

Numerical simulations

We chose to impose an exponential decrease of σ, as was observed in the TFM experiments during myosin inhibition. We then solved eqs. (4.3) and (4.6) for different time-points and compared the evolution of traction force magnitude, radius of curvature, line and surface tensions with the experimental data. Our numerical results reproduced qualitatively the exponential decay of traction forces and the increase in cell area. We next validated this model on a single cell basis. The 10 cells (7 treated with Y27632 and 3 with blebbistatin) that were the most symmetric in shape, and with similar responses of each arc to myosin inhibition were used. For each cell, we searched for the best value of λ_a to fit the evolution of F, R, λ and σ. The steps of this fitting procedure are detailed here.

i) From the force F and radius R measurements, the evolution of λ and σ are computed using eq. (4.2)-(4.3), before and during the drug treatment.

ii) The values at t_0 (before adding the drug) of the traction force magnitude F_0, the initial arc radius R_0 and the spanning distance d are used to set the initial parameters of the model.

iii) The surface tension experimental values are fitted with a simple exponential decay using integrated fitting options (NonLinear Least Squares method).

iv) The characteristic time τ of the surface tension decay is used as the simulation time scale.

v) The simulated surface tension σ/σ_0 is then imposed to follow this exponential decrease in time. Eq. (4.6) is solved for R, at each time points, for different values of the initial ratio $R_a = \lambda_a/\sigma_0$. R_a was incremented by 0.1µm, corresponding to increments in the initial active tension term λ_a of $\sigma_0 \cdot 0.1\mu m$. Since the radius R_0 and force F_0 fix the values of λ_0 at the first time-point, changing λ_a will modulate the bundle stiffness EA so that eq. (4.6) is satisfied at t_0. The higher λ_a, the lower the bundle stiffness. Since R and F change monotonically with λ_a, there is a unique value of λ_a that will yield the correct evolution of R/R_0 and F/F_0. To find the best parameter value, numerical solutions were scored as follows: the root-mean-square error was computed for every experimental point, and a total score was given by aggregating all relative errors (eq. (4.7)). We then chose the parameters giving the minimal error between the predicted R_{num} and F_{num} and the experimental values R_{exp} and F_{exp}.

$$score = \frac{\sqrt{\langle (R_{exp} - R_{num})^2 \rangle}}{R_0} + \frac{\sqrt{\langle (F_{exp} - F_{num})^2 \rangle}}{F_0} \tag{4.7}$$

Results

An example is given in Figure 4.7A for a representative cell (F_0 = 102nN, d = 38.7µm, R_0 = 31.6µm, σ_0 = 0.41nN/µm and λ_0 = 1.9nN, τ = 14 min). The numerical results (solid lines) compare well with the experimental results (circles): the magnitudes and slopes of both R and F (left plot), as well as for the line and surface tensions (right plot) are the same as for the experimental data. The root mean square errors are below 1% for F, λ and σ, and below 8% for R. The results of simulations for 10 different cells, normalized to their initial values, were averaged and are shown in Figure 4.7B. The color bands indicate the standard deviations around the mean values. The good agreement of the numerical results with the experimental observations of Figure 4.3C demonstrates that the superposition of elastic and contractile terms is an accurate description of the tension in peripheral arcs. Dispersion in these results reflects the different ratios of elastic and active contributions from cell to cell, but also partly comes from the variability of initial values: despite standardized adhesion localization imposed by micro-patterning, we observed variability in initial values of F_0 (standard deviation was 80% of mean value) and of R_0 (standard deviation was 30% of mean value).

The values found for the initial active, elastic and total tensions of the 10 cells on PAA gels and 1 cell on a PDMS substrate are plotted in Figure 4.8 and summarized in Table 2. Initial line tension was found to be between 12nN and 130nN. Interestingly, most of the cells displayed one dominant contribution to the line tension, being either mostly active or mostly (or entirely) elastic, suggesting there are two modes for tension build-up in acto-myosin bundles (see discussion 4.4); but in average, the active contribution was of 64% of total line tension. Those cells that had a higher elastic contribution correspond to those that lost less traction forces during contractility inhibition, explaining why in average, forces dropped only 50% in Y27632 treated cells (Figure 4.3C). However, the elastic tension never did exceed 20nN, regardless of the initial line tension magnitude. Cells therefore gained more tension by increasing the myosin activity (see inset of Figure 4.8). Note that the relative weight of each contribution is dependent on how the rest-length is set, such that a L_0 smaller than d would lead to a higher active contribution; but the best fits were always obtained for $L_0 = d$.

	λ_0 (nN)	λ_a (nN)	EA (nN)	σ_0 (nN/µm)
PAA gels	37.1 +/- 8.2	27.3+/- 8.3	386 +/- 143	0.73 +/- 0.16
PDMS	100.5 +/- 16.4	127	26.3	1.10 +/- 0.41

Table 4.2: Mean values +/- standard error for initial line tension, active contribution, bundle stiffness and cell bulk surface tension. The first row gives the values extracted from TFM data on PAA gels using the numerical model. The second row gives λ values measured with ultra-soft cantilevers (λ_0 and σ_0 are averages over 5 cells; λ_a and EA computed for 1 cell only, so no SE given; this also explains why λ_a is higher than λ_0). σ_0 was computed from λ_0 and R_0 using eq. (4.2).

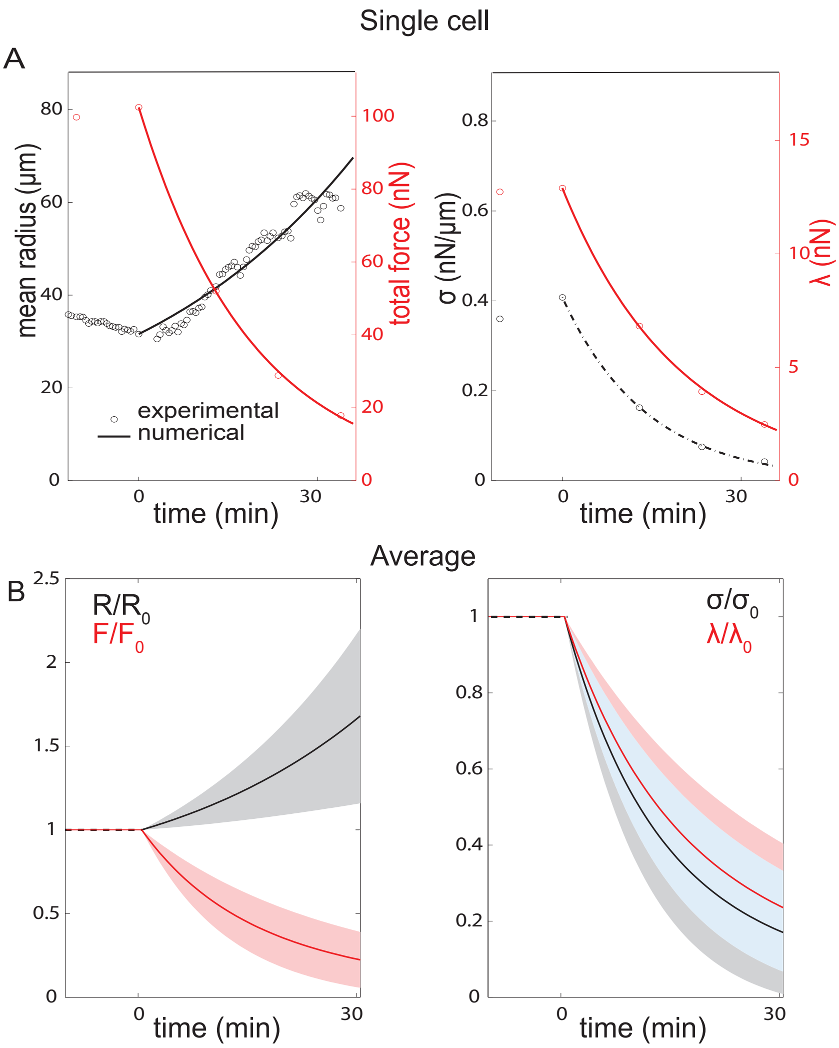

Figure 4.7: Fitting experimental results with the contractile elastic bundle model. A) Experimental (o) and numerical results (solid lines) showing evolutions of forces, arc radius and line and surface tension for a representative Y27632-treated cell. Left panel: mean arc radius (black) and total traction force (red); right panel: surface tension (black) and line tension (red). Drug was added at time t=0. Surface tension was fitted with an exponential decay indicated by the dotted line ($\tau = 14.1min$). Best value found for the active tension was $\lambda_a = 0.28nN$. B) Average of the numerical results for 10 cells (7 Y27632 + 3 blebbistatin treated), normalized to their initial values. The bands indicate the standard deviations around the mean values found over all cells, solid lines are the average values. Left panel: arc radius (black) and traction force (red); right panel: surface tension (black) and line tension (red). The blue band in the middle corresponds to the overlap of the black band (mean σ +/- std) and the red band (mean λ +/- std). The dashed red and black line are reminders that values are constant at t<0.

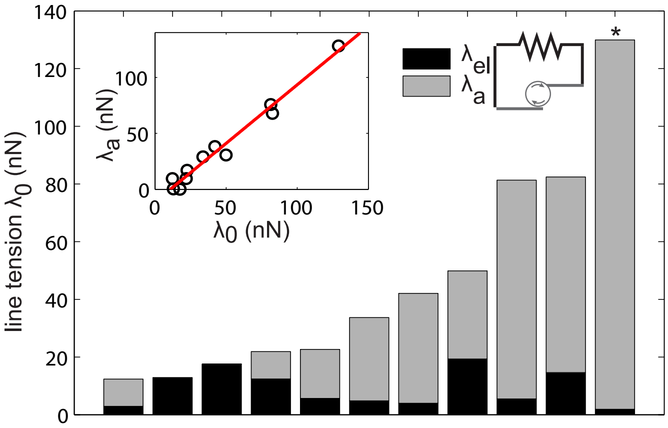

Figure 4.8: Balance of elastic and active contributions to the line tension. Values found by the model for the elastic contribution λ_{el} (dark bars, represented by the spring) and the contractile contribution λ_a (gray bars, represented by the active element) to the total line tension λ_0 for 11 different cells. In 10 cells, λ_0 was measured with the TFM technique; in 1 cell (*), λ_0 was measured with cantilever-based technique. Inset shows the active contribution as a function of total line tension, with a linear fit (red dotted line).

4.4 Discussion

4.4.1 Diversity of shape response

We have presented in the section 4.2 our experimental measurements of the dynamics of traction forces and shape of individual living cells, and explained our observations with an analytical model. We found that the fiber radius increased upon inhibition of myosin contractility (Figures 4.3 and 4.7). These experimental results are consistent with a previous study [Tanner et al., 2010] on living cells, but others, measuring populations of fixed cells, found curvature radii 2 to 5 times smaller for Y27632 treatment with respect to control cells [Théry et al., 2006a, Bischofs et al., 2008]. Following individual cells during drug treatment we have only occasionally observed collapse of the cytoplasm between the branches of adhesive pattern leading to a decrease of apparent arc radii. We therefore examined how experimental conditions might modify the cellular response to myosin inhibition.

We first verified that lower arc radii were not an artifact of fixation protocols. For this we systematically imaged cells before Y27632 treatment, before fixation and after fixation. We found that fixation, whether combined with the use of an extraction buffer or not, does not alter cell shape. We then compared cell shape response to myosin inhibition for various experimental conditions. We varied spreading time (4 hours or overnight), serum concentration (10% or no serum) and the type of medium (Leibovitz-15, which is buffered as appropriate for live imaging, and DMEM, standard medium used for cell culture). We found that a collapse of the cytoplasm became the dominant response when the cells were spread on adhesive patterns for only a short time (as in Théry et al. [2006a]) or in the absence of serum (as in Bischofs et al. [2008]). Surprisingly, this was also the case for cells in DMEM, compared to cells in L-15, although in both cases, cells were kept in an atmosphere-controlled incubator. The difference was not due to pH discrepancies, so we can only guess that medium composition might have an influence on cell metabolism. Examples are given in Figure 4.9. Note that in all the cases of cell collapse, the peripheral arcs were disassembled. In contrast, the mechanical model presented above focuses on the situation where myosin activity was reduced, but the cytoskeletal organization remained largely intact, so that it was possible to assign and measure a line tension in the arcs.

4.4.2 Cytoskeletal remodeling during myosin inhibition

In the experiments presented above, we continued monitoring cell shape and tension after washout of the drug with normal medium. While the traction forces increased back to their initial levels, cell area did not always recover completely, i.e arc radii did not reduce to pre-drug value. One possible explanation for this incomplete recovery is that Y27632 treatment induces partial detachment of the peripheral bundles from the cytoplasm. This would artificially decrease the surface tension acting on the bundle radius, leading to higher radii than in normal conditions. Figure 4.10 shows that the intensity of actin is much lower just behind the edge of the cell after myosin inhibition. Considering shape and tension dynamics during recovery after drug washout would therefore necessitate to take cytoskeleton remodeling into account to modify the initial and final cell state. These observations also bring forward the fact that the reference shape associated to an elastic medium is in this case modified by the cytoskeleton remodeling, a useful process for dynamic cell shape adaptation.

4.4.3 Assumption of constant arc elasticity

In both TFM and cantilever-based experiments, we explain the increase in arc radius under myosin inhibition by the fact that surface tension in the cell bulk drops faster than the line tension in the peripheral arc. Indeed, a model of a contractile elastic bundle, in which the line tension is the sum of elastic and active contributions accurately reproduces the experimental behavior of peripheral arcs. This is the simplest model to account for our experimental observations, where we kept linear dependencies of line and surface tension on motor activity. However, we cannot exclude that there are some more complex forms

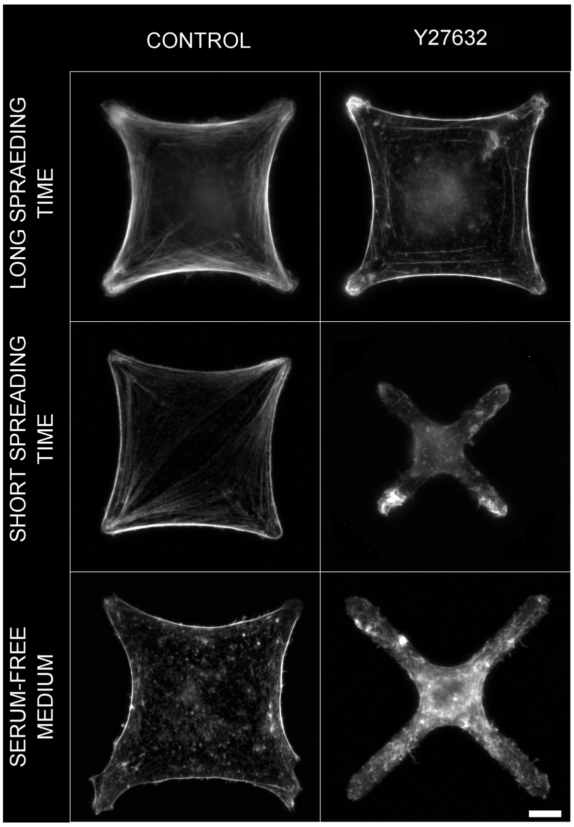

Figure 4.9: Influence of experimental conditions on cell response to contractility inhibition. REF 52 cells were seeded on cross-shaped patterns, and left to spread for a few hours (middle row) or for over 12 hours (top and bottom row). Cells were then incubated in control conditions (left) or with Y27632 (right) for 30 minutes. The cells in the bottom row were incubated in serum-free medium. After 30 min, cells were fixed with 3% paraformaldehyde in cytoskeleton buffer and rinsed with PBS. Alexa-Phalloidin 488 was used to mark F-actin. A loss of cytoskeletal coherence in the bulk of the cell is apparent in the cells after 30min in serum-free medium, and the the Y27632 treated cells after short time of spreading. The cytoskeleton might not have been sufficiently reinforced to sustain the contractility inhibition. This behavior was only very rarely observed when cells were left to spread for a longer time, and the Y27632 was diluted in serum-containing medium. Scale bar, 10µm.

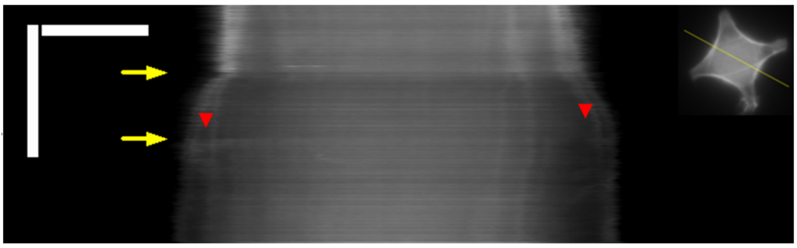

Figure 4.10: Incomplete area recovery. Kymograph of actin intensity (marked by Lifeact EGFP) along a line spanning the middle of the cell (shown in inset). Horizontal scale bar is 10µm; vertical scale bar is 60 minutes. There is a depletion of actin after drug treatment behind the outer peripheral bundle (red arrowheads). The two yellow arrows indicate time of Y27632 addition and washout, respectively.

of dependence that may also result in similar trends, but there are no theoretical or experimental indications of what these could be. On the other hand, the hypothesis of elasticity is biologically justified by the presence of cross-linking proteins, and the bundle stiffness is expected to depend on the nature and the structure of these cross-linkers. Note that myosin could be necessary in the formation of an elastic structure, even though the elastic forces mentioned here are myosin-independent. Nonetheless, our results indicate that elastic behavior allows cell expansion independently of active processes. It was already known that cells spread on homogeneous substrates expand when myosin is inhibited, due to higher membrane protrusion activity [Cai et al., 2010, Yam et al., 2007]; but using patterned substrates we here demonstrate that cell expansion could also be due to elastic forces. Passive elastic forces could thus contribute to shape dynamics in cells.

Other models have attempted to distinguish between active and passive contributions to cytoskeletal tension, but have not addressed the dynamic aspect [Albert and Schwarz, 2014], or have concentrated on much shorter timescales, during which viscous effect were dominant [Kumar et al., 2006, Tanner et al., 2010]. Here, for the first time, we separately estimate the active tension and elasticity in fibers (Table 2), and demonstrate that combined elastic and active contributions account for the shape changes upon inhibition of myosin contractility. This has been done considering that bundle stiffness EA stays constant during myosin inhibition. The values found for 11 different cells are dispersed over several orders of magnitude, with a first group between 30nN and 200nN, and a second group above 350nN (Table 4.2). A previous analysis of static cell populations proposed that line tension variations could be due either to bundle stiffness (elasticity control mode), or to active contractility (tension control mode) [Bischofs et al., 2008]. However, it was not possible to distinguish between these two modes. We here bring experimental evidence for the existence of both these modes and show that they are in most cases complementary, as illustrated in Figure 4.8. The corresponding values of EA both for tension control and elasticity control are consistent with other numerical estimations, in which values between 40nN and 2000nN were found [Albert and Schwarz, 2014]. An existing experimental estimation also gives a stiffness of 46nN for isolated stress fibers of vascular smooth muscle cells [Deguchi et al., 2006]. This range of values shows that different organizations of the acto-myosin cytoskeleton and cross-linking proteins can generate bundles of various strengths, either within a population of cells or across different cell types. It is interesting to note that although line tension is higher on the more rigid PDMS, bundle stiffness was actually lower than on the PAA gels, showing that substrate stiffness may have opposite effects on myosin activity and on bundle elasticity.

The assumption of a constant bundle stiffness may need to be reconsidered, given that the elastic properties are likely dependent on the density and on the activity of myosin motors and on other cross-linkers such as α-actinin [Yoshinaga and Marcq, 2012]. It has been shown that blebbistatin reduces the rigidity of actin meshworks [Balland et al., 2005], presumably due to its effect on myosin. It is possible that Y27632 also reduces EA. Changes in bundle stiffness can be estimated by computing the strengths of the arcs, given by the relative actin intensity of the arcs with respect to the cell interior [Bischofs et al., 2008]. Our measurements suggest that arcs are weaker and thinner after myosin inhibition, indicating that there could be some remodeling of the cytoskeleton (data not shown). To estimate the possible effect of a decrease of stiffness, we assumed that EA dropped half as fast as σ. This did neither lead to major differences in the numerical solutions, nor to better agreement with our experimental data, suggesting that such variation of bundle stiffness does not significantly impact cellular response.

However, a drop in bundle stiffness faster than the loss in surface tension would lead to lower radii, thus shrinking cells. Yet another behavior is found when the nature of evolution of bundle stiffness differs from that of the surface tension: the radius may then change non-monotonically, e.g. first decreasing as the changes in stiffness dominate, then increasing when the drop in surface tension becomes more important. It is possible that different types of dynamical behavior may yet be discovered when the living cell dynamics are studied more extensively. The interplay between the motor inhibition kinetics and the changes in bundle stiffness could account partially for the minor differences in the response to blebbistatin or Y27632. Indeed, Y27632 and blebbistatin use different mechanisms to inhibit myosin. This could lead to different effects of each drug on EA: blebbistatin acting directly on the motors, its effect on contractility should be faster, and may be reinforced by a stronger drop in bundle stiffness. Additionally, inhibition of LIM-kinase by Y27632 could lead to a marginal over-activation of cofilin. Cofilin-mediated disassembly of actin filaments would contribute to an increased drop of surface tension [Tinevez et al., 2009]. The differential effects of blebbistatin on bundle stiffness and of Y27632 on surface tension may provide an explanation for our experimental results (Figure 4.3), in which traction forces decayed faster and radii increased less in blebbistatin-treated cells than in Y27632-treated cells. These effects could be integrated in the analytical model by adding another time dependent factor to EA or σ, but then one parameter would have to be fixed arbitrarily, since there would be too many unknowns. Thus other measurements are needed to clarify the relationship between bundle stiffness and contractility. One possibility is to attempt obtaining a more direct estimate of fiber elasticity during inhibition by active deformation of the fiber. This is the direction taken in the next chapter.

Conclusion

Acto-myosin bundles are prominent cytoskeletal features involved in many cellular and supra-cellular processes, whose mechanism it is important to understand. We studied the equilibrium of shape and tension in peripheral arcs of adherent fibroblasts on micro-patterned substrates. Inhibiting myosin with low concentrations of either Y27632 or blebbistatin resulted in a concomitant increase of peripheral arcs' radii of curvature and drop of traction forces down to 20% or 50% depending on the myosin inhibitor, of their initial level. These changes in shape are coupled to changes in line and surface tensions, as captured by the tension equilibrium law. We showed by different techniques that both λ and σ decrease, though not at the same rate. This is explained by the superposition of myosin-independent elasticity and myosin-dependent contractility in the line tension. Our numerical results demonstrate that the model of contractile elastic bundle appropriately describes the mechanical response of arcs during myosin inhibition. We found that the active contribution scales with the total line tension in the arcs. This model could be further refined to include the change of bundle stiffness and to explore how the force-shape coupling is controlled throughout cell spreading, or cytoskeleton remodeling.

Chapter 5

Mechanical properties of *in situ* semi-isolated fibers[1]

In the analytical model presented in the previous chapter, we assumed that bundle stiffness remained constant during myosin inhibition. Our experimental measurements did not allow to challenge that assumption directly. To obtain a more direct estimation of how the viscoelastic properties of peripheral stress fibers may change under perturbations, we turned to micro-manipulation experiments on mechanically isolated fibers. Isolating fibers has the advantage of removing the surface tension contribution, thus leaving fibers to be straight. SU-8 Cantilevers are used to deform a fiber perpendicularly to its length, and monitor the force with which it resists to transverse deformation. The goal is to measure the fiber's spring constant and internal viscosity in a single experiment and under different contractility conditions, with the idea of understanding what are the molecular components determining the fiber's mechanical properties.

Others studies have used micromanipulation of chemically extracted fibers to estimate their strength and longitudinal extensibility [Deguchi et al., 2006, Matsui et al., 2013], or fiber laser ablation to estimate fiber viscosity from the recoil velocity [Kumar et al., 2006, Colombelli et al., 2009]. From those results, we expect that stress fibers are highly extensible (i.e. can be strained up to 400%), with recoil time constants in the order of 1-10 seconds; but in contrast to the methods used in those investigations, we chose to impose an orthogonal deflection of the fiber, and to keep the fibers intact. Thus no chemical attachment between the cantilever and the fiber was necessary, and this protocol allowed for multiple perturbations of several fibers with the same cantilever.

---

[1] Results of Chapter 5 to be published in Labouesse et al., [2015b]

5.1 Methods

5.1.1 Experimental setup for fiber isolation and deformation

Rat embryonic fibroblasts were seeded on 3-dimensional patterned substrates, so as to be suspended, and allow for the movement of the cantilever. PDMS patterns of 5µm to 10µm high were thus fabricated. The top surface of the patterns was stamped with fibronectin for robust cell attachment (see section 2.2.3 for details). The patterns used had several large non-adhesive gaps to trigger formation of thick peripheral bundles. A SU-8 cantilever was mounted on a manual micromanipulator on one side of the microscope stage. Opposing the cantilever, a glass capillary (Femtotips, opening diameter of 0.2µm to 0.5µm) was mounted on another micromanipulator unit. This was used to make microinjuries in the cells, in order to isolate the fibers from the cytoplasm. Microinjuries were easily done on cells which had a thin stretch of cytoplasm between the pattern branches. In those cases, the hole in the cytoplasm would enlarge spontaneously. We checked that isolating fibers did not compromise their integrity. Fibers indeed still straightened back to their original shape when released, being kept in place by the remaining adhesive complexes at its tips. The fixing and staining for actin and myosin confirmed that they were present in the isolated fiber (Figure 5.1 and 5.2).

5.1.2 Experimental protocol

Deformation of isolated fibers at fixed velocity

Our approach is similar to the one used in Bernal et al. [2007] to study the mechanical properties of axons. They have indeed also employed microneedles to deform isolated axons. They were able to separate the axons' response into three different regimes, according to the deformation rate and the timescale of relaxation. They used this to map the axon's response onto a 3-parameter-solid model (Figure 5.3). Briefly, they first applied a fast deformation, to which the axon responded with an elastic behavior. The deformation rate was such that viscous response was negligible. They then kept the transverse elongation constant, allowing the axon to relax while being kept under tension. In a first step, the response resembled a viscoelastic exponential relaxation. In a second step, myosin motor activity led to active contraction. Although our system is different in that stress fibers are shorter and do not contain microtubules, the same protocol could be applied here. We therefore imposed sequentially a fast transverse elongation and a constant transverse elongation and sought to dissociate the mechanical response into an elastic component and a viscoelastic component.

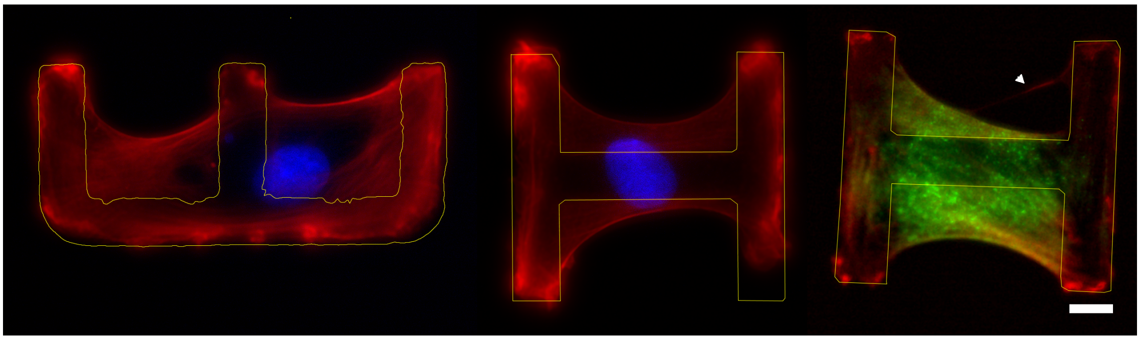

Figure 5.1: Immunostaining of cells spread on PDMS geometrical patterns, fixed and stained for actin (red), nucleus (blue) and myosin II b (green, right panel). The pattern contour is indicated in yellow. The cell in the right panel was fixed after the fiber had been isolated (arrowhead). After several hours, the hole had not closed, but the fiber, initially horizontal had slid along the contour. Low levels of myosin are present in the fiber, though the contrast does not allow to distinguish here. Scale bar, 10µm.

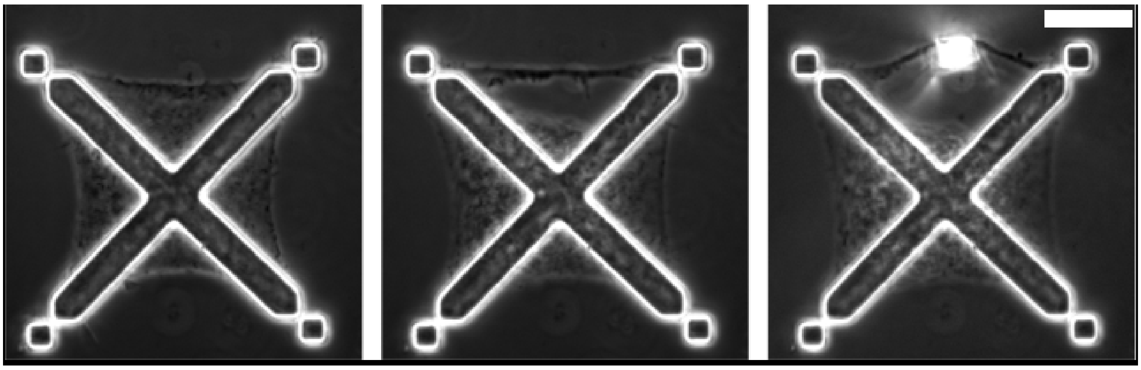

Figure 5.2: Fiber isolation: REF cell on a cross-shaped pattern, before fiber isolation (left) and after fiber isolation (right). A soft cantilever (bright rectangular spot) is placed against the fiber and a transverse deformation is applied.

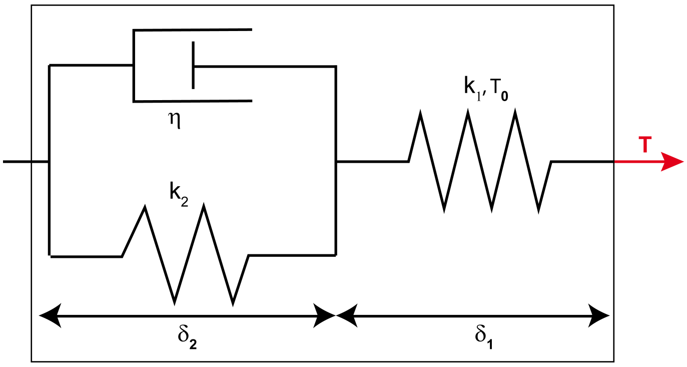

Figure 5.3: Schematic modeling of a stress fiber as a 3-parameter solid. A spring of constant k_1 and active pre-tension T_0 is in series with a viscoelastic element composed of a spring k_2 in parallel with a dashpot η.

To do so, a cantilever was placed in the hole in the cytoplasm, behind the fiber of interest. A given velocity was then imposed to the motorized microscope platform, typically ~5µm/s, over a course of ~ 20µm, resulting in a movement of the cantilever relatively to the fiber. Thus a transverse deformation was applied at the center of the fiber (Figure 5.2). Note that no control loop was implemented here, so that the target velocity was the maximal possible velocity, reached if the fiber opposed no resistance to deformation. The actual deformation rate depended on the relative stiffness of the fiber compared to the cantilever stiffness. Cantilever stiffness could be adjusted by varying their lengths h, the stiffness varying as $1/h^3$. The most rigid cantilever was 6.25nN/µm (0.5mm long), while the less rigid was 0.6nN/µm (1.1mm long). Fiber and cantilever movements were imaged using the streaming mode (ultra-fast acquisition) of the camera to reach acquisition frequencies of at least 10Hz. This was the limiting factor for the imposed deformation velocities, since higher velocities resulted in lower image sampling frequency. 5 µm/s was therefore a good compromise between fast deformation and sufficient sampling frequency. The respective fiber and cantilever deformations were then obtained by aligning the images to the first slice. Fiber length was also measured using the pattern as a landmark when contrast was too low and it was too difficult to distinguish the end of the fibers.

5.1.3 Derivation of model equations

We give here the derivation of the force-elongation relations that are used in the analysis of the experiments presented here. The final equations have been given by Bernal et al. [2007]. The model follows a 3-parameter-solid subjected to transverse deformation (Figure 5.4). The validity of this model is discussed in section 5.3.1. In the first phase (traction), simple elastic regime is assumed (this is justified in section 5.2.1, therefore only the first spring k_1 is considered. In the second phase (relaxation), all three elements are considered. Equilibrium is assumed such that the force on the cantilever balances the tension in the fiber (Figure 5.4).

Elastic regime

The force balance between the tension T in the fiber and the force on the cantilever $F_c = k_c \delta_c$ (k_c = cantilever spring constant, δ_c = cantilever deflection on the y-axis) is given by $F_c = 2T\sin(\theta)$, with $\sin(\theta) = \frac{e}{L} = \frac{x}{\sqrt{1+x^2}}$ and the normalized transverse elongation $x = e/d$. We here assume elastic tension in the fiber, such that $T = k_1\delta + T_0$. T_0 is a pretension due to the action of myosin motors, k_1 is the primary spring constant, and δ the fiber elongation, which is geometrically given by

$$\delta = L - d = \sqrt{e^2 + d^2} - d = d(\sqrt{x^2+1} - 1).$$

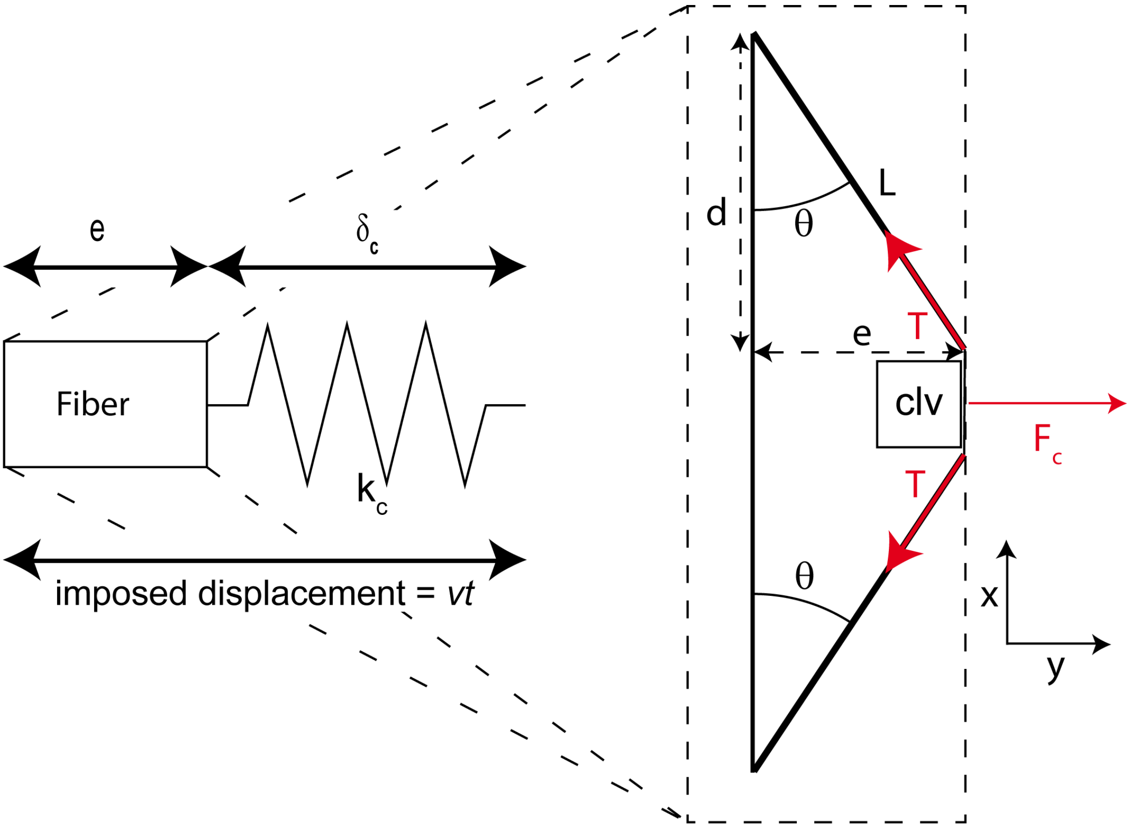

Figure 5.4: Schematic of experimental system and force balance during traction. The fiber is pulled by a cantilever of spring constant k_c. The total transverse elongation of the system fiber + cantilever is $e + \delta_c = v \cdot t$. During the relaxation regime, this transverse elongation remains constant, although the transverse fiber elongation e and the cantilever elongation δ_c change. The global geometry of the system is detailed on the right side. The tension T in the fiber on either side of the cantilever balances the force F_c with which the cantilever deforms the fiber. d is the length of the straight fiber segment, L is the length of the deformed fiber segment, e the indentation and θ the angle of the fiber with its axis at rest. The tension T is determined by the mechanical model sketched in Figure 5.3.

The rest-length is implicitly taken to be equal to d for the half-fiber segment. Hence,

$$F_c = \frac{2Tx}{\sqrt{1+x^2}} = 2k_1 d(x - \frac{x}{\sqrt{1+x^2}}) + 2T_0\frac{x}{\sqrt{1+x^2}} \qquad (5.1)$$

Viscoelastic relaxation under constant tension

In the second phase, we consider that the viscoelastic relaxation increases the fiber longitudinal deformation although the total transverse elongation $e + \delta_c$ is kept constant. As above, $F_c = k_c\delta_c$. The first spring (constant k_1, elongation δ_1) is in series with 2 parallel elements, a dashpot η and a secondary spring (k_2, δ_2). The sketch of the projection, in the limit of small additional deformations is given in Figure 5.5. Writing the force balance

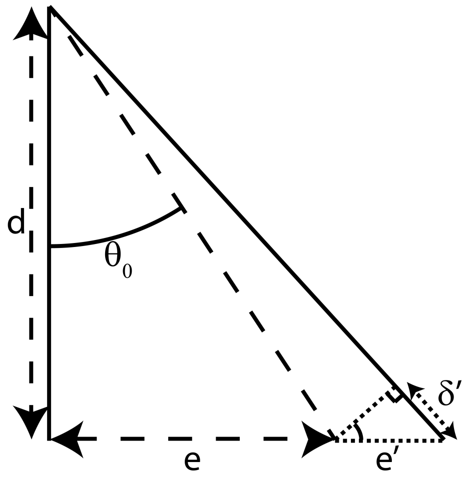

Figure 5.5: Sketch of the geometry for the relaxation regime, in the limit of small additional deformations $\theta \approx \text{cst} = \theta_0$.

along the fiber axis yields the following three equations:

$$\begin{cases} T = k_1\delta_1 + T_0 \\ T = k_2\delta_2 + \eta\dot{\delta_2} \\ T = \dfrac{k_c\delta_c}{2\sin(\theta)} \end{cases} \quad \Rightarrow \quad \begin{cases} \dfrac{k_1}{\eta}\delta_1 + \dfrac{T_0}{\eta} = \dot{\delta_2} + \dfrac{k_2}{\eta}\delta_2 \\ k_1\delta_1 + T_0 = \dfrac{k_c\delta_c}{2\sin(\theta)} \end{cases} \tag{5.2}$$

with $\delta = \delta_1 + \delta_2$ the total elongation of the fiber. It is best to express this last equation in terms of the additional deformation δ' due to viscoelastic effect after the initial traction: $\delta = \delta_0 + \delta'$ with $\delta' = \delta_2 - \delta_1'$ and $\dot{\delta} = \dot{\delta'} = \dot{\delta_2} - \dot{\delta_1'}$. Similarly, $\delta_c = \delta_c^0 - \delta_c'$, with δ_c', $\delta_1' > 0$. The variables are kept positive, but the minus sign in the relations indicate that δ_1 and δ_c decrease, while δ_2, δ and e increase. δ_0 and δ_c^0 are constants determined by the final transverse elongation after the elastic traction: $2(k_1\delta_0 + T_0)\sin(\theta_0) = k_c\delta_c^0$. Equation (5.2) rewritten is

$$\begin{cases} \dfrac{k_1}{\eta}\delta_1 + \dfrac{T_0}{\eta} = \dot{\delta'} + \dot{\delta_1'} + \dfrac{k_2}{\eta}(\delta' + \delta_1') \\ k_1\delta_1' = \dfrac{k_c\delta_c'}{2\sin(\theta)} \end{cases}$$

Since the total deformation velocity is zero, the projection on the y-axis in the limit of small additional deformations ($\theta \approx \theta_0$) yields $\dot{\delta'} = \sin(\theta_0)\dot{e'}$ and $\delta' = \sin(\theta_0)e'$. Finally, since the total transverse elongation is kept constant, $e' = \delta_c'$. Using these relations, we can rewrite the equations as a function of e, $\dot{e}$ and $A = k_c/(2\sin(\theta_0))$ only.

$$\begin{cases} \dfrac{A\delta_c^0}{\eta} - \dfrac{Ae'}{\eta} = \sin(\theta_0)\dot{e}' + \dfrac{A}{k_1}\dot{e}' + \dfrac{k_2}{\eta}\left(\delta' + \dfrac{Ae'}{k_1}\right) \\ \qquad\qquad \delta' = \sin(\theta_0)e' \end{cases}$$

$$\Rightarrow \left(\sin(\theta_0) + \frac{A}{k_1}\right)\dot{e}' + \left[\frac{k_2}{\eta}\left(\sin(\theta_0) + \frac{A}{k_1}\right) + \frac{A}{\eta}\right]e' = \frac{A\delta_c^0}{\eta} \tag{5.3}$$

The right-hand side being constant, the equation therefore reduces to a first order differential equation, such that the solution is of the form

$$e' = e_\infty(1 - exp(-t/\tau)) \tag{5.4}$$

e_∞ is the asymptotic value of the additional displacement e'. Fitting δ_c' with this exponential function and measuring the slope at the origin α yields the time constant τ and η:

$$e_\infty = \frac{A\delta_c^0}{\eta(\sin(\theta_0) + A/k_1)}\tau \tag{5.5}$$

$$\tau = \eta\left(k_2 + \frac{A}{\sin(\theta_0) + A/k_1}\right)^{-1} \tag{5.6}$$

$$\eta = \frac{A\delta_c^0}{(\sin(\theta_0) + A/k_1)\alpha} \tag{5.7}$$

$$\tag{5.8}$$

5.2 Results from transverse fiber deformation

5.2.1 Elastic response of a fiber under traction

Validation of the elastic tension assumption

A fast transverse deformation was applied to the system fiber+cantilever at velocity v = 5µm/s. The deflection of the cantilever allowed computing the force with which the fiber resisted deformation. We then plotted the force on the cantilever against the relative fiber deformation projected along the displacement axis (y-axis). We first operated under the assumption of negligible viscosity. To check whether in this case the behavior was indeed elastic, we compared the results of fitting from two different models: one considering a constant tension in the fiber that would solely be due to motors $T = T_0$, and one considering an additional elastic tension in the fiber, i.e. increasing linearly with deformation $T = k_1\delta + T_0$ (as in the model used in Chapter 4). Projected on the y-axis, the constant tension and the elastic tension models follow respectively (5.9) and (5.10):

$$\text{constant Tension} \qquad F_c = 2T_0 \frac{x}{\sqrt{1+x^2}} \tag{5.9}$$

$$\text{elastic Tension} \qquad F_c = 2T_0 \frac{x}{\sqrt{1+x^2}} + 2k_1 d \left(x - \frac{x}{\sqrt{1+x^2}}\right) \tag{5.10}$$

where F_c is the force on the cantilever, k_1 the fiber spring constant, T_0 the initial tension and $x = e/d$ the normalized transverse elongation (see Figure 5.4 for an illustration). In both models, the force on the cantilever increases with the elongation, but nonetheless constant tension and elastic tension behavior could be discriminated in most cases. Examples of those two fittings are given for a representative cell in Figure 5.6. The results confirmed that peripheral fibers can be stretched elastically, up to at least 40% strain ($x = 1$). Thus the model already introduced in Chapter 4 of an additive elastic tension and initial (myosin-powered) tension is here further validated.

Fibers from 22 REF cells were probed with this method, using cantilevers of various stiffnesses. In some cases, fibers were deformed several times and allowed to relax in between each stimulation. Each traction event was fitted separately. The resulting k values and T_0 values are plotted in Figure 5.7. The order of magnitude of median values $k_1^{med} = 1.6\text{nN}/\mu\text{m}$ and $T_0^{med} = 4.3$ nN are similar to previous reports [Deguchi et al., 2005; 2006, Matsui et al., 2013], and the corresponding EA ($EA = k_1 d$) values go up to 45 nN, which is the lower range of what was measured in Chapter 4.

Fiber extensibility and homogeneity of k_1

We tested how far fibers could be elongated within the same elastic regime. In a few cases, we could stretch the fibers to a strain close to 120% (i.e. a transverse elongation $e = 2d$) without breaking the fibers. We did not observe any systematic change of regime at these particular elongations, the elastic tension model fitting could therefore be applied to the whole course of deformation with no change in the output values compared to fittings done in the small deformation regime only. Matsui et al. [2013] have shown that stress fibers can be axially stretched without tearing the fiber to 3.75 times their length, with similar deformations for each unit along the fibers. The strain was therefore more or less uniform along the fiber. Here we do not have access to the local strain (fibers were not marked fluorescently), but our results show that important fiber stretching is also possible when fibers are elongated transversely. Although such elongations are not physiological, it is significant that these stress fibers are highly deformable both axially and transversely, since they have to sustain high loads at the cell periphery (see Figure 3.15).

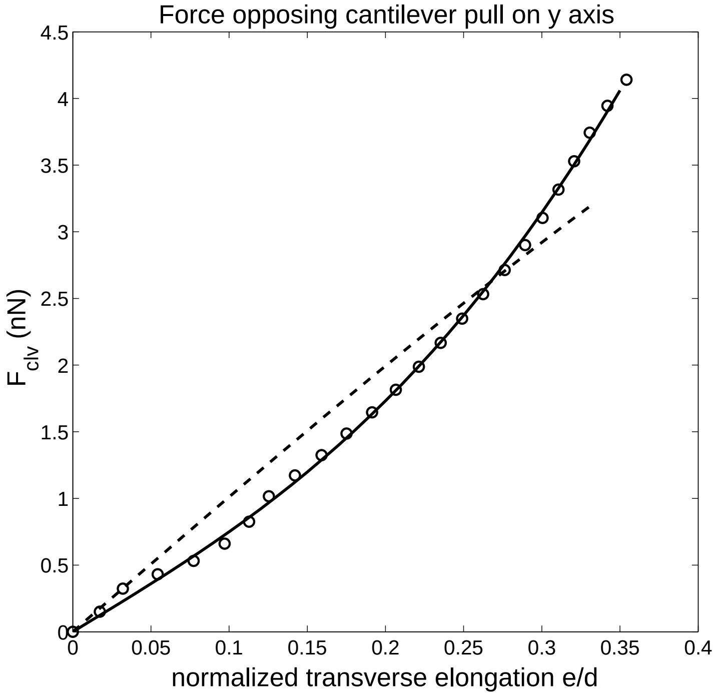

Figure 5.6: Comparison of elastic and constant tensions models. Data ("o") showing the force against the cantilever (nN) versus the transverse elongation normalized by the half spanning distance (e/d). Best fits using a constant tension model (dashed line) and an elastic tension model (solid line). The corresponding values are $T_0 = 5.1nN$ in the constant tension fit, k_1=3nN/µm, T_0=3.6nN in the elastic tension fit. R^2 values indicated that the elastic fit was marginally better (0.998 against 0.952), but the residuals were 6 times lower, clearly indicating that the fiber responded elastically to the deformation.

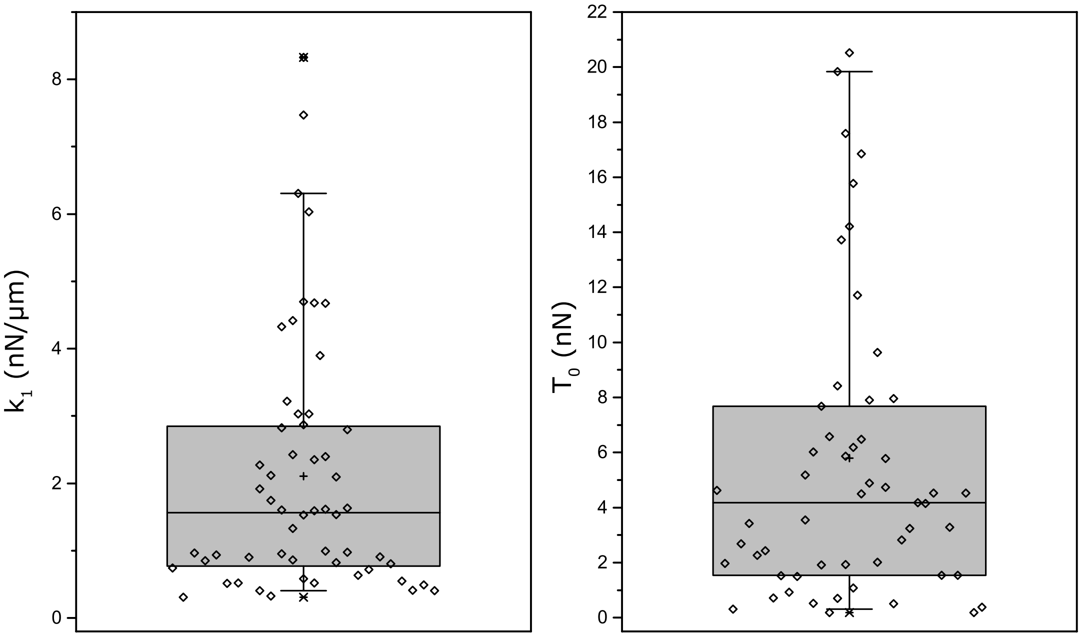

Figure 5.7: Distribution of spring constants and initial fiber tension. Boxplot of k_1 (left) and T_0 (right) from 64 traction experiments on fibers from 22 different cells. The central line indicates the median, the central plus shows the mean, the box limits are the 25^{th} and 75^{th} percentiles and the whiskers correspond to 5^{th} and 95^{th} percentiles. The data points (◇) are added to the plot.

Influence of strain rate

To verify whether the response to traction was purely elastic, two points need to be considered: 1) independence of k_1 from the strain-rate (same k_1 at faster deformations) and 2) negligibility of viscous effects , i.e. the fiber is pulled fast enough so that the viscous elements do not have time to respond. We therefore changed the deformation velocity by a factor 2, while pulling on the same fiber to compare the resulting force on the cantilever. No significant differences were found, allowing us to keep the assumption of a single elastic response during the traction event. However, one problem we faced is that at higher strain rates, some irrgular oscillations were observed (Figure 5.12), probably due to a limitation of the experimental setup, as discussed further in section 5.3.3.

Effect of Y27632 treatment

To assess the contribution of myosin to the tension of the peripheral fibers, we performed the same measurements in contractility inhibiting conditions. As in Chapter 4, we used 10µM Y27632 diluted in the imaging medium. We first measured k_1 and T_0 in control conditions, then again for the same fiber after treatment with Y27632. To compare the evolution of k_1 and T_0 for 4 different fibers, they were normalized to the their pre-drug values k_i and T_i. We plot these normalized values in function of drug incubation time (Figure 5.8). Results show that fiber pre-tension T_0 indeed decreases with Y27632 treatment, as expected since T_0 is attributed to myosin motor activity, but are not conclusive on the spring constant k_1, since both lower and higher values of k_1 have been measured after myosin inhibition.

5.2.2 Viscoelastic relaxation over short time scales

After the first phase of traction, the motorized platform was kept still, but the fiber was observed to continue relaxing on a time scale of a few seconds. This resulted in a continued elongation of the fiber but a reduced tension, thus the term “relaxation”. This first of all brings evidence that there is some damping in the fiber, which is thus not purely elastic. Further confirmation comes from the fact that a fiber does not instantaneously relax when released, but instead needs several seconds to straighten. Therefore a viscous element should be taken into account at the relaxation stage in the mechanical model of a fiber. Since we observe a decrease of force together with an increased fiber elongation, it means that the strain on the spring has been partly absorbed by another element in series. Following Bernal et al. [2007], a secondary spring and dashpot in parallel are used to describe the relaxation (see Figure 5.3 for a sketch of the model), and are added in series

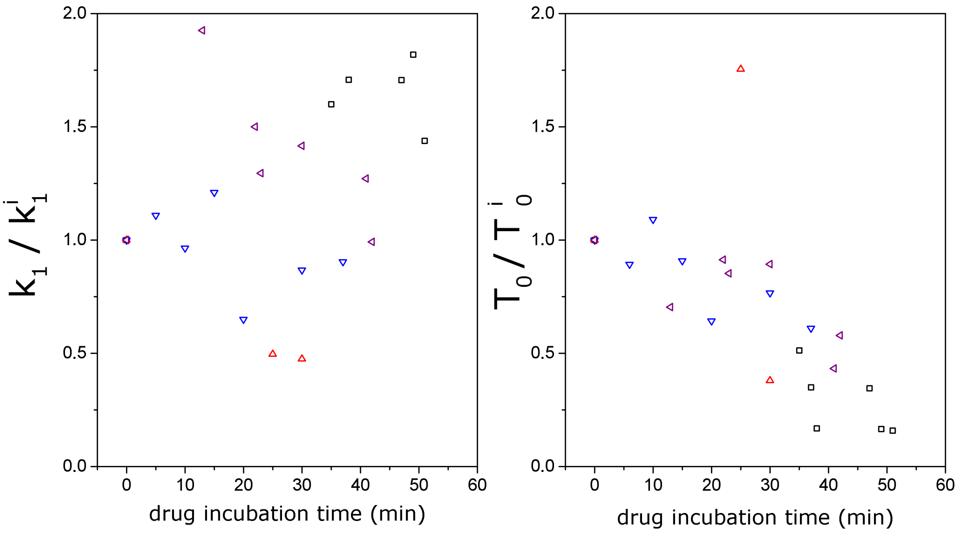

Figure 5.8: Y27632 decreases fiber pre-tension. Relative values of k_1 (left) and T_0 (right) during Y27632 treatment. Values were normalized by the pre-treatment values (average of all the stimulations done before adding the drug). Each symbol corresponds to a different batch of experiments.

to the elastic component k_1 stretched in the traction regime. The second spring serves to impose a reference length to the dashpot element, but we consider its pre-tension to be null (see section 5.3.1 for further discussion of the model). The additional transverse elongation e' observed here was limited (in average below 7% of the maximal elongation in the traction phase) so that the approximation of small additional deformations (leading to $\theta \approx \theta_0$ in eq. (5.3)) holds in this regime. To exploit these data, we therefore computed this extra-deformation and used its time evolution mapped to eq. (5.4) to infer τ and η from eqs. (5.6) and (5.7).

After a few seconds, irregular behavior in terms of force and elongation was observed, similarly to what is presented in Bernal et al. [2007] when myosin motors start contracting the fiber (Figure 5.9a). Consequently, only the initial regular relaxation was fitted to determine the viscosity coefficient (the subsequent active relaxation is discussed in section 5.3.3). The range of "regular" behavior was determined by varying the size of the fitting range, adjusting the parameters to fit the data to eq. (5.4). The longest range with the highest R^2 was selected, and used to determine to model parameters. Visual confirmation ensured that elongation increased exponentially in the chosen range. An example is given in Figure 5.9. The results for 16 cells are given in Figure 5.10. The order of magnitude of τ is of 1 sec (median value 0.6 sec), similar to what was found in laser ablation experiments [Kumar et al., 2006]. This brings further confirmation that isolating stress fibers does not alter their mechanical properties, which are intrinsic to their structure. Taken together, our results from both the traction and relaxation regimes, and those from Kumar et al. [2006] also show that fibers respond similarly to transverse and axial perturbations.

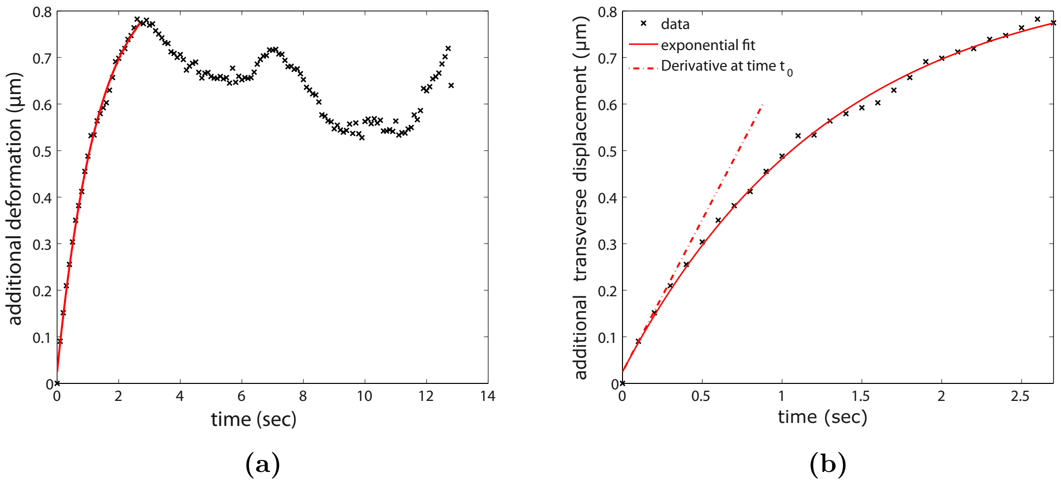

(a) (b)

Figure 5.9: Example of viscoelastic relaxation. a) Deformation over 13 seconds. b) Zoom on the first 2.7 seconds on which the exponential fitting was done. The red line in a) and b) shows the exponential relaxation, the dotted line in b) shows the slope at t=0. τ= 1.3s, η=8.2 nN.s/µm

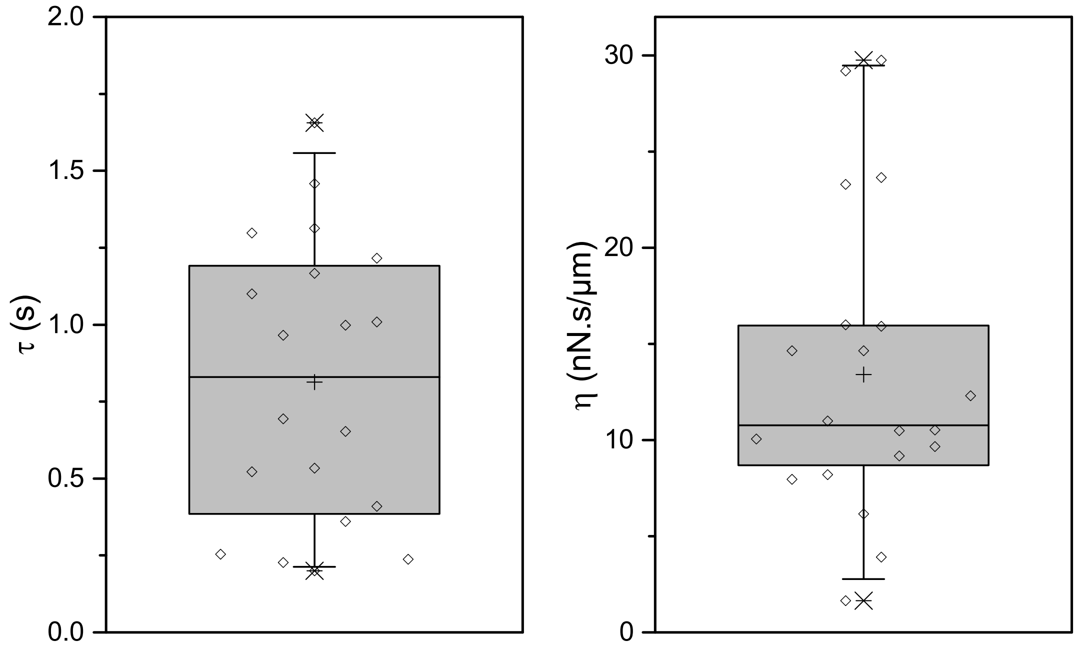

Figure 5.10: Distribution of time constants and viscosity coefficient. Boxplot of τ (left) and η (right) from 49 measurements on fibers from 20 different cells. The central line indicates the median, the central plus shows the mean, the box limits are the 25th and 75th percentiles and the whiskers correspond to 5th and 95th percentiles. The data points ($\diamond$) are added to the plot.

5.3 Discussion

5.3.1 Validity of a 3-parameter-solid model

A 3-parameter solid model was used to analyze the data extracted from these experiments. The reason for the choice of 3-parameter solid model as opposed to other classic viscoelastic models such as Kelvin-Voigt or Standard-Linear is that it was adapted to the separation of regimes, i.e. an elastic response during traction and a viscoelastic damping during relaxation. The main assumption here is thus that a single spring is sufficient to describe fiber tension during traction. This is verified by the force-elongation curves (Figure 5.6). During the second part, our data shows that 1) the feedback force on the cantilever decreases 2) there is an additional small elongation which is limited and 3) this additional elongation increases exponentially.

Point 1 argues to a smaller elongation of the primary spring k_1, thus part of its displacement must be absorbed by a dashpot element η in series ("$-$") rather than in parallel ("$//$"). Thus a Kelvin-Voigt system would not be suitable here, nor would a standard-linear model ($k_1//\{k_2 - \eta\}$) with the elements added in parallel to the primary spring.

Points 2 and 3 indicate that there is not a simple dashpot in series with the primary spring, which would lead to an infinite elongation, such as in a Maxwell model ($k_1 - \eta$) or in a 3-parameter fluid model ($\eta_1 - \{k_1//\eta_2\}$). However, adding a Kelvin-Voigt unit to the first spring leading to the so-called 3-parameter solid model ($k_1 - \{k_2//\eta\}$) yields exactly that evolution.

It is of course possible that other more complex models also fit the data, either using equivalences between elements or with additional elements (four or more). For example, a Standard-Linear model ($k_2^a//\{k_2^b - \eta\}$) could fit the relaxation regime, under the condition that $k_2^a + k_2^b = k_1$; but this means dissociating the primary spring k_1 into two springs. A single element will no longer describe a particular behavior. With the 3-parameter-solid model, we have thus chosen the simplest representation that could model the observed fiber response, and enable us to extract information on the regulation of mechanical properties.

The main assumption that viscosity can indeed be neglected during the traction remains to be validated on a cell-to-cell basis. From the values of η and τ, the slope of δ_c at $t = t_0$ (the start of relaxation), we can also estimate k_2. We found that k_2 was in average 16 times greater than k_1. This scaling is in sharp contrast with what was found by Bernal et al. [2007] in axons where k_2 was two orders of magnitude lower than k_1. In their case, this was consistent with the fact that the viscous response was much slower than the elastic response ($\tau > 10$s). In our case however, both the experimental data and the estimated relaxation times indicate that viscous response is over a time scale of seconds, thus similar to the time over which fibers are pulled during traction. However, $k_2 >> k_1$ here guarantees that the elastic response of the primary spring k_1 (which is softer) is dominating during the traction, and so $\delta_2 << \delta_1 \approx \delta$. Thus the separation of elastic and viscous relaxation regime is valid in an initial approximation, though it may not hold in the cases in which small k_2 values were found. To bring additional confirmation to the assumptions used, one possibility is to solve the full differential equation describing $e(t)$ for the four parameters k_1, T_0, k_2, and η to compare values, and check if a different set of parameters would fit our experimental data. This complex equation gives the temporal evolution of e, given an imposed total transverse elongation vt.

$$\eta\dot{e} = \frac{e(d^2+e^2)}{Cvtd^2+(1+C)e^3}\Bigg[\eta Cv - e(Ck_1 + C_k2 + k2) + \frac{ek_2}{\sqrt{d^2+e^2}}\left(d - \frac{T_0}{k_1}\right) + vtC(k_1+k_2)\Bigg]$$

C is a constant given by $C = k_c/2k_1$. The equation can be solved for $e(t)$ using numerical solvers. However, given that solving this equation for four parameters is too complex and not precise, we start by imposing as initial values the ones already found by separately fitting the elastic and viscoelastic behaviors on the force-extension curves, and check if they together give the proper temporal evolution for both the traction and relaxation phases. We will then explore if other set of parameters might also fit. This is the subject of ongoing analysis.

5.3.2 Dependence of mechanical properties on myosin activity

We expected that the initial fiber tension T_0 would drop when myosin was inhibited, since it is known that fibers are under pre-tension due to the action of myosin motors [Deguchi and Sato, 2009]. The effect on k_1 was more difficult to predict since elasticity comes from the structural properties of the stress fibers, and the role of myosin as passive crosslinkers on this elasticity is unknown. Other studies have investigated the effect of myosin on cell elasticity. Nijenhuis et al. [2014] combined atomic force microscopy and scanning acoustic microscopy to find that Y27632 treatment reduced the elastic modulus by at least 2, as well as the shear modulus by a factor 3. The bulk modulus was unaffected. Their interpretation is that deactivating myosin motors leads to a lesser resistance to shear deformation, but does not change the elastic compressibility. In contrast, Martens and Radmacher [2008] found that cells treated with blebbistatin softened by a factor 3, but cells treated with Y27632 did not show any significant change in stiffness. Importantly, both these studies were concerned with the elastic modulus of the cell as a whole, not that of single fibers. Given the dense parallel arrangement of actin filaments and cross-linkers in stress fibers, the effect of myosin inhibition may be different on fibers than on the cell bulk. From these considerations, and the results from Chapter 4, we expected no or limited change of peripheral fibers' spring constant after Y27632 treatment. Our results do not contradict this expectation, but do not allow either concluding in a definite manner on k_1's dependence on myosin activity.

5.3.3 Deviations from linear viscoelastic behavior

Active relaxation over long time scales

To complete the comparison of our experimental results with those of Bernal et al. [2007] on axons, we briefly mention the onset of active contraction during the relaxation phase which is observed on time-scales of 1-10 sec. In the case of axons, slow active contraction was observed, which the authors modeled with an additional contractile element in parallel to the secondary spring and the dashpot. The average force produced by this contractile element is a function of the deformation rate and of motor sliding velocity, and can be represented by a Gaussian function of the relative speed of deformation with respect to motor velocity: $T_a e^{-\dot{\delta}_2^2/v_{mot}^2}$. The equation (5.3) determining $e'(t)$ becomes:

$$\beta\dot{\delta}'_c + \frac{T_a}{\eta} e^{-[\beta\dot{e}']^2/v_{mot}^2} + \left[\frac{k_2}{\eta}\beta + \frac{A}{\eta}\right]\delta'_c = \frac{A\delta_c^0}{\eta} \tag{5.11}$$

β is a constant given by $\beta = \sin(\theta_0) + \frac{A}{k_1}$. We applied the same analysis by assuming e' to be exponential as in section 5.2.2, then finding the values for T_a and v_{mot} so that the eq. (5.11) is satisfied. An example is shown in Figure 5.11 for the same cell as in Figure 5.9. The average motor velocity found is $v_{mot} = 0.37$µm/s. Although this value is higher than expected (see section 1.2.2), similar order of magnitudes have been previously reported in Bernal et al. [2007]. which iThus active contraction also occurs during the relaxation phase and is sufficient to explain the observed behavior following the initial pure viscoelastic response.

Oscillations during traction

The fiber response during the traction phase was assumed to be elastic, as detailed above. Although an elastic tension model fitted the experimental data properly, there were noticeable semi-regular oscillations of the measured force around the expected value (Figure

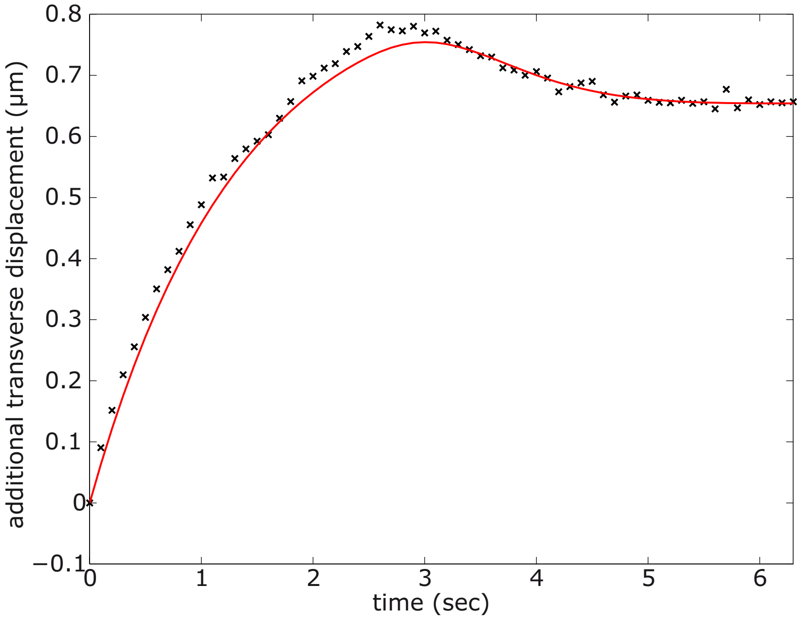

Figure 5.11: Active contraction counterbalances the fiber relaxation. Best fit over 6.3 sec found for T_a = 25nN and v_{mot} = 0.37μm/s.

5.12). These oscillations were repeatedly observed, in various batch of experiments. We therefore verified that the oscillations did not originate from a systematic error in the detection of the cantilever displacement. To this end, a free cantilever was tracked during platform movement with the same methods. No oscillations were observed, instead the cantilever movement was stable. However, following the movement of the motorized platform at high acquisition rate, we observed irregularities in the displacement speed, such that it periodically deviated from the nominal speed of 5μm/s. The periodicity of these deviations correlated with those of the observed oscillations (see Figure 5.13). Testing the uniformity of platform movement at different speeds revealed that these deviations come from a high pitch screw, best adapted for speeds 1000x higher. This means that our system would not be adapted for slower deformation velocities.

In the examples shown in Figure 5.12, which were obtained on a different system, we did not have access to the difference between nominal and effective displacement. It is likely that the observed oscillations also come from limitations of the automatized system, although the possibility of a non-linear mechanical response of the fiber cannot be completely discarded (such as stick-slip of the motors on the filaments).

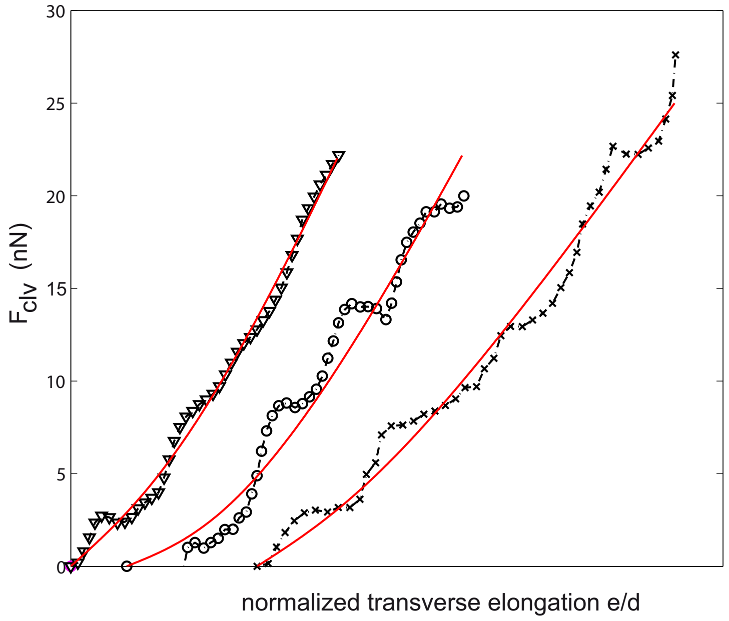

Figure 5.12: Force-elongation with semi-regular oscillations. Example of elastic tension fitting for 3 fibers during the traction regime. Fitting curve is in red, data in black. An offset on the x-axis was added to each set of data for better visualisation. The oscillations around the theoretical elastic curve (red) is systematic, although not identical. These examples were selected because the amplitudes of deviations were high. In other fibers, such oscillations are of comparable or smaller amplitudes.

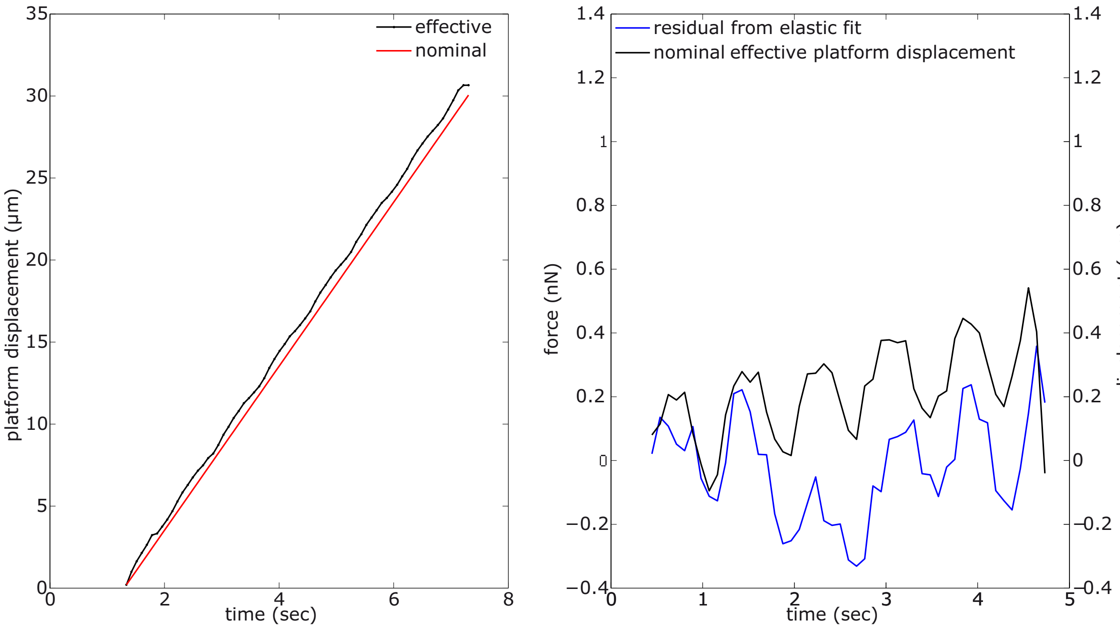

Figure 5.13: Irregular platform movement correlates with residual from elastic tension fit. (Left) Nominal platform movement set at 5µm/s (red) and actual platform displacement measured by image alignment (black). (Right) Oscillating residuals of elastic fit (blue, in nN), and difference between nominal and actual platform displacement (black, in µm).

Conclusion

In this set of experiments, we have probed the mechanical properties of isolated fibers and attempted to separate the elastic response from the viscoelastic response. To do so, we have used SU-8 cantilevers to apply a transverse elongation to the fiber, first at a constant velocity, then maintaining the total elongation constant and letting the fiber relax. Our results confirm that the peripheral fibers are highly extensible, and that they behave elastically during the traction phase. We found spring constants in the order of 1nN/µm, consistent with values found in previous studies, and T_0 values around 3nN. The goal was to verify how these values may depend on molecular components of the peripheral fibers. Treatment with ROCK inhibitor Y27632 resulted in a definite decrease of T_0, which confirms that active tension is lost when myosin motors are inactivated. No conclusion could be drawn from the measurements of k_1 under ROCK inhibition. To get further insight into the molecular underpinnings of k, it would be necessary to modulate the binding capacity of other cross-linkers such as α-actinin, or use genetic tools to knock-out its expression. This might reveal how the combination of motor activity and passive crosslinking participate in determining the mechanical properties of peripheral stress fibers.

At low deformation rates (i.e when the transverse elongation was kept constant), viscoelastic behavior was observed initially, followed by slow contraction due to the activity of myosin motors. Although the characteristic time for viscous behavior was below 1 sec, the amplitude was limited such that it was still possible to neglect it during the traction phase. To confirm this, further analysis need to be conducted, relaxing some of the hypotheses. Overall our experimental setup allows to simultaneously probe 3 different behaviors: elasticity of the peripheral fibers, viscosity within the fiber and the action of motors on long time scales. It could additionally be used to apply a deformation to fibers and let them relax freely (i.e straighten back to their original position). The time scale of this straightening is expected to be similar to the viscoelastic relaxation observed in these experiments.

Chapter 6

Conclusion and Perspectives

6.1 Summary of results

We have examined the organization and mechanical properties of peripheral stress fibers of cells in constrained environments using analytical modeling together with three different experimental approaches: adhesive constraining of cells on glass substrates, traction force microscopy on patterned soft substrates and transverse deformation of isolated fibers using soft cantilevers. In Chapter 3, we have characterized the formation of actin-myosin bridges at the cell periphery, as a geometry-dependent feature occurring above a length maturation threshold of 3-4µm. We explained how this length dependence could come from the conversion of radial myosin-powered forces to tangential forces at cell adhesions. We argued that not only the formation, but also the shape of peripheral arcs is force-dependent, following the well-known Laplace law which states that the interface curvature is equal to the ratio of surface tension to line tension.

In Chapter 4, we examined how the line tension in peripheral arcs was affected by altered cell contractility and found that cells simultaneously swelled and diminished their traction forces when myosin was inhibited. We explained this by a simple model for line tension as a sum of a myosin-dependent active contribution and of a mysoin-independent elastic contribution, and argued that some elasticity is necessary to allow for dynamic shape adaptation. We used this analytical model combined to the dynamic measurements of arc shape and traction forces to estimate the ratio of elastic and active tension in arcs in their native state, confirming that elastic tension is limited while myosin-powered tension is more variable, scaling with cell contractility.

Finally, in Chapter 5, we confirmed that peripheral fibers responded elastically to transverse deformations over short timescales around 1 sec. Above 1 sec, viscous effects lead to further relaxation of the fiber. We did not find any explicit dependence of elasticity on myosin activity, indicating that passive cross-linkers such as α-actinin are likely also central to determining the mechanical properties of stress fibers.

6.2 Discussion

Overall, we have conducted three different types of measurements of line tension in peripheral stress fibers, under contractility inhibition. The first one was based on the combination of traction force microscopy and measurement of arc radius of curvature. The second one was based on small transverse indentations performed with a soft cantilever. Finally, we used the same cantilevers to apply transverse deformations on isolated fibers. How do these measures compare one to another? The order of magnitudes of the line tension are generally the same, though higher tensions were measured with small indentations of arcs, in Chapter 4, section 4.2.2. Looking at the active pre-tension values (λ_a in Chapter 4, and T_0 in Chapter 5) we found once again higher values when tension was measured by indenting arcs (~100nN), and lower ones in isolated fibers (~ 6nN) while, results from traction force microscopy experiments yielded tensions in the intermediate range (~27 nN). While the type of substrate could explain these differences, it is also possible that fiber isolation affects mechanical tension in the fiber. Nonetheless, the decrease of tension following the inhibition of myosin was reproducible in all cases. In Figure 6.1, we compare some of the experimental results obtained with alternative techniques. We observe that, at the concentrations of inhibitor used, tension decreases in all cases, at a similar rate, and that there is about 20% residual tension after treatment. Note though that for isolated fibers (◇ in Figure 6.1), only the decrease of active pre-tension T_0 is plotted, the elastic term is not considered here, which could explain why normalized values during the course of myosin inhibition are higher than for other experiments. The similarity of these results obtained with different techniques supports the overall conclusion, that the total line tension decreases under inhibition of contractility, with one contribution being directly proportional to myosin activity, and the other elastic contribution being dependent on bundle length.

Nevertheless, it should be noted that the estimates of elastic spring constants obtained with each technique are not identical. In isolated fibers, k_1 did never exceed 10nN/μm, which, in terms of stiffness, means $EA = k_1 d$ was between 5nN and 140nN. This corresponds to the lower range of what has been measured in peripheral arcs in Chapter 4, where values above 500nN have been found. One reason for the higher values in the case of

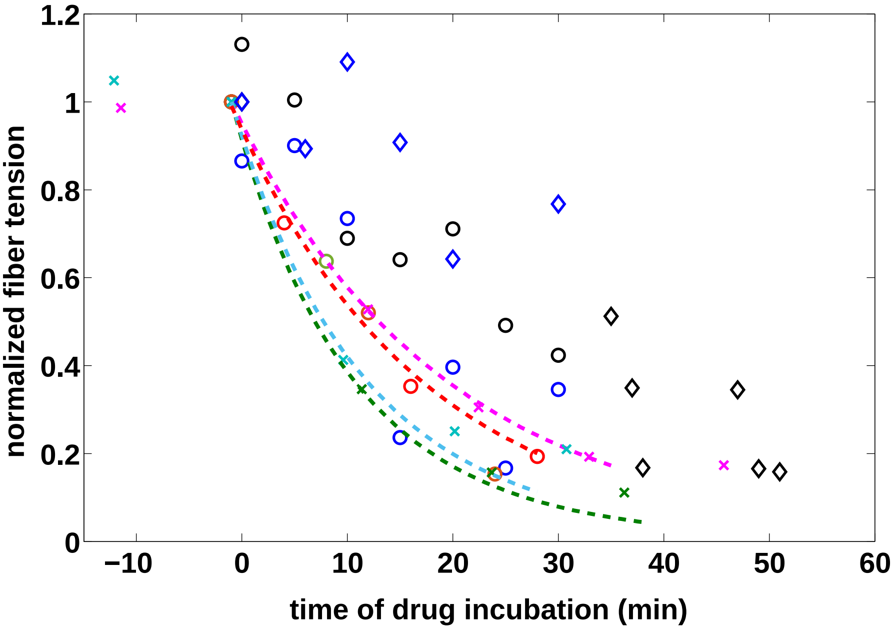

Figure 6.1: Decrease of fiber line tension during myosin inhibition. Fiber tension were normalized to the values measured before inhibition. At time t=0, 10µM Y27632 was added to the medium. 'x' represent values obtained by combining TFM and arc radius measurement. 'o' represent values measured by small indentations of arcs using soft cantilevers. '◇' represent values of tensions measured on isolated fibers (the resulting T_0 from fitting the force-elongation curves). The dashed lines are the results of the numerical simulations with the model described in Chapter 4.

non-isolated arcs could be that the effective bundle cross-section is larger than for isolated bundles. Bundle cross-section is indeed unknown, and though from visualization of actin a single bundle can be distinguished, it does not exclude the possibility that several accumulated bundles contribute to the measured tension. In Chapter 5, the errors in estimation of k_1 come from the fact that the characteristic time scale of viscous behavior is close to the time of traction, leading to a possible understimation of the spring constant. Possibilities to correct for this are being explored, by looking at the traction and relaxation regime in a single fit rather than as two separate regimes.

In Chapter 4, we neglected viscosity in the bundles because the deformation occurred over several tens of minutes, and therefore modeled peripheral bundles as a spring and a motor unit in parallel. In Chapter 5, the timescale of deformations was of seconds, and thus enabled us to simultaneously probe fiber elasticity and fiber viscosity. To analyze our results, a 3-parameter-solid model seemed the most adapted to describe the observed behavior; the action of myosin motors was implicitly considered in the pre-tension term T_0. Thus the overall characterization of a peripheral stress fiber is a combination of a spring in parallel with a motor setting the active pre-tension, together in series with a Kelvin-Voigt-contractile unit accounting for viscous dissipation. These results are summarized up in Figure 6.2.

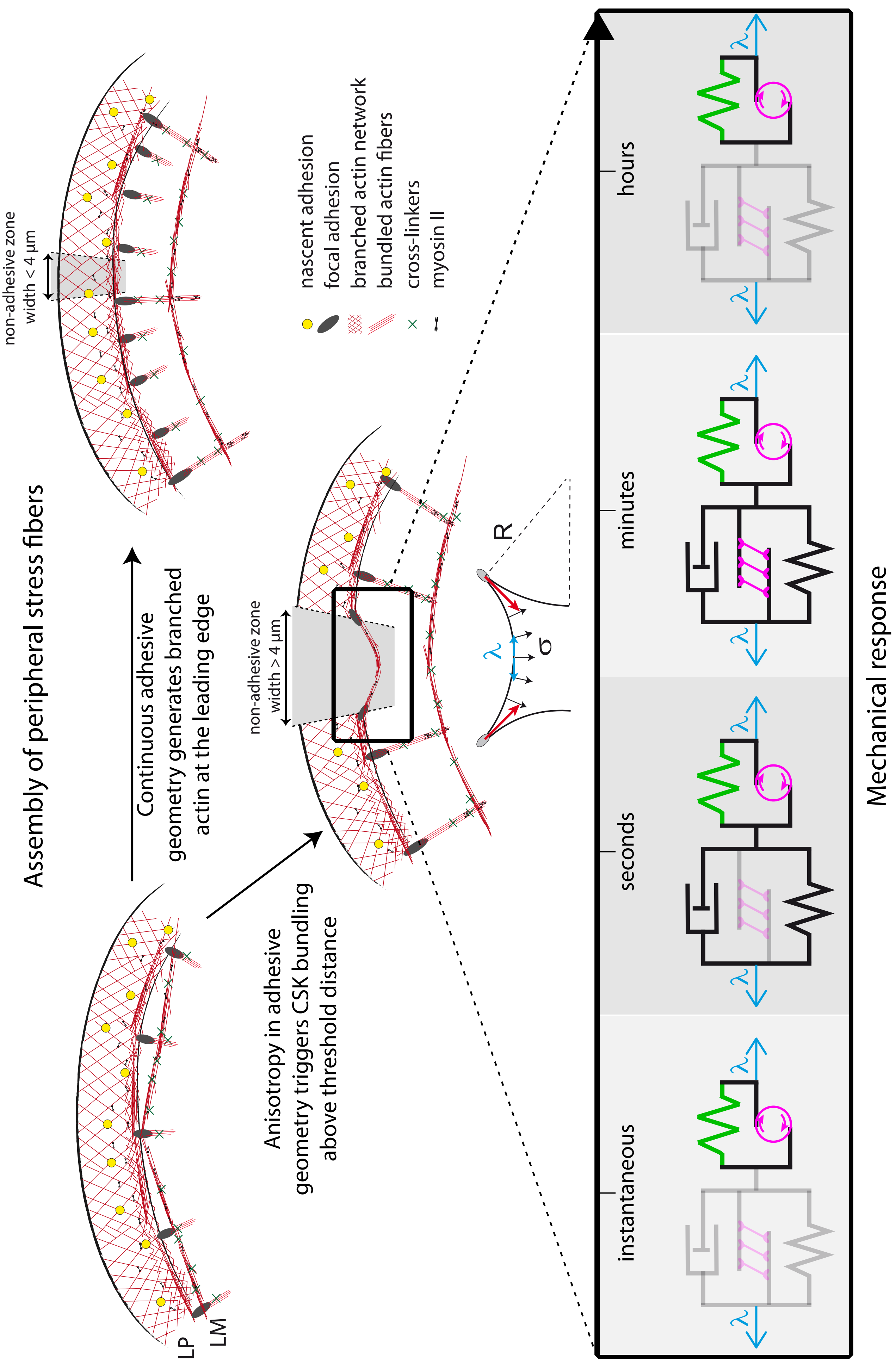
Assembly of peripheral stress fibers
Continuous adhesive geometry generates branched actin at the leading edge
Anisotropy in adhesive geometry triggers CSK bundling above threshold distance
non-adhesive zone width < 4 µm
non-adhesive zone width > 4 µm
LP
LM
nascent adhesion
focal adhesion
branched actin network
bundled actin fibers
cross-linkers
myosin II
R
λ
σ
instantaneous
seconds
minutes
hours
λ
Mechanical response

Figure 6.2: Summary of peripheral SF assembly and mechanical response (legend on page 113)

Figure 6.2: Summary of peripheral stress fiber assembly and mechanical response. (Top) At the leading edge of the cell, branched actin networks form the lamellipodial protrusions (LP). Nascent adhesions form under the LP, and mature to focal complexes (not shown) and then to focal adhesions at the interface with the lamellum (LM). On continuous adhesive substrate or on narrow non-adhesive gaps, the organization of actin remains branched, and radial stress fibers (bundled actin) polymerize at the focal adhesions. Anisotropy imposed by the adhesive geometry or by spreading triggers reorganization of the cytoskeleton (CSK) into bundles tangential to the leading edge above a threshold distance of 4µm (Chapter 4). The radius of curvature R of these peripheral arcs is determined by the ratio of line tension λ and surface tension σ. The tension λ in the arcs can be measured and the response will vary with the timescale and nature of the perturbation. (Bottom) Mechanical model of peripheral stress fiber's response to perturbation. Instantaneous response is determined by an elastic (green) and active tension (magenta motor unit) (Chapter 5, section 5.2.1). On time scale of a few seconds, viscous effects come into play (Chapter 5, section 5.2.2). Relaxation over several seconds to minutes also involves the sliding of myosins on actin filaments (magenta myosins) (Chapter 5, section 5.3.3). Finally over long timescales (tens of minutes to hours), the dominant elements are again a parallel arrangement of elastic and active tension, for example, in response to myosin inhibition (Chapter 4). Active pre-tension and the myosin sliding both come from the myosin motors bound to actin (magenta) and are thus affected by blebbistatin or Y27632 treatment. Elasticity is primarily due to cross-linkers such as α-actinin, though the contribution of myosins to elasticity as passive cross-linkers cannot be entirely ruled out. Viscous dissipation is suspected to come from the friction and dynamic binding/unbinding of the multiple actin-binding proteins.

To conclude, our findings have shown that cytoskeleton remodeling and the formation of specific features such as peripheral arcs are sensitive to the adhesive geometry. The elasticity in these peripheral arcs, and most likely in other stress fibers, enables dynamic adaptation of cell shape to the local tension, in particular in reduced contractility condition. However, the elasticity does not appear to be directly dependent on the presence of myosin. Since the general viscoelastic properties of stress fibers enable a fast response to external perturbations, at least partly independently of myosin activity, one can speculate that they constitute a parallel pathway to regulate cell homeostasis, thereby creating more flexibility to adapt the cell's response to external stimuli. Furthermore, elastic peripheral fibers provide a direct mechanism to relate cell deformation to the cell's mechanical tension, and could therefore be implicated in the dynamic regulation of not only cell shape, but also cell size.

6.3 Perspectives

6.3.1 Combining active and passive force measurements

One issue that has not been addressed so far is that continuous mechanical stimulation of cells may trigger remodeling of the cytoskeleton and of cell-matrix adhesions, for instance, a stiffening of molecular bonds or of stress fibers, and disassembly of adhesions. In order to estimate to what extent cytoskeletal remodeling modifies the force balance in the cell, it would be interesting to combine the active tension measurement technique developed here, based on fiber deformation, with passive force measurements, based on traction force microscopy (by passive measurements, we mean no external perturbation was applied to the cell). In this prospect, our cantilever-based tension measurement method is well suited because it can be in theory used on different substrates, and does not require chemical treatment of cells (as in Deguchi et al. [2006] and Matsui et al. [2013]), thus allowing simultaneous global measurements of cell traction forces. Furthermore, cantilevers can be rendered either anti-adhesive or adhesive (coated with fibronectin), thereby allowing to use different types of simulations.

We therefore set out to build a setup in which cantilever tension measurement can be combined with some traction force microscopy measurements. The objectives were to apply transverse deformations to peripheral fibers and measure how much work was transmitted to the terminating adhesions. Furthermore, testing both fiber indentation with passivated cantilevers and fiber transverse pulling by creating an adhesive contact at the fiber mid-point could give insight into how adhesive complexes alter the fiber's mechanical response and the extent of cytoskeleton remodeling. Although it was not possible to carry out all these experiments, some significant steps were taken in fabricating an adequate experimental setup.

Creating adhesive contact to pull fibers

We first carried out tests on non-deformable PDMS patterns with cantilevers functionalized with fibronectin. Adhesive contacts were created by placing the cantilever against a peripheral fiber for 10-15min. Fibers were then transversally stretched at 1µm/s. Note that fibers were not isolated from the cell in this case. From the platform speed and the cantilever deflection, we could compute the applied deformation and the force on the cantilever, and subsequently analyze the force-extension curves, with a similar theoretical framework as used in Chapter 5, section 5.2.1. An inward force was added in the force balance to account for the resistance of the cytoplasm. To our surprise, the force-extension curves were concave (Figure 6.3), and therefore an elastic tension model did not fit well the experimental data (though still better than a constant tension model). Here we found that less force was needed to elongate the fiber as it was stretched further. It is possible that traction is not fast enough to neglect damping, however adding a damping term in the equation did not yield better results; alternatively, other effects may lead to some fluidization of the fiber or of the cytoplasm. Fluidization of the cytoskeleton has been reported before [Krishnan et al., 2009, Chen et al., 2010, Krishnan et al., 2012] for cells that are submitted to sequential stretching-compressing deformations. In fact, when cells are submitted to stretch-hold or compress-stretch protocols, stiffening or constant stiffness are observed [Wu and Feng, 2015]. In our case, we continuously stretch the fiber

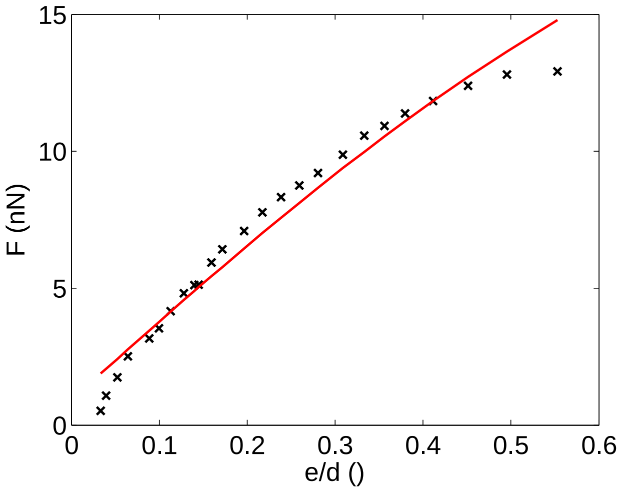

Figure 6.3: Example of force-extension curve for an adhesive cell-cantilever contact. Experimental data ('x', black) and theoretical curve (red line). The axial elongation e was normalized to the half fiber spanning distance d. The k value that was used here was very low at 0.46nN/µm, but as can be noticed, this does not give reproduce the concavity of the experimental curve. Note that allowing negative values for k yields perfect fits, but no physical significance.

until the cantilever breaks free from the cell so this does not meet the previously observed conditions for fiber fluidization. Therefore we suspect that either fluidization of the cytoplasm is involved, or the newly formed adhesion, and the specific geometry of the probed system, which we stretch transversally rather than axially, lead to different response than what has been reported until now. Conducting similar measurements with passivated cantilevers, or on isolated fibers together with inhibition of contractility might help decipher whether the cytoplasm, the motors, or other SF components are responsible for the apparent fluidization.

Experimental setup

To proceed towards simultaneous measurement of active tension and passive forces, we changed the patterns that we had been using so far. Cantilever-based measurements are best done on 3-dimensional patterns to allow for axial movement of the cantilever, without risking disrupting the substrate (especially a soft gel); but the patterns used in previous measurements were too rigid to be deformed by cellular forces. Therefore we turned to PDMS micro-pillar arrays for the passive force measurements. To allow for cantilever maneuverability in the x-y plane, full arrays were not convenient. Instead we designed a mask with sufficient spaces in between cell-sized arrays of pillars. Since traction forces are exerted at the cell periphery, we also used larger inner islands to promote proper cell spreading, surrounded by micro-pillars at the periphery (Figure 6.4). Pillars were molded in 15µm deep Si wafers in order to have spring constants of $k \sim 7$nN/µm. This was the

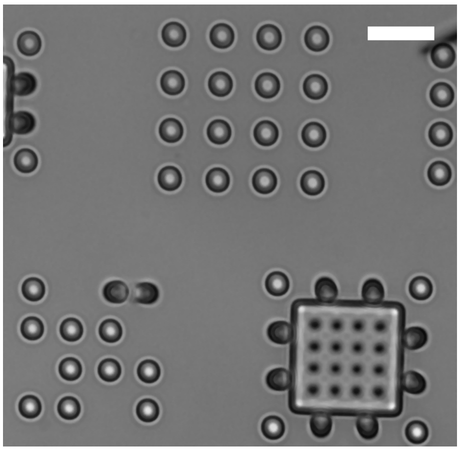

Figure 6.4: Spaced 3-dimensional PDMS patterns. Pillar diameter is 3µm, pillar spacing is 4µm. Near the larger square shaped islands, some pillars have fallen and stick to the neighboring structures. The dark spots in the square island correspond to square holes. These were added so that islands and pillars had similar aspect ratios, to homogenize the depth of etching during Si wafer process. Scale bar, 10µm.

best compromise found between having deformable pillars with a low spring constant, and having pillars with the lowest-aspect ratio for ease of fabrication, given that $k = \frac{3\pi ED^4}{64L^3}$. Lowering the Young modulus of the PDMS was possible to a limited extent by changing the ratio of base to curing agent from 10:1 to 12:1. However, the high aspect ratios of the pillars also led to easy pillar buckling when E was further decreased. These considerations led us to use 15µm high pillars with a 12:1 PDMS ratio. The top surface of the pillars were stamped with fibronectin to promote cell attachment.

Despite testing several cell types, fibroblasts but also smooth muscle cell lines, cells did not sufficiently spread on the pillars, which impeded the implementation of the double force measurement. There are several options that could improve this setup. The size of the pillar arrays need to be increased and the spacing diminished to ensure cell spreading and strong attachment. Then, either a smaller cantilever could be used (though this is also a fabrication challenge), or alternatively, cantilevers which fall on the top of the cell instead of vertically on the side of the cell could be used, thus avoiding maneuvrability problems. Finally other tension measurement techniques, such as magnetic microneedles [Matthews et al., 2004] or even magnetized micro-pillar arrays [Sniadecki et al., 2007], could be more suitable to a double force measurement experimental setup.

6.3.2 Further Outlooks

Our experimental and modeling endeavours have focused on the measurement of active tension and elastic constants in stress fibers, focusing on the role of myosin II. We see several other directions that could complete the study of the formation and maintenance of stress fibers in fibroblasts. First of all, the molecular composition of focal adhesions is known to be extremely dynamic and sensitive to external tension. However, it is not known whether focal adhesions connected to dorsal SF, ventral SF or peripheral arcs are similar. Investigating not only the maturational state of FAs, but also the signaling that follows from FA maturation could bring further light into the myosin-dependent length maturation threshold mechanism. Myosin activity is indeed tightly regulated by several signaling pathways, some of them (such as ROCK) being activated at FAs. Additionally, molecular composition and structure of peripheral arcs could be investigated more closely using super-resolution microscopy with high temporal resolution, in order to have insight into the progression of arc formation, strengthening and turnover. Other biochemical perturbations or genetic tools could be used to test the dynamics of binding/unbinding rates of passive crosslinkers, and estimate the impact of strain-stiffening/softening in crosslinking bonds on mechanical properties. It would also be interesting to compare the response of arcs submitted to other perturbations such as cyclic stretch to those presented here. The viscoelastic model presented here would have to be modified to account for cytoskeletal reorganization and reorientation observed under cyclic stretch. In general, the model and understanding of the mechanical properties of SF would be greatly improved by integrating knowledge of the dynamic remodeling of cytoskeletal components (actin filaments, myosin motors and other cross-linkers), and possible stick-slip effects such as those observed in semi-isolated fibers. Finally, the approach presented in Chapter 4 could be expanded to look at the relation between the 3-dimensional shape of the cell and the traction forces in all directions.

Bibliography

Albert, P. and Schwarz, U. S. Dynamics of Cell Shape and Forces on Micropatterned Substrates Predicted by a Cellular Potts Model. *Biophys. J.*, 106(11):2340–2352, 2014.

Alberts, B. *Molecular biology of the cell.* Garland Science, New York, 4th edition, 2002. ISBN 0815332181 (hardbound) 0815340729 (pbk.).

Alexandrova, A. Y., Arnold, K., Schaub, S., Vasiliev, J. M., Meister, J.-J., Bershadsky, A. D., and Verkhovsky, A. B. Comparative dynamics of retrograde actin flow and focal adhesions: formation of nascent adhesions triggers transition from fast to slow flow. *PLoS One*, 3(9):e3234, 2008.

Ambrosi, D., Duperray, A., Peschetola, V., and Verdier, C. Traction patterns of tumor cells. *Journal of Mathematical Biology*, 58(1-2):163–181, 2009.

Aratyn-Schaus, Y., Oakes, P. W., and Gardel, M. L. Dynamic and structural signatures of lamellar actomyosin force generation. *Mol. Biol. Cell*, 22(8):1330–9, 2011.

Balaban, N. Q., Schwarz, U. S., Riveline, D., Goichberg, P., Tzur, G., Sabanay, I., Mahalu, D., Safran, S. A., Bershadsky, A. D., Addadi, L., and Geiger, B. Force and focal adhesion assembly: a close relationship studied using elastic micropatterned substrates. *Nat. Cell Biol.*, 3(5):466–472, 2001.

Balland, M., Richert, A., and Gallet, F. The dissipative contribution of myosin II in the cytoskeleton dynamics of myoblasts. *Eur. Biophys. J.*, 34(3):255–61, 2005.

Banerjee, S. and Giomi, L. Polymorphism and bistability in adherent cells. *Soft Matter*, 9(21):5251, 2013.

Bangasser, B. L., Rosenfeld, S. S., and Odde, D. J. Determinants of Maximal Force Transmission in a Motor-Clutch Model of Cell Traction in a Compliant Microenvironment. *Biophys. J.*, 105(3):581–592, 2013.

Bernal, R., Pullarkat, P., and Melo, F. Mechanical Properties of Axons. *Phys. Rev. Lett.*, 99(1):018301, 2007.

Bershadsky, A. D., Balaban, N. Q., and Geiger, B. Adhesion-Dependent Cell Mechanosensitivity. *Annu. Rev. Cell Dev. Biol.*, 19(1):677–695, 2003.

Besser, A. and Schwarz, U. S. Coupling biochemistry and mechanics in cell adhesion: a model for inhomogeneous stress fiber contraction. *New J. Phys.*, 9(11):425–425, 2007.

Besser, A., Colombelli, J., Stelzer, E. H. K., and Schwarz, U. S. Viscoelastic response of contractile filament bundles. *Phys. Rev. E*, 83(5):051902, 2011.

Bischofs, I., Schmidt, S., and Schwarz, U. S. Effect of Adhesion Geometry and Rigidity on Cellular Force Distributions. *Phys. Rev. Lett.*, 103(4):1–4, 2009.

Bischofs, I. B., Klein, F., Lehnert, D., Bastmeyer, M., and Schwarz, U. S. Filamentous Network Mechanics and Active Contractility Determine Cell and Tissue Shape. *Biophys. J.*, 95(7):3488–3496, 2008.

Brown, R., Prajapati, R., McGrouther, D., Yannas, I., and Eastwood, M. Tensional homeostasis in dermal fibroblasts: mechanical responses to mechanical loading in three-dimensional substrates. *J. Cell Physiol.*, 175(3):323–332, 1998.

Burnette, D. T., Manley, S., Sengupta, P., Sougrat, R., Davidson, M. W., Kachar, B., and Lippincott-Schwartz, J. A role for actin arcs in the leading-edge advance of migrating cells. *Nat. Cell Biol.*, 13(4):371–381, 2011.

Burnette, D. T., Shao, L., Ott, C., Pasapera, A. M., Fischer, R. S., Baird, M. A., Der Loughian, C., Delanoe-Ayari, H., Paszek, M. J., Davidson, M. W., Betzig, E., and Lippincott-Schwartz, J. A contractile and counterbalancing adhesion system controls the 3D shape of crawling cells. *J. Cell Biol.*, 205(1):83–96, 2014.

Burridge, K. and Wittchen, E. S. The tension mounts: Stress fibers as force-generating mechanotransducers. *J. Cell Biol.*, 200(1):9–19, 2013.

Butler, J. P., Tolić-Nø rrelykke, I. M., Fabry, B., and Fredberg, J. J. Traction fields, moments, and strain energy that cells exert on their surroundings. *Am. J. Physiol. Cell Physiol.*, 282:C595–C605, 2002.

Cai, Y., Rossier, O., Gauthier, N. C., Biais, N., Fardin, M. A., Zhang, X., Miller, L. W., Ladoux, B., Cornish, V. W., and Sheetz, M. P. Cytoskeletal coherence requires myosin-IIA contractility. *J. Cell Sci.*, 123(3):413–423, 2010.

Chan, C. E. and Odde, D. J. Traction dynamics of filopodia on compliant substrates. *Science (80-.).*, 322(5908):1687–91, 2008.

Chaudhuri, O., Parekh, S. H., and Fletcher, D. A. Reversible stress softening of actin networks. *Nature*, 445(7125):295–298, 2007.

Chen, C., Krishnan, R., Zhou, E., Ramachandran, A., Tambe, D., Rajendran, K., Adam, R. M., Deng, L., and Fredberg, J. J. Fluidization and resolidification of the human bladder smooth muscle cell in response to transient stretch. *PloS one*, 5(8):e12035, 2010.

Chen, C. S., Mrkisch, M., Huang, S., Whitesides, G. M., and Ingber, D. E. Geometric Control of Cell Life and Death. *Science (80-.).*, 276(5317):1425–1428, 1997.

Chicurel, M. E., Chen, C. S., and Ingber, D. E. Cellular control lies in the balance of forces. *Curr. Opin. Cell Biol.*, 10(2):232–239, 1998.

Choi, C. K., Vicente-Manzanares, M., Zareno, J., Whitmore, L. a., Mogilner, A., and Horwitz, A. R. Actin and alpha-actinin orchestrate the assembly and maturation of nascent adhesions in a myosin II motor-independent manner. *Nat. Cell Biol.*, 10(9): 1039–50, 2008.

Clark, A. G. and Paluch, E. Mechanics and regulation of cell shape during the cell cycle. In *Results Probl. Cell Differ.*, volume 53, pages 31–73. Springer Berlin / Heidelberg, 2011. ISBN 978-3-642-19064-3.

Colombelli, J., Besser, A., Kress, H., Reynaud, E. G., Girard, P., Caussinus, E., Haselmann, U., Small, J. V., Schwarz, U. S., and Stelzer, E. H. K. Mechanosensing in actin stress fibers revealed by a close correlation between force and protein localization. *J. Cell Sci.*, 122(Pt 10):1665–79, 2009.

Coyer, S. R., Singh, A., Dumbauld, D. W., Calderwood, D. A., Craig, S. W., Delamarche, E., and García, A. J. Nanopatterning reveals an ECM area threshold for focal adhesion assembly and force transmission that is regulated by integrin activation and cytoskeleton tension. *J. Cell Sci.*, 125(Pt 21):5110–23, 2012.

Deguchi, S. and Sato, M. Biomechanical properties of actin stress fibers of non-motile cells. *Biorheology*, 46(2):93–105, 2009.

Deguchi, S., Ohashi, T., and Sato, M. Evaluation of tension in actin bundle of endothelial cells based on preexisting strain and tensile properties measurements. *Mol. Cell. Biomech.*, 2:125–133, 2005.

Deguchi, S., Ohashi, T., and Sato, M. Tensile properties of single stress fibers isolated from cultured vascular smooth muscle cells. *J. Biomech.*, 39(14):2603–2610, 2006.

Deguchi, S., Matsui, T. S., and Iio, K. The position and size of individual focal adhesions are determined by intracellular stress-dependent positive regulation. *Cytoskeleton (Hoboken).*, 68(11):639–51, 2011.

Dembo, M. and Wang, Y. L. Stresses at the cell-to-substrate interface during locomotion of fibroblasts. *Biophys. J.*, 76(4):2307–16, 1999.

Discher, D. E., Janmey, P., and Wang, Y.-L. Tissue cells feel and respond to the stiffness of their substrate. *Science*, 310(5751):1139–43, 2005.

Engler, A. J., Sen, S., Sweeney, H. L., and Discher, D. E. Matrix elasticity directs stem cell lineage specification. *Cell*, 126(4):677–89, 2006.

Fletcher, D. A. and Mullins, R. D. Cell mechanics and the cytoskeleton. *Nature*, 463 (7280):485–492, 2010.

Fouchard, J., Bimbard, C., Bufi, N., Durand-Smet, P., Proag, A., Richert, A., Cardoso, O., and Asnacios, A. Three-dimensional cell body shape dictates the onset of traction force generation and growth of focal adhesions. *Proc. Natl. Acad. Sci. U. S. A.*, 111 (36):13075–13080, 2014.

Friedland, J. C., Lee, M. H., and Boettiger, D. Mechanically Activated Integrin Switch Controls alpha(5)beta(1) Function. *Science (80-.).*, 323(5914):642–644, 2009.

Fung, Y. C. *Foundations of Solid Mechanics.* Prentice-Hall, Inc., Englewood Cliffs, NJ, USA, 1965.

Gardel, M. L., Schneider, I. C., Yvonne Aratyn-Schaus, and Waterman, C. M. Mechanical Integration of Actin and Adhesion Dynamics in Cell Migration. *Annual Reviews of Cell and Developmental Biology*, 26:315–333, 2010.

Gauthier, N. C., Masters, T. A., and Sheetz, M. P. Mechanical feedback between membrane tension and dynamics. *Trends Cell Biol.*, 22(10):527–35, 2012.

Geiger, B., Bershadsky, A. D., Pankov, R., and Yamada, K. M. Transmembrane crosstalk between the extracellular matrix and the cytoskeleton. *Nat. Rev. - Mol. Cell Biol.*, 2 (11), 2001.

Geiger, B., Spatz, J. P., and Bershadsky, A. D. Environmental sensing through focal adhesions. *Nat. Rev. - Mol. Cell Biol.*, 10(1):21–33, 2009.

Ghibaudo, M., Saez, A., Trichet, L., Xayaphoummine, A., Browaeys, J., Silberzan, P., Buguin, A., and Ladoux, B. Traction forces and rigidity sensing regulate cell functions. *Soft Matter*, 4(9):1836, 2008.

Graner, F. and Glazier, J. A. Simulation of Biological Cell Sorting Using a 2-Dimensional Extended Potts-Model. *Phys. Rev. Lett.*, 69(13):2013–2016, 1992.

Guillou, H., Depraz-Depland, A., Planus, E., Vianay, B., Chaussy, J., Grichine, A., Albigès-Rizo, C., and Block, M. R. Lamellipodia nucleation by filopodia depends on integrin occupancy and downstream Rac1 signaling. *Exp. Cell Res.*, 314(3):478–488, 2008.

Guthardt Torres, P., Bischofs, I., and Schwarz, U. S. Contractile network models for adherent cells. *Phys. Rev. E*, 85(1):1–13, 2012.

Han, S. J., Bielawski, K. S., Ting, L. H. H., Rodriguez, M. L. L., and Sniadecki, N. J. J. Decoupling Substrate Stiffness , Spread Area , and Micropost Density : A Close Spatial Relationship between Traction Forces and Focal Adhesions. *Biophys. J.*, 103(4): 640–648, 2012.

Harris, A. K., Wild, P., and Stopak, D. Silicone rubber substrata: a new wrinkle in the study of cell locomotion. *Science*, 208:177–179, 1980.

Hill, A. V. The heat of shortening and the dynamic constants of muscle. *Proceedings of the Royal Society of London. Series B, Biological Sciences*, 126(843):pp. 136–195, 1938.

Hoffman, B. D., Grashoff, C., and Schwartz, M. A. Dynamic molecular processes mediate cellular mechanotransduction. *Nature*, 475(7356):316–323, 2011.

Hotulainen, P. and Lappalainen, P. Stress fibers are generated by two distinct actin assembly mechanisms in motile cells. *J. Cell Biol.*, 173(3):383–394, 2006.

Howard, J. *Mechanics of motor proteins and the cytoskeleton.* Sinauer Associates, Inc, Sunderland, MA, first edition, 2001.

Kanchanawong, P., Shtengel, G., Pasapera, A. M., Ramko, E. B., Davidson, M. W., Hess, H. F., and Waterman, C. M. Nanoscale architecture of integrin-based cell adhesions. *Nature*, 468(7323):580–4, 2010.

Kaunas, R., Hsu, H.-J., and Deguchi, S. Sarcomeric model of stretch-induced stress fiber reorganization. *Cell Health Cytoskelet.*, 3:13, 2010.

Kolega, J. Asymmetric Distribution of Myosin IIB in Migrating Endothelial Cells Is Regulated by a Rho-dependent Kinase and Contributes to Tail Retraction. *Mol. Biol. Cell*, 14(December):4745–4757, 2003.

Kong, F., García, A. J., Mould, A. P., Humphries, M. J., and Zhu, C. Demonstration of catch bonds between an integrin and its ligand. *The Journal of cell biology*, 185(7): 1275–1284, 2009.

Kraning-Rush, C. M., Carey, S. P., Califano, J. P., and Reinhart-King, C. A. Chapter 6: Quantifying traction stresses in adherent cells. In Asthagiri, A. R. and Arkin, A. P., editors, *Computational Methods Cell Biology*, volume 110 of *Methods in Cell Biology*, pages 139–78. Academic Press, 2012.

Krishnan, R., Park, C. Y., Lin, Y.-C., Mead, J., Jaspers, R. T., Trepat, X., Lenormand, G., Tambe, D., Smolensky, A. V., Knoll, A. H., Butler, J. P., and Fredberg, J. J. Reinforcement versus fluidization in cytoskeletal mechanoresponsiveness. *PloS one*, 4 (5):e5486, 2009.

Krishnan, R., Canović, E. P., Iordan, A. L., Rajendran, K., Manomohan, G., Pirentis, A. P., Smith, M. L., Butler, J. P., Fredberg, J. J., and Stamenović, D. Fluidization, resolidification, and reorientation of the endothelial cell in response to slow tidal stretches. *Am. J. of Physiology-Cell Physiology*, 303(4):C368–C375, 2012.

Kumar, S., Maxwell, I. Z., Heisterkamp, A., Polte, T. R., Lele, T. P., Salanga, M., Mazur, E., and Ingber, D. E. Viscoelastic retraction of single living stress fibers and its impact on cell shape, cytoskeletal organization, and extracellular matrix mechanics. *Biophys. J.*, 90(10):3762–3773, 2006.

Labouesse, C., Gabella, C., Vianay, B., Verkhovsky, A. B., and Meister, J.-J. In situ measurements of the mechanical properties of semi-isolated stress fibers. *in preparation.*

Labouesse, C., Verkhovsky, A. B., Meister, J.-J., Gabella, C., and Vianay, B. Cell shape dynamics reveal balance of elasticity and contractility in peripheral arcs. *Biophys. J.*, 108(10):2437–2447, 2015.

Lacayo, C. I., Pincus, Z., VanDuijn, M. M., Wilson, C. A., Fletcher, D. A., Gertler, F. B., Mogilner, A., and Theriot, J. A. Emergence of large-scale cell morphology and movement from local actin filament growth dynamics. *PLoS Biol.*, 5(9):e233, 2007.

Landau, L. D. and Lifschitz, E. M. *Theory of Elasticity*, volume 7 of *Course of Theoretical Physics*. Pergamon Press, Oxford, UK, third edition, 1986.

Lecuit, T. and Lenne, P. F. Cell surface mechanics and the control of cell shape, tissue patterns and morphogenesis. *Nat. Rev. - Mol. Cell Biol.*, 8(8):633–644, 2007.

Lee, J., Leonard, M., Oliver, T., Ishihara, A., and Jacobson, K. Traction forces generated by locomoting keratocytes. *The Journal of cell biology*, 127(6):1957–1964, 1994.

Lehnert, D., Wehrle-Haller, B., David, C., Weiland, U., Ballestrem, C., Imhof, B. A., and Bastmeyer, M. Cell behaviour on micropatterned substrata: limits of extracellular matrix geometry for spreading and adhesion. *J. Cell Sci.*, 117(Pt 1):41–52, 2004.

Lemmon, C. A. and Romer, L. H. A Predictive Model of Cell Traction Forces Based on Cell Geometry. *Biophys. J.*, 99(9):L78–L80, 2010.

Lenz, M., Thoresen, T., Gardel, M. L., and Dinner, A. R. Contractile Units in Disordered Actomyosin Bundles Arise from F-Actin Buckling. *Phys. Rev. Lett.*, 108(23):238107, 2012.

Loosli, Y., Vianay, B., Luginbuehl, R., and Snedeker, J. G. Numerically bridging lamellipodial and filopodial activity during cell spreading reveals a potentially novel trigger of focal adhesion maturation. *Integr. Biol.*, 4:508–521, 2012.

Loosli, Y., Labouesse, C., Luginbuehl, R., Meister, J.-J., Snedeker, J. G., and Vianay, B. An actin length threshold regulates adhesion maturation at the lamellipodium/lamellum interface. *Integr. Biol.*, 5(6):865–76, 2013.

Lu, L., Feng, Y., Hucker, W. J., Oswald, S. J., Longmore, G. D., and Yin, F. C.-P. Actin stress fiber pre-extension in human aortic endothelial cells. *Cell Motil. Cytoskeleton*, 65 (4):281–94, 2008.

Mandal, K., Wang, I., Vitiello, E., Orellana, L. A. C., and Balland, M. Cell dipole behaviour revealed by ECM sub-cellular geometry. *Nat. Commun.*, 5:5749, 2014.

Marcq, P., Yoshinaga, N., and Prost, J. Rigidity Sensing Explained by Active Matter Theory. *Biophys. J.*, 101(6):L33–L35, 2011.

Martens, J. C. and Radmacher, M. Softening of the actin cytoskeleton by inhibition of myosin II. *Pflugers Arch. Eur. J. Physiol.*, 456:95–100, 2008.

Matsui, T. S., Sato, M., and Deguchi, S. High extensibility of stress fibers revealed by in vitro micromanipulation with fluorescence imaging. *Biochem. Biophys. Res. Commun.*, 434(3):444–8, 2013.

Matthews, B. D., Overby, D. R., Alenghat, F. J., Karavitis, J., Numaguchi, Y., Allen, P. G., and Ingber, D. E. Mechanical properties of individual focal adhesions probed with a magnetic microneedle. *Biochem. Biophys. Res. Commun.*, 313(3):758–764, 2004.

MBInfo contributors, Mechanobiology Institute, National University of Singapore. Mbinfo wiki, 2012. URL `http://www.mechanobio.info/`.

Michel, R., Peschetola, V., Bedessem, B., Etienne, J., Ambrosi, D., Duperray, A., and Verdier, C. Inverse problems for the determination of traction forces by cells on a substrate: a comparison of two methods. *Computer Methods in Biomechanics and Biomedical Engineering*, 15(sup1):27–29, 2012.

Nicolas, A., Geiger, B., and Safran, S. A. Cell mechanosensitivity controls the anisotropy of focal adhesions. *Proc. Natl. Acad. Sci. U. S. A.*, 101:12520–12525, 2004.

Nicolas, A., Besser, A., and Safran, S. a. Dynamics of cellular focal adhesions on deformable substrates: consequences for cell force microscopy. *Biophys. J.*, 95(2):527–39, 2008.

Nijenhuis, N., Zhao, X., Carisey, A., Ballestrem, C., and Derby, B. Article Combining AFM and Acoustic Probes to Reveal Changes in the Elastic Stiffness Tensor of Living Cells. *Biophysj*, 107(7):1502–1512, 2014.

Oakes, P. W. and Gardel, M. L. Stressing the limits of focal adhesion mechanosensitivity. *Curr. Opin. Cell Biol.*, 30(1):68–73, 2014.

Oakes, P. W., Beckham, Y., Stricker, J., and Gardel, M. L. Tension is required but not sufficient for focal adhesion maturation without a stress fiber template. *J. Cell Biol.*, 196(3):363–374, 2012.

Oakes, P. W., Banerjee, S., Marchetti, M. C., and Gardel, M. L. Geometry Regulates Traction Stresses in Adherent Cells. *Biophys. J.*, 107(4):825–833, 2014.

Parker, K. K., Brock, A. L., Brangwynne, C., Mannix, R. J., Wang, N., Ostuni, E., Geisse, N. a., Adams, J. C., Whitesides, G. M., and Ingber, D. E. Directional control of lamellipodia extension by constraining cell shape and orienting cell tractional forces. *FASEB J.*, 16(10):1195–204, 2002.

Parsons, J. T., Horwitz, A. R., and Schwartz, M. A. Cell adhesion: integrating cytoskeletal dynamics and cellular tension. *Nat. Rev. - Mol. Cell Biol.*, 11(9):633–643, 2010.

Paul, R., Heil, P., Spatz, J. P., and Schwarz, U. S. Propagation of Mechanical Stress through the Actin Cytoskeleton toward Focal Adhesions: Model and Experiment. *Biophys. J.*, 94(4):1470–1482, 2008.

Pelham, R. J. and Wang, Y.-l. High resolution detection of mechanical forces exerted by locomoting fibroblasts on the substrate. *Mol. Biol. Cell*, 10(4):935–945, 1999.

Pellegrin, S. and Mellor, H. Actin stress fibres. *J. Cell Sci.*, 120(20):3491–3499, 2007.

Peterson, L. J., Rajfur, Z., Maddox, A. S., Freel, C. D., Chen, Y., Edlund, M., Otey, C., and Burridge, K. Simultaneous Stretching and Contraction of Stress Fibers In Vivo. *Mol. Biol. Cell*, 15(July):3497–3508, 2004.

Piacentini, N., Verkhovsky, A. B., Gabella, C., Meister, J.-J., and Vianay, B. Ultra-soft cantilevers and 3-D micro-patterned substrates for contractile bundle tension measurement in living cells. *Lab Chip*, 14(14):2539–47, 2014.

Piel, M. and Théry, M. *Micropatterning in Cell Biology, Part C*, volume 121 of *Methods in Cell Biology*. Elsevier, 1st edition, 2014. ISBN 9780128003374.

Pollard, T. D. Regulation of actin filament assembly by Arp2/3 complex and formins. *Annu. Rev. Biophys. Biomol. Struct.*, 36:451–477, 2007.

Pollard, T. D. and Borisy, G. G. Cellular motility driven by assembly and disassembly of actin filaments. *Cell*, 112(4):453–465, 2003.

Prager-Khoutorsky, M., Lichtenstein, A., Krishnan, R., Rajendran, K., Mayo, A., Kam, Z., Geiger, B., and Bershadsky, A. D. Fibroblast polarization is a matrix-rigidity-dependent process controlled by focal adhesion mechanosensing. *Nat. Cell Biol.*, 13(12):1457–1465, 2011.

Raffel, M., Willert, C. E., Wereley, S. T., and Kompenhans, J. *Particle Image Velocimetry*. Springer-Verlag, Berlin, Heidelberg, 2nd edition, 2007. ISBN 978-3-540-72308-0.

Rape, A. D., Guo, W.-H., and Wang, Y.-L. The regulation of traction force in relation to cell shape and focal adhesions. *Biomaterials*, 32(8):2043–51, 2011.

Reinhart-King, C. A., Dembo, M., and Hammer, D. A. The dynamics and mechanics of endothelial cell spreading. *Biophys. J.*, 89(1):676–689, 2005.

Reymann, A.-C., Martiel, J.-L., Cambier, T., Blanchoin, L., Boujemaa-Paterski, R., and Théry, M. Nucleation geometry governs ordered actin networks structures. *Nat. Mater.*, 9(10):827–32, 2010.

Reymann, A.-c., Boujemaa-Paterski, R., Martiel, J.-L., Guérin, C., Cao, W., Chin, H. F., De la Cruz, E. M., Théry, M., and Blanchoin, L. Actin Network Architecture Can Determine Myosin Motor Activity. *Science (80-.).*, 336:1310–1314, 2012.

Riveline, D., Zamir, E., Balaban, N. Q., Schwarz, U. S., Ishizaki, T., Narumiya, S., Kam, Z., Geiger, B., and Bershadsky, A. D. Focal contacts as mechanosensors: externally applied local mechanical force induces growth of focal contacts by an mDia1-dependent and ROCK-independent mechanism. *J. Cell Biol.*, 153(6):1175–1186, 2001.

Rosenfeld, S. S., Xing, J., Chen, L.-Q., and Sweeney, H. L. Myosin iib is unconventionally conventional. *Journal of Biological Chemistry*, 278(30):27449–27455, 2003.

Rossier, O. M., Gauthier, N., Biais, N., Vonnegut, W., Fardin, M. A., Avigan, P., Heller, E. R., Mathur, A., Ghassemi, S., Koeckert, M. S., Hone, J. C., and Sheetz, M. P. Force generated by actomyosin contraction builds bridges between adhesive contacts. *Embo J.*, 29(6):1055–1068, 2010.

Sabass, B., Gardel, M. L., Waterman, C. M., and Schwarz, U. S. High resolution traction force microscopy based on experimental and computational advances. *Biophys. J.*, 94 (1):207–20, 2008.

Sakamoto, T., Limouze, J., Combs, C. a., Straight, A. F., and Sellers, J. R. Blebbistatin, a myosin II inhibitor, is photoinactivated by blue light. *Biochemistry*, 44(2):584–8, 2005.

Schwarz, U. S. and Gardel, M. L. United we stand: integrating the actin cytoskeleton and cell-matrix adhesions in cellular mechanotransduction. *J. Cell Sci.*, 125(Pt 13):3051–60, 2012.

Schwarz, U. S., Balaban, N. Q., Riveline, D., Bershadsky, A. D., Geiger, B., and Safran, S. A. Calculation of forces at focal adhesions from elastic substrate data: the effect of localized force and the need for regularization. *Biophys. J.*, 83(3):1380–94, 2002.

Schwarz, U. S., Erdmann, T., and Bischofs, I. Focal adhesions as mechanosensors: the two-spring model. *Biosystems.*, 83(2-3):225–32, 2006.

Scientific Volume Imaging. Huygens remote manager, 2012. URL `http://www.svi.nl`.

Senju, Y. and Miyata, H. The Role of Actomyosin Contractility in the Formation and Dynamics of Actin Bundles During Fibroblast Spreading. *J. Biochem.*, 145(2):137–150, 2009.

Shemesh, T., Verkhovsky, A. B., Svitkina, T. M., Bershadsky, A. D., and Kozlov, M. M. Role of focal adhesions and mechanical stresses in the formation and progression of the lamellipodium-lamellum interface. *Biophys. J.*, 97(5):1254–1264, 2009.

Shemesh, T., Bershadsky, A. D., and Kozlov, M. M. Physical Model for Self-Organization of Actin Cytoskeleton and Adhesion Complexes at the Cell Front. *Biophys. J.*, 102(8): 1746–1756, 2012.

Smith, M. A., Blankman, E., Gardel, M. L., Luettjohann, L., Waterman, C. M., and Beckerle, M. C. A zyxin-mediated mechanism for actin stress fiber maintenance and repair. *Dev. Cell*, 19(3):365–76, 2010.

Sniadecki, N. J., Anguelouch, A., Yang, M. T., Lamb, C. M., Liu, Z., Kirschner, S. B., Liu, Y., Reich, D. H., and Chen, C. S. Magnetic microposts as an approach to apply forces to living cells. *Proc. Natl. Acad. Sci. U. S. A.*, 104(37):14553–8, 2007.

Straight, A. F., Cheung, A., Limouze, J., Chen, I., Westwood, N. J., Sellers, J. R., and Mitchison, T. J. Dissecting temporal and spatial control of cytokinesis with a myosin ii inhibitor. *Science*, 299(5613):1743–1747, 2003.

Stricker, J., Sabass, B., Schwarz, U. S., and Gardel, M. L. Optimization of traction force microscopy for micron-sized focal adhesions. *J. Phys. Condens. Matter*, 22(19):194104, 2010.

Stricker, J., Aratyn-Schaus, Y., Oakes, P. W., and Gardel, M. L. Spatiotemporal constraints on the force-dependent growth of focal adhesions. *Biophys. J.*, 100(12):2883–93, 2011.

Svitkina, T., Verkhovsky, A., McQuade, K., and Borisy, G. Analysis of the actin-myosin II system in fish epidermal keratocytes: mechanism of cell body translocation. *J. Cell Biol.*, 139(2):397, 1997.

Tan, J. L., Tien, J., Pirone, D. M., Gray, D. S., Bhadriraju, K., and Chen, C. S. Cells lying on a bed of microneedles: An approach to isolate mechanical force. *Proc. Natl. Acad. Sci.*, 100(4):1484–1489, 2003.

Tanner, K., Boudreau, A., Bissell, M. J., and Kumar, S. Dissecting regional variations in stress fiber mechanics in living cells with laser nanosurgery. *Biophys. J.*, 99(9):2775–83, 2010.

Tee, S.-Y., Fu, J., Chen, C., and Janmey, P. A. Cell Shape and Substrate Rigidity Both Regulate Cell Stiffness. *Biophys. J.*, 100(5):L25–L27, 2011.

Théry, M. Micropatterning as a tool to decipher cell morphogenesis and functions. *J. Cell Sci.*, 123(Pt 24):4201–4213, 2010.

Théry, M., Pépin, A., Dressaire, E., Chen, Y., and Bornens, M. Cell distribution of stress fibres in response to the geometry of the adhesive environment. *Cell Motil. Cytoskeleton*, 63(6):341–55, 2006a.

Théry, M., Racine, V., Piel, M., Pépin, A., Dimitrov, A., Chen, Y., Sibarita, J.-B., and Bornens, M. Anisotropy of cell adhesive microenvironment governs cell internal organization and orientation of polarity. *Proc. Natl. Acad. Sci. U. S. A.*, 103(52):19771–6, 2006b.

Thoresen, T., Lenz, M., and Gardel, M. L. Reconstitution of contractile actomyosin bundles. *Biophys. J.*, 100(11):2698–705, 2011.

Tinevez, J.-Y., Schulze, U., Salbreux, G., Roensch, J., Joanny, J.-F., and Paluch, E. Role of cortical tension in bleb growth. *Proc. Natl. Acad. Sci. U. S. A.*, 106(44):18581–6, 2009.

Tojkander, S., Gateva, G., and Lappalainen, P. Actin stress fibers - assembly, dynamics and biological roles. *J. Cell Sci.*, 125(Pt 8):1855–64, 2012.

Tse, J. R. and Engler, A. J. Preparation of hydrogel substrates with tunable mechanical properties. *Curr. Protoc. cell Biol.*, Chapter 10(June):Unit 10.16, 2010.

Tseng, Q. *Study of multicellular architecture with controlled microenvironment.* PhD thesis, Université de Grenoble, 2011.

Tseng, Q., Wang, I., Duchemin-Pelletier, E., Azioune, A., Carpi, N., Gao, J., Filhol, O., Piel, M., Théry, M., and Balland, M. A new micropatterning method of soft substrates reveals that different tumorigenic signals can promote or reduce cell contraction levels. *Lab Chip*, 11(13):2231–40, 2011. URL `https://sites.google.com/site/qingzongtseng/tfm`.

Tseng, Q., Duchemin-Pelletier, E., Deshiere, A., Balland, M., Guillou, H., Filhol, O., and Théry, M. Spatial organization of the extracellular matrix regulates cell-cell junction positioning. *Proc. Natl. Acad. Sci. U. S. A.*, 109(5):1506–11, 2012.

Vianay, B., Kafer, J., Planus, E., Block, M. R., Graner, F., and Guillou, H. Single Cells Spreading on a Protein Lattice Adopt an Energy Minimizing Shape. *Phys. Rev. Lett.*, 105(12):–, 2010.

Vicente-Manzanares, M., Choi, C. K., and Horwitz, A. R. Integrins in cell migration – the actin connection. *Journal of Cell Science*, 122(2):199–206, 2009a.

Vicente-Manzanares, M., Ma, X., Adelstein, R. S., and Horwitz, A. R. Non-muscle myosin II takes centre stage in cell adhesion and migration. *Nat. Rev. - Mol. Cell Biol.*, 10(11): 778–90, 2009b.

Vignaud, T., Blanchoin, L., and Théry, M. Directed cytoskeleton self-organization. *Trends Cell Biol.*, 22(12):671–82, 2012.

Walcott, S., Kim, D.-h., Wirtz, D., and Sun, S. X. Nucleation and Decay Initiation Are the Stiffness-Sensitive Phases of Focal Adhesion Maturation. *Biophys. J.*, 101(12): 2919–2928, 2011.

Webster, K. D., Ng, W. P., and Fletcher, D. A. Tensional Homeostasis in Single Fibroblasts. *Biophys. J.*, 107(1):146–155, 2014.

Wolfenson, H., Henis, Y. I., Geiger, B., and Bershadsky, A. D. The heel and toe of the cell's foot: A multifaceted approach for understanding the structure and dynamics of focal adhesions. *Cell Motil. Cytoskeleton*, 66(11):1017–1029, 2009.

Wolfenson, H., Bershadsky, A. D., Henis, Y. I., and Geiger, B. Actomyosin-generated tension controls the molecular kinetics of focal adhesions. *J. Cell Sci.*, 124(Pt 9):1425–32, 2011.

Wu, T. and Feng, J. J. A Biomechanical Model for Fluidization of Cells under Dynamic Strain. *Biophys. J.*, 108(1):43–52, 2015.

Xu, J., Tseng, Y., and Wirtz, D. Strain hardening of actin filament networks. Regulation by the dynamic cross-linking protein alpha-actinin. *J. Biol. Chem.*, 275(46):35886–92, 2000.

Yam, P. T., Wilson, C. A., Ji, L., Hebert, B., Barnhart, E. L., Dye, N. A., Wiseman, P. W., Danuser, G., and Theriot, J. A. Actin-myosin network reorganization breaks symmetry at the cell rear to spontaneously initiate polarized cell motility. *J. Cell Biol.*, 178(7):1207–21, 2007.

Yeung, T., Georges, P. C., Flanagan, L. A., Marg, B., Ortiz, M., Funaki, M., Zahir, N., Ming, W., Weaver, V., and Janmey, P. A. Effects of substrate stiffness on cell morphology, cytoskeletal structure, and adhesion. *Cell motility and the cytoskeleton*, 60 (1):24–34, 2005.

Yip, A. K., Iwasaki, K., Ursekar, C., Machiyama, H., Saxena, M., Chen, H., Harada, I., Chiam, K.-H., and Sawada, Y. Cellular response to substrate rigidity is governed by either stress or strain. *Biophys. J.*, 104(1):19–29, 2013.

Yoshinaga, N. and Marcq, P. Contraction of cross-linked actomyosin bundles. *Phys. Biol.*, 9(4):046004, 2012.

Zemel, A., Rehfeldt, F., Brown, A. E. X., Discher, D. E., and Safran, S. A. Cell shape, spreading symmetry, and the polarization of stress-fibers in cells. *J. Physics-Condensed Matter*, 22(19):–, 2010a.

Zemel, A., Rehfeldt, F., Brown, A. E. X., Discher, D. E., and Safran, S. A. Optimal matrix rigidity for stress-fibre polarization in stem cells. *Nat Phys*, 6(6):468–473, 2010b.

Céline LABOUESSE

Ingénieure de l'Ecole Polytechnique, Paris
M. Sc. in Physics, ETH Zurich

Date of Birth: 27/09/1986 Nationality: French email: celine.labouesse@m4x.org

---

PROFESSIONAL EXPERIENCE

Mar 2011 – May 2015 **PhD Student, Laboratory of Cell Biophysics, EPFL (Lausanne, CH)**
Mechanical properties of peripheral stress fibers in adherent cells spreading on patterned substrates
Supervisors: Pr. J.-J. Meister

July – Aug 2013 **Internship at University Heidelberg (GE)**
Modeling the impact of geometry on the dynamic force balance in peripheral stress fibers
Supervisor: Prof. U. S. Schwarz

Mar 2011 – Jun 2015 **Teaching Assistant, EPFL (Lausanne, CH) *~100 hrs / year***
Biophysics (3rd year B. Sc.), Prof. J.-J Meister
Physics III, Physics IV (2nd year B. Sc.), Prof. J.-J. Meister

Sep 2010 – Jan 2011 **Master Thesis at Laboratory of Cell Biophysics, EPFL (Lausanne, CH)**
Adapting the Cellular Potts Model to Determine Actin Cytoskeleton Structure and Reorganization in Cell Spreading.
Supervisors: Pr. J.-J. Meister and Dr. B. Vianay

June 2010 **Semester Project (3 weeks) at Proton Therapy Center, PSI (Villigen, CH)**
Optimizing the nominal proton energy: to what extent can the spot size be reduced and what effect would this have on the quality of treatment ?
Supervisor : Pr. A. J. Lomax

Mar – Jun 2010 **Semester Project (120h), Institute of Biomechanics, ETHZ (Zurich, CH)**
Investigation of the Relationship between Stress Fibers Tension and their Lengths
Supervisors: Pr. J. G. Snedeker, Y. Loosli

Apr. 2009 – July 2009 **Research Internship at Laboratoire Léon Brillouin (CEA Saclay, FR)**
Study of the Folding of Luciferase by Translocation through Nanopores using Neutron Scattering Experiments
Supervisors: Dr. D. Lairez, Dr. S. Combet-Jeancenel, Christophe Tasserit

---

EDUCATIONAL BACKGROUND

Mar 2011 – May 2015	**PhD Student, EPFL (Lausanne, CH)**	
Sep 2009 – Feb 2011	**Master of Science in Physics, ETHZ (Zurich, CH)**	***magna cum Laude***
Sep 2006 – Sep 2009	**Ecole Polytechnique – ParisTech (Palaiseau, FR)**	***ranking: 115/500***
Sep 2004 – Jun 2006	**Preparatory Class, Lycée Kléber (Strasbourg, FR)**	***top 2% nation-wide***
June 2004	**Baccalaureate, Lycée International des Pontonniers (Strasbourg, FR)**	

PROFESSIONAL SKILLS

Experimental Skills:
Cell culture, immunostaining, fluorescence microscopy, traction force microscopy, micro-manipulation, photolithography; knowledge of super-resolution microscopy (dSTORM)

IT Skills:

Programming languages:	Java, C++, HTML, PHP,
Software programs:	Matlab, ImageJ, Origin, Latex

Languages:
French (native)
English (bilingual, IGCSE in English Language and Literature, TOEFL IBT : 115/120)
German (B2 Diploma, conversational skills)
Russian (Beginner)

PUBLICATIONS AND CONFERENCES' CONTRIBUTIONS

Publications:
Labouesse, C., Meister, J.-J., Verkhovsky, A. B., Gabella, C., and Vianay, B.. Cell shape dynamics reveal balance of elasticity and contractility in peripheral arcs. *Biophysical Journal*, 2015, 108(10):2437-2447

Loosli, Y*., **Labouesse, C***, Luginbuehl, R., Meister, J.-J., Snedeker, J.G, and Vianay, B.. An actin length threshold regulates adhesion maturation at the lamellipodium/lamellum interface. *Integrative Biology*, 2013. 5 (6), 865 - 876
(*) shared first authorship

Oral Presentations
6th Swiss Soft Days – October 2011 (Zurich, CH)

Poster
European Cell Mech Meeting 2015 (Barcelona, Spain)
Japan-Swiss biomechanics workshop 2014 (Shima, Japan)
Biophysical Society Annual Meeting 2014 (San Francisco, USA)
European Cell Mech Meeting 2013 (Obergurgl, Austria)
Biophysical Society Annual Meeting 2012 (San Diego, USA)
Winter School for Biophysics, 2012 (Ascona, CH)
PhD Symposium Shapes in Living Systems, 2011 (Paris, France)

AWARDS

Suzuken Memorial Foundation Travel Grant (2014): Japan-Swiss biomechanics workshop

Boehringer Ingelheim Fonds Travel Grant (2013): 5 week visiting period in the group of Prof. U. Schwarz, University of Heidelberg for a project: *Modeling the impact of geometry on the dynamic force balance in peripheral stress fibers.*